

POLITECNICO
MILANO 1863

SCUOLA DI INGEGNERIA INDUSTRIALE
E DELL'INFORMAZIONE

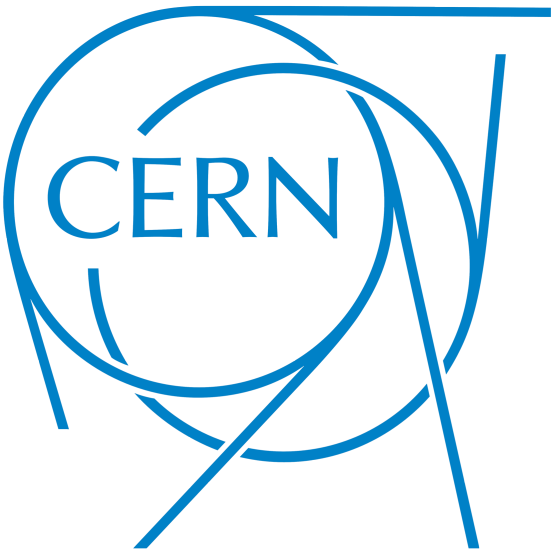
Numerical modeling of REBCO Pancake Coils with PEEC and FEM T-A based formulations

Tesi di Laurea Magistrale in
Mathematical Engineering - Ingegneria Matematica

Author: **Alessio Simoni**

Student ID: 232894
Advisor: Prof. Carlo De Falco
Co-advisors: Dr. Bernardo Bordini, Davide Rinaldoni
Academic Year: 2024-25

In collaboration with



"If you’re gonna do it, you might as well be memorable"

Abstract

High-temperature superconductor (HTS) magnets based on non-insulated (NI) rare-earth barium copper oxide (REBCO) pancake coils represent an innovative technology with potential applications in high-energy physics accelerators, nuclear fusion devices, and NMR spectroscopy.
This thesis contributes to the development of the numerical and experimental foundations of a 15 T solenoid, a sub-scale prototype of the 40 T Final Cooling Solenoid (FCS) for a Muon Collider, whose design requires engineering current densities exceeding 600 A/mm^2.

Two independent 3D computational models were developed and cross-validated. A T–A finite element model was implemented in COMSOL Multiphysics, the first of its kind for superconducting coil geometries. A thin sheet PEEC integral model was implemented in MATLAB, innovative in its current-injection strategy. In fact, an additional degree of freedom is introduced directly at the discrete level, imposing a transport current.

In parallel, an experimental program at CERN enabled several progresses toward the 15 T sub-scale HTS solenoid prototype. After their fabrication, the produced coils were successfully tested individually at 77 K, using Hall probes and voltage taps for magnetic flux density and voltage measurements.
The injection of different current profiles allowed for the identification of the equivalent circuit parameters and the critical current I_c, defined with a 1μV/cm criterion, yielding I_c = 45–60 A. As an experiment, mechanical polishing was employed on the flat faces of the coil, as a strategy to reduce the charging time of the coil to a desired value. The characteristic time reduction amounted to two orders of magnitude from around 300 s to 2 s.

Cross-validation on 9, 24, and 50-turn spirals showed maximum relative discrepancies of around 0.1-1% for current density and Joule losses, and 2–3% for the magnetic flux density, with the PEEC model requiring one to two orders of magnitude fewer degrees of freedom than the 3D FEM counterpart. Finally, the nonlinear COMSOL T–A model reproduced the measured magnetic flux density profile shape of the polished (insulated) coil, with the computed field scaling up towards the experimental data as the number of

simulated turns increased.

The future numerical and experimental work will focus on incorporating the nonlinear power-law behavior into the PEEC model, extending both models to account for radial current paths and testing single and multiple pancakes at 4.2 K to finally stack them and produce a solenoid aiming at the 15 T goal.

Keywords: HTS magnets, REBCO coils, T-A formulation, PEEC method, Muon Collider.

Abstract in lingua italiana

I magneti a superconduttore ad alta temperatura (HTS) basati su bobine pancake in REBCO (rare-earth barium copper oxide) non isolate (NI) rappresentano una tecnologia innovativa, con potenziali applicazioni in acceleratori di fisica delle alte energie, dispositivi per la fusione nucleare e spettroscopia NMR.
Questa tesi contribuisce allo sviluppo delle basi numeriche e sperimentali di un solenoide da 15 T, prototipo in scala ridotta del solenoide di cooling finale (Final Cooling Solenoid, FCS) da 40 T per un Muon Collider, il cui progetto richiede densità di corrente ingegneristiche superiori a 600 A/mm^2.

Sono stati sviluppati e confrontati due modelli computazionali 3D indipendenti. Un modello agli elementi finiti T–A è stato implementato in COMSOL Multiphysics, primo nel suo genere per bobine superconduttrici. Un modello integrale PEEC è stato invece implementato in MATLAB, innovativo per la strategia di iniezione di corrente: un grado di libertà aggiuntivo viene introdotto direttamente a livello della discretizzazione per imporre una corrente di trasporto.

In parallelo, un programma sperimentale al CERN ha permesso notevoli avanzamenti verso il prototipo di solenoide HTS da 15 T. Dopo la loro fabbricazione, le bobine prodotte sono state testate singolarmente a 77 K, utilizzando sonde di Hall e misuratori di tensione per misurare rispettivamente la densità di flusso magnetico e la distribuzione di tensione. L'iniezione di differenti profili di corrente ha consentito di identificare i parametri del circuito equivalente di una bobina e la corrente critica I_c, definita con il criterio di 1 μV/cm, ottenendo $I_c = 45$–60 A. Come primo esperimento, è stata applicata una lucidatura meccanica sulle facce piane della bobina, come strategia per ridurre il tempo di carica a un valore desiderato. La riduzione del tempo caratteristico è stata di due ordini di grandezza da circa 300 s a 2 s.

Il confronto su spirali da 9, 24 e 50 spire ha mostrato discrepanze relative massime dell'ordine di 0.1–1% per densità di corrente e perdite Joule, e del 2–3% per la densità di flusso magnetico, con il modello PEEC che richiede da uno a due ordini di grandezza in meno gradi di libertà rispetto al FEM 3D. Infine, il modello non lineare T–A in COM-

SOL ha correttamente riprodotto la forma del profilo di densità di flusso magnetico al centro, misurata per la bobina lucidata (isolata), con il campo calcolato numericamente che converge verso i dati sperimentali all'aumentare del numero di spire simulate.

Il lavoro futuro, numerico e sperimentale, si concentrerà sull'inclusione del comportamento superconduttivo non lineare nel modello PEEC, sull'estensione di entrambi i modelli per considerare i flussi radiali di corrente, e sul collaudo di singole e multiple bobine a 4.2 K, per poterle successivamente impilare e realizzare un solenoide da 15 T.

Parole chiave: magneti HTS, bobine REBCO, formulazione T-A, metodo PEEC, Muon Collider.

Contents

iii

Abstract **v**

Abstract in lingua italiana **vii**

Contents **ix**

1 Introduction **1**
1.1 Historical Context: Superconducting Magnets in Particle Accelerators . . . 1
1.2 The Muon Collider Project . . . 2
1.2.1 The 40 Tesla Final Cooling Solenoid . . . 3
1.3 Fundamentals of Superconductivity for High-Field Magnets . . . 4
1.3.1 The Superconducting State . . . 4
1.3.2 Type I and Type II Superconductors . . . 5
1.3.3 Low and High Temperature Superconductors . . . 6
1.3.4 The Quench Phenomena . . . 9
1.4 No-Insulation Pancake Coil Technology . . . 9
1.5 Research Objectives and Thesis Scope . . . 10
1.5.1 Computational Development . . . 10
1.6 Thesis Organization . . . 11

2 Theoretical Background **13**
2.1 The Magneto-Quasistatic Approximation . . . 13
2.2 A-V Formulation . . . 14
2.2.1 Differential Form and Boundary Conditions . . . 15
2.3 Gauge Invariance in Magneto-Quasistatic Problems . . . 15
2.3.1 The Coulomb Gauge Condition . . . 16
2.3.2 Analytical Solution via Green's Function . . . 16

2.4 The H-ϕ Formulation . . . 17
2.4.1 Governing Equations . . . 17
2.5 The T-A Formulation: Equations and Additional Assumptions . . . 18
2.5.1 Governing Equations . . . 18
2.5.2 Thin-Domain and Surface Flow Approximation . . . 19
2.5.3 Boundary Conditions for T-A . . . 19
2.5.4 From curvilinear to Cartesian coordinates . . . 20
2.5.5 T Integral Equation and Circuital Interpretation . . . 23
2.5.6 Advantages and Limitations of FEM T-A and PEEC . . . 24
2.6 T-A Variational Formulation . . . 25
2.7 PEEC Variational Formulation . . . 26
2.8 Nonlinear E-J Characteristic and Power Law . . . 28

3 Discretization, Quadrature and Implementation 31
3.1 Geometries and Discretization . . . 31
3.1.1 Target Geometries . . . 31
3.1.2 Basis Functions . . . 32
3.2 PEEC Discretization of the Electric Vector Potential . . . 33
3.2.1 Finite Element Setting . . . 33
3.2.2 Reference Element Basis Functions . . . 34
3.2.3 Physical Element Basis Functions . . . 35
3.3 Treatment of External Current Sources . . . 35
3.4 Algebraic formulation . . . 36
3.4.1 Extended Formulation with Imposed Current . . . 37
3.5 Weakly Singular Integral Quadrature . . . 37
3.5.1 Duffy Transformation for Singular Integrals . . . 37
3.5.2 Self inductance computation: . . . 39
3.6 Numerical Implementation of PEEC Method for Spiral HTS Coils and Rectangular Conductors . . . 40
3.6.1 Geometry Construction . . . 40
3.6.2 Matrix Assembly . . . 41
3.6.3 Right-Hand Side Assembly . . . 45
3.6.4 Enforcement of the boundary condition . . . 47
3.6.5 Problem resolution . . . 47
3.6.6 Losses and magnetic field computation . . . 47
3.6.7 Time-Domain Extension . . . 48
3.7 COMSOL Reference Model Configuration . . . 49

4 Experimental Activities and Characterization **53**
4.1 Introduction . . . 53
4.2 Coil Design and Fabrication Process . . . 53
4.2.1 Baseline Geometry . . . 54
4.2.2 Winding Apparatus . . . 55
4.3 Experimental Test Setup . . . 56
4.3.1 Cryogenic Facility . . . 57
4.4 Experiments and Measurements . . . 58
4.5 Limitations . . . 64

5 Numerical Results **65**
5.1 Introduction . . . 65
5.1.1 Test Geometries and Parameters . . . 66
5.2 Frequency-Domain Results . . . 67
5.2.1 Uniform External Magnetic Field . . . 68
5.2.2 Imposed Current Density . . . 70
5.3 Frequency vs Time-Domain Solution . . . 72
5.3.1 Comparison Overview . . . 72
5.4 Time-Domain Results . . . 75
5.4.1 9-turn spiral . . . 76
5.4.2 24-turn spiral . . . 80
5.5 Remarks on the discrepancies between the two models . . . 81
5.6 Numerical Model - Experimental Data Comparison . . . 82

6 Conclusions **85**
6.1 Future developments . . . 86

Bibliography **89**

List of Figures **97**

List of Tables **101**

1 | Introduction

The development of high-energy particle accelerators represents one of the most challenging frontiers in modern physics, driving fundamental discoveries about the nature of matter and the universe [36]. Among the critical components enabling this scientific mission, superconducting magnets play a very important role, providing the intense magnetic fields necessary to guide and focus high-energy particle beams.
As the energy frontier continues to advance, demands for both magnetic field and efficiency levels have led researchers to explore new classes of materials and innovative magnetic designs [48].

1.1. Historical Context: Superconducting Magnets in Particle Accelerators

Superconducting high-field magnets have been the necessary choice for large scale circular particle accelerators since the commissioning of the Tevatron [35] at the Fermi National Accelerator Laboratory in 1983, which demonstrated the feasibility of using superconductivity on a large scale.
Over the past four decades, from the Tevatron through HERA and finally the Large Hadron Collider (LHC) in 2008, all major hadron colliders have relied on superconducting magnets to achieve the magnetic field strengths required for high-energy physics experiments while constantly increasing the particle energies. Traditional superconducting magnets for accelerators have been constructed using low-temperature superconductors (LTS), primarily niobium-titanium (NbTi) and niobium-tin (Nb_3Sn). While NbTi magnets in the LHC operate at 1.9 K and achieve magnetic fields up to 8.3 T, the upcoming High-Luminosity LHC upgrade [13] will employ Nb_3Sn technology to reach field strengths of 11–12 T [8]. However, these conventional superconductors approach their practical performance limits around 16 T at operational temperatures near 1.9 K, necessitating the development of more advanced materials for future more advanced applications.

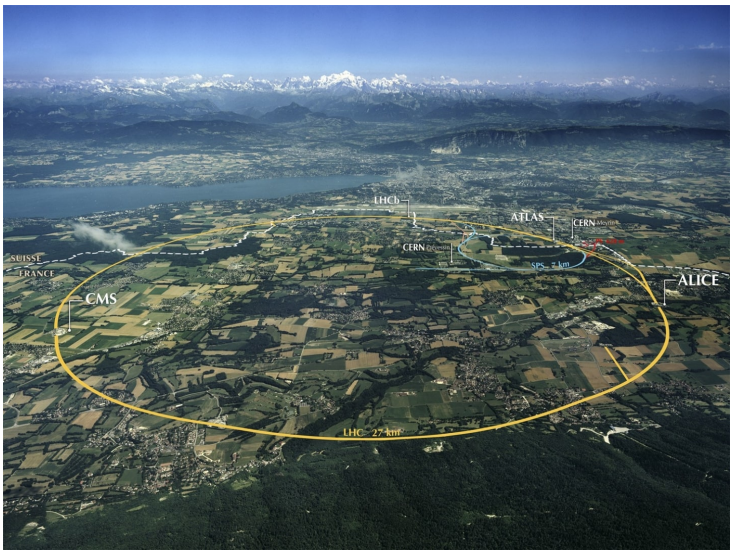


Figure 1.1: Overview of the size and particle collision points of the LHC [15].

1.2. The Muon Collider Project

The Muon Collider represents one of the most ambitious projects in high-energy physics, promising to enable precision studies of the Higgs boson and searches for physics beyond the Standard Model [14] at energies reaching 10 TeV [2]. Most particle accelerators today accelerate electrons or protons. Muons are particles similar to electrons but about 200 times more massive. This large mass difference is critical because when particles are accelerated around a circular path, they lose energy through synchrotron radiation, and this energy loss increases dramatically for lighter particles ($\propto m^{-4}$). Electrons lose energy so quickly at high speeds that building a circular electron collider at 10 TeV would be prohibitively large and expensive. Muons, being much heavier, make multi-TeV energies feasible while maintaining reasonable facility sizes [38].

Additionally, since muons are elementary particles like electrons (and unlike protons, which are composite particles made of quarks) their collisions are cleaner and more precisely interpretable. When protons collide, the actual collision occurs between their constituent quarks and gluons, each carrying only a fraction of the proton's total energy, which creates a complex background of particles and makes it harder to identify the products of interest. On the other hand, in muon collisions, the full energy of each particle is involved, producing less background noise and allowing physicists to more easily detect and study new particles or rare processes. However, muons have a major drawback: they are unstable and decay in about 2.2 μs when at rest. This means the muon beam must be rapidly cooled with a process that reduces the beam's emittance [6] (a measure of how spread out the particles are in position and momentum) to achieve the small beam

size required for high-luminosity collisions before the muons decay.

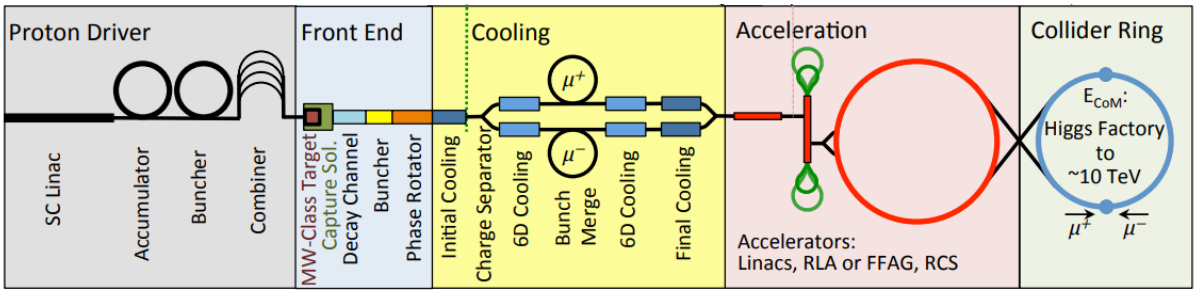


Figure 1.2: Layout of the Muon Collider as presented by the US MAP ([41]), with the 5 main stages highlighted.

1.2.1. The 40 Tesla Final Cooling Solenoid

A critical component of the Muon Collider design is the final cooling system, which must reduce the beam emittance before acceleration and injection into the collider ring.
The final cooling channel consists of multiple cells, each requiring a ultra-high-field solenoid capable of generating magnetic fields of approximately 40 T within a bore aperture of 5 cm [7]. These solenoids represent an unprecedented engineering challenge for accelerator applications, as, worldwide, only the National High Magnetic Field Laboratory (NHMFL) [34] in Tallahassee, USA, and the Chinese High Magnetic Field Laboratory (CHMFL) [33] currently operate magnets capable of producing fields exceeding 40 T. However, these existing solenoids are hybrid resistive-superconducting systems consuming 20–30 MW of power, which is completely unacceptable for accelerator applications.

The conceptual design pursued at CERN is that of a compact solenoid achieving a homogeneous magnetic field greater than 40 T over a length of approximately 0.5 m, thanks to a stack of 52 non-insulated High Temperature Superconductor (HTS) pancake coils. This innovative design employs a modular stack of spiral superconducting tape windings combined with larger correction coils placed at the edges to manage field deformation 1.3. This design requires engineering current densities exceeding 600 A/mm^2 (specifically, 632 A/mm^2 in the operational design) and must take into account the enormous electromagnetic forces while maintaining field homogeneity within 1% over the operational length. To guarantee the mechanical integrity of the 40 T solenoid, a radial pre-compression stage using an outer ring is foreseen. This pre-compression operation is technically complex as it requires very tight tolerances and high uniformity throughout the assembly. Each pancake winding is contained inside two rings that provide the structural support necessary to withstand operational stresses. The projected cost to manufacture 12 solenoids for the

complete final cooling stage is estimated at approximately 30 million euros, assuming a factor-of-two reduction in REBCO tape costs [7].

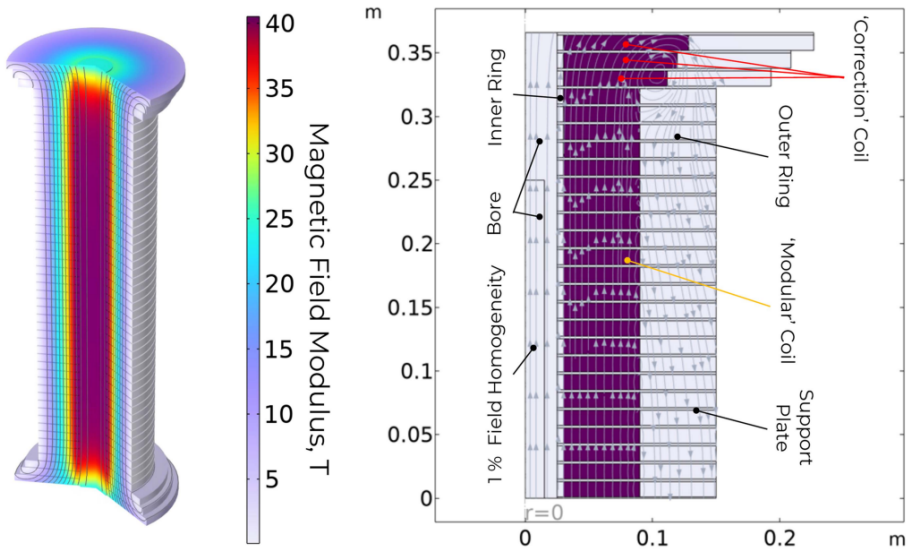


Figure 1.3: Layout and magnetic field distribution for the 40 T solenoid.
Left: magnetic field distribution. Right: a quarter cross-section enabling the view of the full structure.

This ambitious magnet design serves as primary motivation and application focus for the computational and experimental work presented in this thesis. The development of an accurate and efficient numerical models is essential for optimizing the design, predicting the performance under different operating conditions, and ensuring the feasibility of this critical component.

1.3. Fundamentals of Superconductivity for High-Field Magnets

To understand the main challenges presented by this solenoid for a Muon Collider, it is essential to introduce the basic principles of superconductivity.

1.3.1. The Superconducting State

Superconductivity is a quantum mechanical phenomenon discovered in 1911 by Heike Kamerlingh Onnes, characterized by two main properties:

- null electrical resistivity below a critical temperature T_c;

- perfect diamagnetic behavior (the Meissner effect), which expels magnetic fields from the interior of the superconductor.

These properties make superconductors uniquely suited for generating high magnetic fields with minimal energy dissipation. However, superconductivity is a fragile state that can be destroyed by exceeding any of three critical parameters:

- **Critical temperature** (T_c);
- **Critical magnetic field** (B_c;
- **Critical current density** (J_c).

These three parameters are interdependent, with the critical current density generally decreasing as temperature or magnetic field increase.

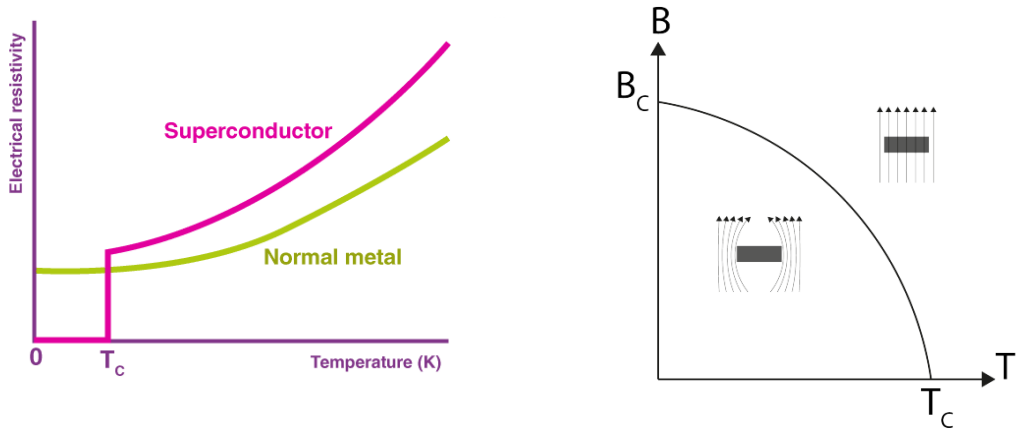


Figure 1.4: Left: plot of electrical resistivity illustrating the its temperature dependence. Right: [1] schematic of the Meissner effect showing the expulsion of magnetic field lines.

1.3.2. Type I and Type II Superconductors

Superconductors are classified into two types based on their response to magnetic fields [58]. Type I superconductors exhibit complete flux expulsion up to a single critical field B_c, at which point superconductivity abruptly disappears. These materials are generally pure metals with low critical fields (<0.2 T) and are clearly not suitable for high-field applications. Type II superconductors, which include all materials used in practical magnets, exhibit a more complex behavior. Below a lower critical field B_{C1}, they behave like Type I superconductors with complete flux expulsion. Above B_{C1} but below an upper critical field B_{C2}, magnetic flux penetrates the superconductor in quantized vortices, cre-

ating a "mixed state" or "vortex state". In this regime, the superconductor can still carry substantial currents while immersed in a high magnetic field.

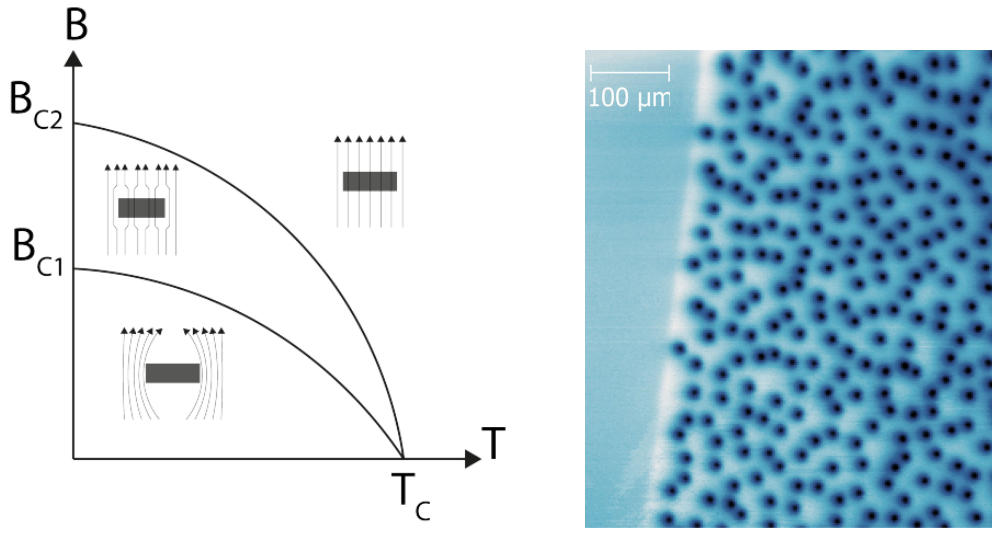


Figure 1.5: Left: [1] schematic of the Meissner effect for type II superconductors; Right: [63] plot of quantum vortices of magnetic field for $\mathbf{B}_{C1} < \mathbf{B} < \mathbf{B}_{C2}$.

The key to high current density in Type II superconductors is flux pinning [21]: defects, grain boundaries, and precipitates in the material structure "pin" the magnetic vortices, preventing their motion under the Lorentz force and thus enabling the material to carry high current densities without energy dissipation (hence without resistance). Modern materials achieve critical current densities exceeding 1000 A/mm^2 at high fields through careful engineering of these pinning centers.

1.3.3. Low and High Temperature Superconductors

Practical superconducting materials for magnets fall into two broad categories [54]. Low-Temperature Superconductors (LTS) include niobium-titanium (NbTi, $T_c \approx 10$ K) and niobium-tin (Nb_3Sn, $T_c \approx 18$ K). These materials have been the main ones used for accelerator magnets for decades. NbTi is ductile and relatively easy to manufacture into multifilamentary wires but is limited to fields below 9–10 T at 4.2 K. Nb_3Sn offers higher field capability (up to 16 T at 1.9 K) but is brittle and requires a challenging heat treatment after winding. Both materials require operation at liquid helium temperatures (4.2 K or lower).

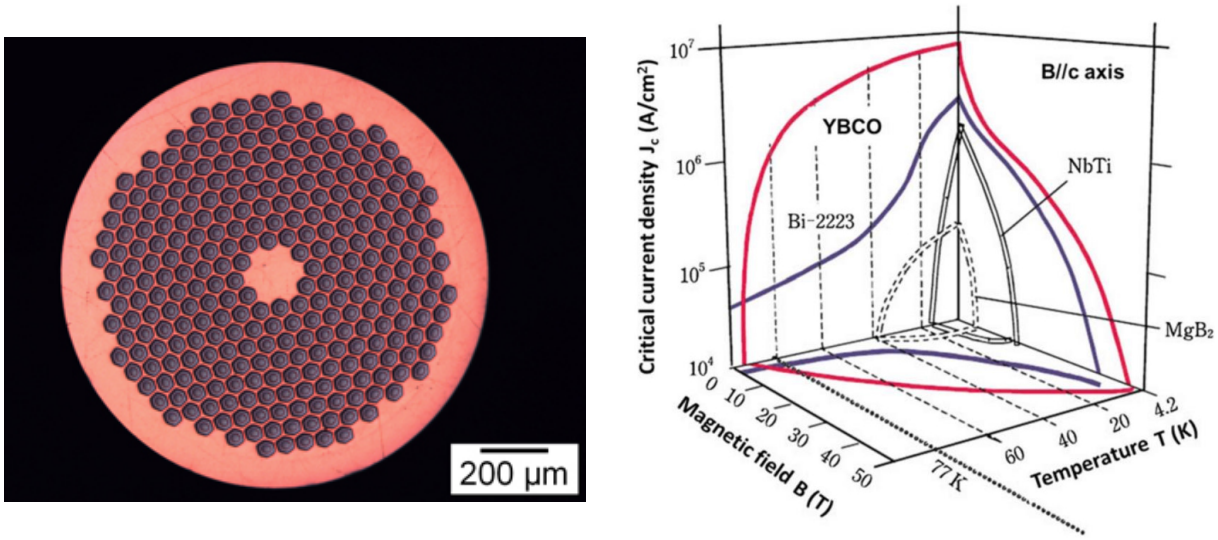


Figure 1.6: Left: [11] cross section of a Nb_3Sn wire; Right: [62] Critical current density versus magnetic field and temperature for YBCO, Bi-2223, NbTi, and MgB_2.

High-Temperature Superconductors (HTS) represent a family of materials discovered at the beginning of 1986, with critical temperatures being significantly higher. The term "high-temperature" is relative as these materials still require cryogenic cooling, but could be operated above the liquid nitrogen temperature of 77 K. For high-field magnet applications, the most important HTS material is rare-earth barium copper oxide (REBCO), typically manufactured as thin films (1–5 μm) deposited on flexible metal substrates.

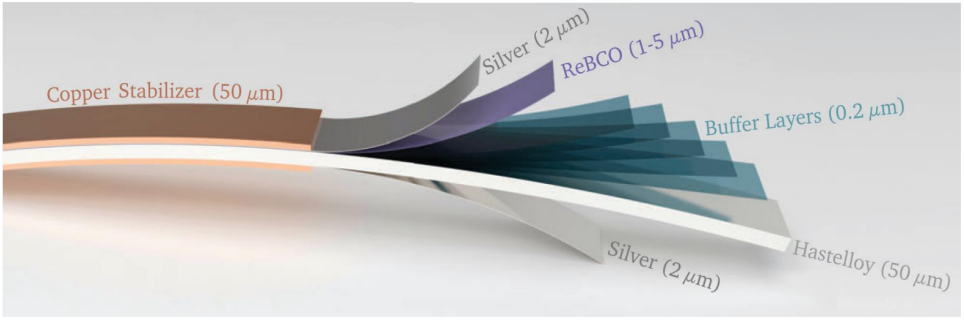


Figure 1.7: Layers composing a REBCO tape [59].

The advantages of HTS materials for ultra-high-field applications are substantial:

- **Higher critical fields**: REBCO remains superconducting in magnetic fields exceeding 40 T at 4.2 K, compared to the 16 T limit of Nb_3Sn;

- **Higher operating temperatures**: HTS can operate at 20–40 K with reduced but still great performance, simplifying cryogenics;
- **Higher engineering current density**: The thin-film architecture enables very high critical current densities in the superconducting layer;

Recent advances in REBCO conductor development have demonstrated critical current densities well exceeding 10 kA/mm^2 at 4.2 K [49], with relevant performance maintained even at fields above 30 T. These properties make REBCO the perfect technology for the 40 T Muon Collider cooling solenoid and dipoles producing a field way beyond 16 T, enabling higher collision energies as in the proposed Large Hadron Collider upgrades [52]. Beyond accelerator technologies, there is a multitude of applications for which HTS, and in particular REBCO tapes, could lead to significant changes.
In fusion energy, REBCO tapes are used to produce the high-field magnets (> 20 T) required for magnetic confinement in reactors like ITER[20] and SPARC[32], which is the second of the three steps of Commonwealth Fusion Systems (CFS) towards the commercialization of nuclear fusion technologies (see fig. 1.8).

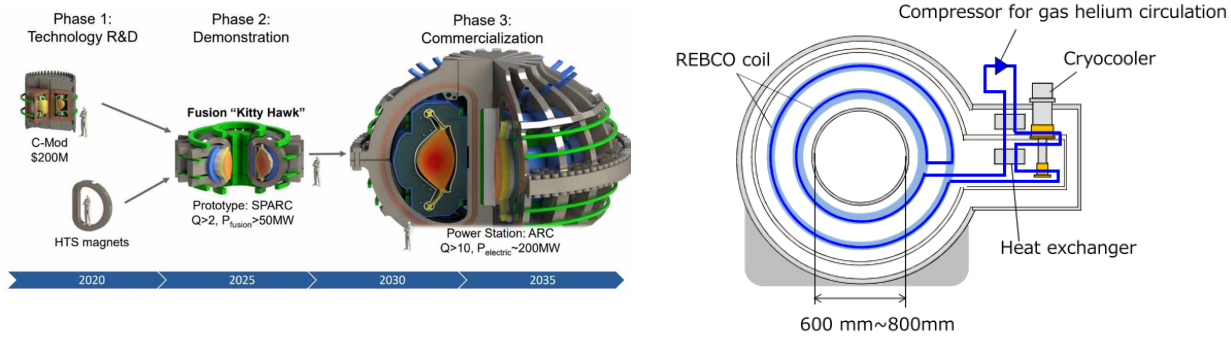


Figure 1.8: Left: R&D outline for the development of fusion devices [50] at CFS; Right: Cryogenic system of UHF-MRI HTS magnet for brain imaging and whole-body imaging [60].

In power systems, REBCO cables and transformers would dramatically reduce electrical losses and carbon footprint, additionally addressing the space limitations in urban grids [45]. Medical imaging could rely on the capability of REBCO magnets to generate fields above 10 T to improve the image resolution for neurological and oncological diagnostics [43], and REBCO's high power density could also be used for electric propulsion in aviation and maritime transport, where one of the major constraint is the weight minimization[41].

1.3.4. The Quench Phenomena

A quench is the rapid and potentially very problematic loss of superconductivity in a conductor [10].
When the superconducting state is lost, the conductor switches to the normal resistive state, generating Joule heating. This localized heating initiates a complex cascade: the normal-conducting zone propagates throughout the coil, characterized by the Normal Zone Propagation Velocity (NZPV) [39]. If the initial thermal source exceeds the quench initiation threshold, positive feedback occurs, and the normal zone expands further, generating more heat, which accelerates the propagation.
In high-field magnets, particularly those employing HTS and LTS conductors in series, quench events might generate significant operational risks: if the energy is quickly dissipated in a small volume, a large voltage is generated, which might cause damage to the insulation or induce currents, hence Lorentz forces and stresses.
In addition, if the quench is not detected and controlled quickly, the cascade continues, and the stored magnetic energy is dissipated as heat, potentially causing local melting or structural failure. The current-sharing temperature represents a critical threshold at which the superconducting layer becomes unable to carry the entire current. Beyond this point, the current begins to be redistributed to the adjacent stabilizer material (typically copper), which dissipates the energy as Joule heating.
Consequently, quench protection systems are mandatory in superconducting magnets, using quench detection circuits (to measure the voltage across the magnet), heater elements to distribute energy uniformly and reduce local hot spots, and dump resistors to safely extract the energy by de-energizing the magnet in a controlled way [55].

1.4. No-Insulation Pancake Coil Technology

No-insulation (NI) winding technology has completely changed the construction of HTS magnets by eliminating turn-to-turn insulation. In conventional coils, each turn of superconducting tape was electrically isolated from its neighbors by a thin insulation layer. In NI coils, adjacent turns are in direct electrical contact, allowing the current to flow between them. This current path has a specific inter-layer contact resistance that depends on the tape specifications and the manufacturing process. This approach provides several advantages. First of all, during a quench, the current can redistribute to neighboring turns, preventing a potentially damaging local heating. Rather than the normal-conducting zone remaining concentrated in a single turn, energy dissipation spreads more homogeneously throughout the coil structure, reducing the peak temperature. Moreover, the

direct metal-to-metal contact between turns significantly increases the mechanical properties of the coil. Recent prototypes showed the incredible performance of NI technology. As an example, a 26 T magnet with a 35 mm bore, constructed from 26 REBCO double pancake coils, was successfully tested at the National High Magnetic Field Laboratory [34]. The success of NI technology has made it the preferred approach for ultra-high-field applications.
However, the associated electromagnetic behavior requires two or three-dimensional numerical models capable of capturing both the azimuthal and radial current dynamics. Understanding these current paths is essential for two main reasons: controlling the magnetic field distribution, which directly affects the accelerator performance, and managing heat generation in case of localized hotspots that may damage the superconductor.

1.5. Research Objectives and Thesis Scope

This thesis addresses two different numerical models having the final goal of reproducing the electrodynamic behavior of superconducting magnets, with particular focus on the requirements of the final cooling solenoid of the Muon Collider.
In addition, the experimental activities for the fabrication of a first prototyped step of such a solenoid will be shown, whose short term objective is to achieve a 15 T peak field before September 2026.

1.5.1. Computational Development

Currently, existing models are able to accurately describe the transient behavior of non-insulated REBCO superconducting coils, but often lack computational efficiency, especially as the number of turns increases and the coil size grows. The primary computational objective is the development and implementation of a T-A PEEC integral method in MATLAB and a T-A Finite Element Model (FEM) in COMSOL capable of modeling insulated pancake coils with realistic geometric and electromagnetic characteristics. Although popular mathematical formulations such as the H-ϕ [23] are highly accurate, they are currently too computationally expensive to simulate large-scale systems like accelerator magnets, often requiring millions of degrees of freedom and simulation times spanning hours or days. To overcome this challenge, novel approaches based on alternative mathematical formulations are needed. Specific goals include: the implementation in MATLAB of a Partial Element Equivalent Circuit (PEEC) integral version of the T-A formulation; the implementation in COMSOL Multiphysics of a finite element T-A model designed for superconducting pancake coils; a cross-checking between the two models for two test

cases of coils with 9 and 24 turns.

Complementing the computational work, this thesis includes the experimental activities aimed at building a sub scale solenoid prototype of the 40 T one. In particular, the short term goal is fabricating a solenoid capable of generating a peak field of 15 T before September 2026. In addition, the experimental data can also be used to validate the numerical models and gain insight into the HTS coil behavior.
The activity can be logically subdivided in three parts. The HTS fully soldered pancake coil fabrication, where coils are wound using commercially acquired REBCO tape. The cryogenic characterization, in which they are tested and measured to determine their electrical and magnetic properties in liquid nitrogen (77 K). The comparison between the numerical results and the experimental data, to validate and tune the computational models to reproduce the voltages and magnetic flux densities measured in the experimental campaign. The integration of computational models and experimental data can provide a broader approach that improves the understanding of HTS magnet behavior.

1.6. Thesis Organization

This thesis is organized as follows:

Chapter 2 presents the electromagnetic theoretical foundation of the T-A formulation, starting from Maxwell's equations and deriving the complete set of equations with the relative boundary conditions. The thin-sheet approximation is also introduced, along with other theoretical remarks, and finally the weak formulations are derived and illustrated to constitute a solid starting point for the discrete problem.
Chapter 3 introduces the finite dimensional setting and the discrete and algebraic formulations that were used for the PEEC model and briefly discusses the T-A FEM ones. In addition, the actual implementation of the MATLAB and COMSOL models is illustrated.
Chapter 4 describes the fabrication and cryogenic testing of HTS pancake coils, introducing and showing the setups that were developed and used, presenting the experimental results and some of the conclusions that can be drawn from them.
Chapter 5 presents the validation of the numerical models using pre-existing Octave or COMSOL models for a numerical comparison of squared and coil geometries.
Chapter 6 summarizes the main achievements of the thesis and suggests directions for further developments.

2 | Theoretical Background

This chapter develops a comprehensive overview of the theoretical background needed for the electromagnetic modeling of superconducting systems using the PEEC method, inspired by [53] and illustrated in [56], and the T-A formulation [66]. The analysis begins with Maxwell's equations in differential form, progresses through the A-V and H-ϕ formulations [23], in order to understand their limitations, and then approaches the T-A formulation in the differential and PEEC integral form. Finally, their associated variational formulations are presented before concluding with the PEEC circuit interpretation.

2.1. The Magneto-Quasistatic Approximation

The electromagnetic behavior of superconducting devices is governed by Maxwell's equations, which provide a complete description of electromagnetic fields in both time and space. For superconducting magnets operating under slowly varying conditions, significant simplifications are achieved through the magneto-quasistatic (MQS) approximation.

Let $\Omega \subset \mathbb{R}^3$ be a three-dimensional domain, then consider $\Omega_c \subset \Omega$ as its subset constituted by electrically conducting regions in which a non-zero current density $\mathbf{J}$ can flow, and a resistivity ρ and conductivity σ are defined. In its complementary set $\Omega_c^C \subset \Omega$ the insulating regions are grouped together and the current density is zero.
Both the time and frequency domain formulations will be presented, starting with the former. For this reason, it is also useful to define a time interval $\mathrm{I} = [\mathrm{t}_0, \mathrm{t}_f]$.
In a continuous medium, Maxwell's equations in differential form are defined in the space time domain $\Omega \times \mathrm{I}$, as divergence and curl of electric and magnetic field.

$$\begin{cases} \nabla \times \mathbf{H} = \mathbf{J} + \epsilon_0 \dfrac{\partial \mathbf{E}}{\partial t}, & \text{(Ampère's law)} \\ \nabla \times \mathbf{E} = -\dfrac{\partial \mathbf{B}}{\partial t}, & \text{(Faraday's law)} \\ \nabla \cdot \mathbf{E} = \dfrac{\rho}{\epsilon_0}, & \text{(Gauss's law)} \\ \nabla \cdot \mathbf{B} = 0, & \text{(Magnetic flux conservation)} \end{cases} \tag{2.1}$$

where $\mathbf{H}\,[\mathrm{A\,m^{-1}}]$, $\mathbf{J}\,[\mathrm{A\,m^{-2}}]$, $\mathbf{E}\,[\mathrm{V\,m^{-1}}]$, $\mathbf{B}\,[\mathrm{T}]$, $\rho\,[\mathrm{C\,m^{-3}}]$ denote the magnetic field, current density, electric field, magnetic flux density, and electric charge density, respectively, and $\epsilon_0\,[\mathrm{F\,m^{-1}}]$ is the vacuum permittivity.
Moreover, the constitutive relations can be added:

$$\mathbf{B} = \mu\mathbf{H}, \quad \mathbf{J} = \sigma(\mathbf{B}, \mathrm{T})\mathbf{E} \tag{2.2}$$

where $\mu\,[\mathrm{H\,m^{-1}}]$ and $\sigma\,[\mathrm{S\,m^{-1}}]$ denote the permeability and conductivity, respectively. The dependency of the latter from temperature or magnetic field will be of particular interest. Together, Eqs. (2.1) and (2.2), form a system of equations having the electric field, $\mathbf{E}$, and magnetic flux density, $\mathbf{B}$, as unknowns.

The MQS approximation applies when the displacement current $\epsilon_0 \dfrac{\partial \mathbf{E}}{\partial t}$ is negligible compared to the conduction current density $\mathbf{J}$. This is valid when the ratio between the electromagnetic time scale $\tau_{\mathrm{em}} = r/c$, where r represents a characteristic length scale of the system and c the speed of light in vacuum, and the characteristic time scale of the problem $\tau = 1/\omega$, with ω representative angular frequency of the problem $\dfrac{\tau_{\mathrm{em}}}{\tau} \ll 1$.
For superconducting magnets with dimensions on the order of meters and operating frequencies below 1 kHz, this condition is satisfied. The physical interpretation is that the rate of change of the electric field is sufficiently slow that capacitive effects can be neglected [9], allowing the analysis to focus exclusively on conduction currents. Under the MQS approximation Eq. (2.1) can be rewritten as:

$$\begin{cases} \nabla \times \mathbf{H} = \mathbf{J} \\ \nabla \times \mathbf{E} = -\dfrac{\partial \mathbf{B}}{\partial t} \\ \nabla \cdot \mathbf{E} = \dfrac{\rho}{\epsilon_0} \\ \nabla \cdot \mathbf{B} = 0 \end{cases} . \tag{2.3}$$

In addition, if the divergence operator is applied to the first equation, the current conservation equation is obtained:

$$\nabla \cdot \mathbf{J} = \nabla \cdot (\nabla \times \mathbf{H}) = 0. \tag{2.4}$$

2.2. A-V Formulation

Before introducing the T-A formulation used in this thesis, it is instructive to briefly review a couple of classical formulations, the A-V [47] and H-ϕ [23] formulations. Un-

derstanding their advantages and limitations is important to motivate the development of novel approaches. The A-V formulation is usually the default choice for magnetic field calculations in commercial finite element codes [46]. It involves the magnetic vector potential $\mathbf{A}$, to automatically satisfy the solenoidal constraint on the magnetic flux density, and the electric scalar potential V.

2.2.1. Differential Form and Boundary Conditions

As first step, define the magnetic vector potential such that $\mathbf{B} = \nabla \times \mathbf{A}$. In this way the magnetic flux conservation equation $\nabla \cdot \mathbf{B} = 0$ is identically satisfied at any time t$\in$ I. Ampère and Faraday laws can then be rewritten to obtain the two-equation system:

$$\begin{cases} \nabla \times \left(\frac{1}{\mu} \nabla \times \mathbf{A} \right) = \mathbf{J}, \text{ in } \Omega, \\ \mathbf{E} = -\frac{\partial \mathbf{A}}{\partial t} - \nabla V, \text{ in } \Omega. \end{cases} \tag{2.5}$$

where V is the scalar electric potential field.

Typical boundary and interface conditions for the A-V formulation include:

- Magnetic insulation: $\mathbf{n} \times \mathbf{A} = \mathbf{0}$ on $\partial\Omega$;
- Dirichlet on V: $V = V_0$ on conductor surfaces $S_V \subset \partial\Omega_c$ where the electric scalar potential is fixed;
- Homogeneous Neumann on V: $\mathbf{n} \cdot \sigma \nabla V = 0$ on insulating boundaries $S_I \subset \partial\Omega_c$;
- Continuity at interfaces: $\mathbf{n} \times \mathbf{A}$ continuous across material boundaries.

2.3. Gauge Invariance in Magneto-Quasistatic Problems

An important observation in electromagnetic theory is that $\mathbf{A}$ is not uniquely defined [25]; this feature is known as gauge freedom or gauge invariance.
Consider the vector potential $\mathbf{A}'$ defined as

$$\mathbf{A}' = \mathbf{A} + \nabla\chi,$$

where $\chi : \Omega \to \mathbb{R}$ is an arbitrary differentiable scalar function (called gauge function): it produces the identical magnetic flux density as the original potential $\mathbf{A}$.

This fundamental property arises from the vector identity $\nabla \times (\nabla \chi) = \mathbf{0}$, which ensures that

$$\mathbf{B} = \nabla \times \mathbf{A}' = \nabla \times \mathbf{A} + \nabla \times (\nabla \chi) = \nabla \times \mathbf{A}.$$

Consequently, the magnetic flux density is uniquely determined regardless of which gauge is chosen, while the vector potential itself remains underdetermined. This freedom, though being sometimes advantageous, necessitates the introduction of an additional constraint to make the vector potential unique.

2.3.1. The Coulomb Gauge Condition

Among the numerous gauge choices available in electromagnetic theory, the Coulomb gauge is widely employed in magneto-quasistatic formulations. This gauge is defined by the simple divergence-free condition:

$$\nabla \cdot \mathbf{A} = 0.$$

When the Coulomb gauge condition is imposed, the vector potential satisfies a simplification of the governing equations. In fact, under this constraint, the first equation of (2.5) turns into the Poisson's equation:

$$\nabla^2 \mathbf{A} = -\mu_0 \mathbf{J}. \tag{2.6}$$

This equation represents a direct relationship between the spatial distribution of currents and the resulting vector potential field. Each component of $\mathbf{A}$ independently satisfies Poisson's equation, provided that the current distribution satisfies the charge continuity equation $\nabla \cdot \mathbf{J} = 0$, which constitutes a necessary compatibility condition for the consistency of equation (2.6).

2.3.2. Analytical Solution via Green's Function

The solution to Poisson's equation in unbounded three-dimensional space can be expressed analytically using the Green's function method, a useful technique in potential theory. The fundamental Green's function for three-dimensional Poisson's equation is given by:

$$G(\mathbf{r}, \mathbf{r}') = \frac{1}{4\pi |\mathbf{r} - \mathbf{r}'|},$$

where $\mathbf{r}$ denotes the field point (observation point) and $\mathbf{r}'$ denotes the source point.
This Green's function represents the solution to $\nabla^2 G = -\delta(\mathbf{r} - \mathbf{r}')$, where δ is the Dirac

delta distribution and describes the potential at field point $\mathbf{r}$ due to a point source located at $\mathbf{r}'$, with magnitude inversely proportional to the Euclidean distance between them.

By employing the Green's function, the solution to the Poisson's equation in the domain can be expressed as a convolution integral:

$$\mathbf{A}(\mathbf{r}) = \mu_0 \int_{\Omega_c} G(\mathbf{r}, \mathbf{r}')\mathbf{J}(\mathbf{r}')\, d\Omega' + \mathbf{A}_0(\mathbf{r}), \tag{2.7}$$

where the integration extends over the domain $\Omega_c \subset \mathbb{R}^3$ containing current-carrying conductors and $\mathbf{A}_0$ represents the magnetic contribution from external sources. This representation ensures that the resulting vector potential is consistent with both the differential equation and the Coulomb gauge constraint. Moreover, (eq. (2.7)) will be very useful in obtaining the integral equation of the PEEC formulation.

2.4. The H-ϕ Formulation

The H-ϕ formulation is a second standard formulation, more suitable to approach the simulation of superconducting magnets. It performs well at handling the nonlinearity of the superconducting constitutive law, is more versatile, and computationally competitive for 3D geometries like bulks, but it has a clear disadvantage when dealing with thin geometries. This can be partially recovered by means of homogenization techniques, as shown in [24] or [31].

2.4.1. Governing Equations

The H-ϕ formulation employs a mixed formulation with two unknowns: the magnetic field $\mathbf{H}$ in the conducting regions Ω_c, and the magnetic scalar potential ϕ in the non-conducting regions Ω_c^C.
The governing equations are:

$$\begin{cases} \nabla \times (\rho \nabla \times \mathbf{H}) = -\mu \dfrac{\partial \mathbf{H}}{\partial t}, & \text{in } \Omega_c, \\ \nabla \cdot (\mu \nabla \phi) = 0, & \text{in } \Omega_c^C. \end{cases} \tag{2.8}$$

To close the problem, appropriate boundary conditions must be imposed at the interface $\Gamma = \partial\Omega_c \cap \partial\Omega_c^C$ between conducting and non-conducting regions, and at the external boundary $\partial\Omega$ [23].

2.5. The T-A Formulation: Equations and Additional Assumptions

The A-V and $\mathbf{H} - \phi$ formulations have two main common computational disadvantages. First of all, as all Finite Element approaches, they require the discretization of the entire domain Ω, including the air regions with no current sources, leading to larger matrices. Second, in order to reduce the effect of the artificial magnetic insulation boundary condition, the domain's size needs to be sufficiently large, increasing the computational complexity. In addition, with the A-V formulation is difficult to cope with the nonlinear electric law of superconductors (power law) using the A-V formulation.
The T-A formulation [37] introduces the current vector potential $\mathbf{T}$ to represent the current density such that $\mathbf{J} = \nabla \times \mathbf{T}$. This automatically ensures that the current density field is divergence free.

2.5.1. Governing Equations

The T-A formulation, obtained by rewriting (eq. (2.5)) with the introduction of the new electric vector potential:

$$\begin{cases} \nabla \times \mathbf{E} = -\dfrac{\partial(\nabla \times \mathbf{A})}{\partial t}, \text{ in } \Omega_c & \text{(Faraday law)} \\ \nabla \times (\nabla \times \mathbf{A}) = \mu_0 \mathbf{J} = \mu_0 (\nabla \times \mathbf{T}), \text{ in } \Omega & \text{(Ampère law)} \end{cases} \tag{2.9}$$

where the electric field can also be related to the current density through the constitutive law: $\mathbf{E} = \dfrac{\mathbf{J}}{\sigma(\mathbf{J}, \mathbf{B})}$.

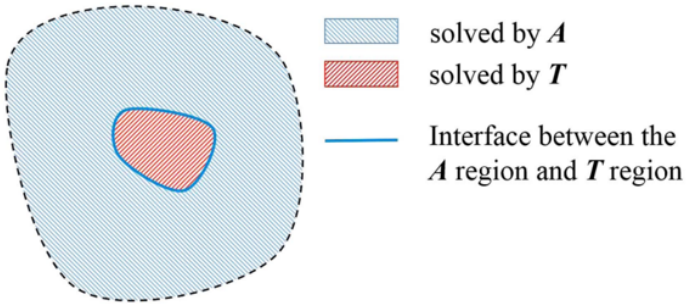


Figure 2.1: Visualisation of the different computational domains of the two equations [66]

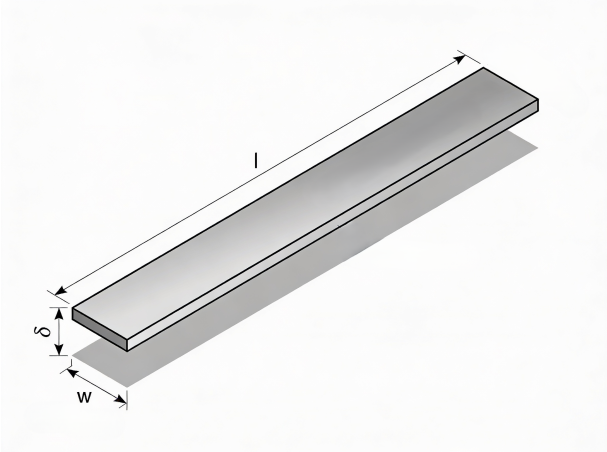


Figure 2.2: Example of domain satisfying the mentioned condition

2.5.2. Thin-Domain and Surface Flow Approximation

For tapes with thickness δ much smaller than width w and length l, see (fig. 2.2), the thin-domain approximation assumes that the distribution of all the involved variables is uniform across the thickness of the tape. For a pancake coil, this approach basically represents a homogenization through the thin layer δ, assuming quantities do not vary along the the radial direction. Moreover, in a local orthonormal cylindrical frame $\{\hat{r}, \hat{\theta}, \hat{z}\}$ (radial, azimuthal, axial), if the current is not allowed to flow along $\hat{\mathbf{r}}$ (meaning no radial current when tape is wound into a coil) the current vector potential can be reduced to:

$$\mathbf{T} = T\hat{\mathbf{r}}, \quad \mathbf{J} = \nabla \times \mathbf{T} = \frac{\partial T}{\partial z}\hat{\theta} - \frac{\partial T}{\partial \theta}\hat{\mathbf{z}} \tag{2.10}$$

where T is a scalar function, and the current is only allowed to flow parallel to the surface of the tape.

2.5.3. Boundary Conditions for T-A

The boundary conditions for the magnetic vector potential $\mathbf{A}$ are the same described in paragraph 2.2.2 for the A-V formulation.
A new condition on the electric vector potential has to be obtained. The integral of current density over a cross-section Σ can be expressed as:

$$I_0 = \int_{\Sigma} \mathbf{J} \cdot d\mathbf{S} = \oint_{\partial\Sigma} \mathbf{T} \cdot d\mathbf{s} = (T_2 - T_1)\delta \tag{2.11}$$

where T_1, T_2 are, under the thin domain approximation the top and bottom edge values of the electric vector potential (see fig. 2.3) and δ is the thickness of the geometry. The

immediate consequence is that by simply fixing a value for one of them, for instance T_1, and analytically obtaining the corresponding one of T_2, the total current I_0 is imposed. For simplicity, we take $T_1 = 0$, hence $T_2 = \frac{I_0}{\delta}$.

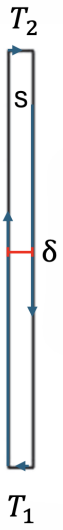


Figure 2.3: Generic cross section of the tape Σ on which T2 and T1 are fixed.

2.5.4. From curvilinear to Cartesian coordinates

In the presented formulation, the only unknown is a scalar field having radial direction. However, COMSOL Multiphysics requires the equations to be expressed in Cartesian coordinates. Hence, it was necessary to rewrite the Faraday equation from the curvilinear coordinates into the Cartesian reference system so that it could be implemented.
Given a normal vector $\mathbf{n} = (n_x, n_y, n_z)$ on the HTS surface, the current density components can be expressed as:

$$\begin{aligned} J_x &= \frac{\partial(Tn_z)}{\partial y} - \frac{\partial(Tn_y)}{\partial z} \\ J_y &= \frac{\partial(Tn_x)}{\partial z} - \frac{\partial(Tn_z)}{\partial x} \\ J_z &= \frac{\partial(Tn_y)}{\partial x} - \frac{\partial(Tn_x)}{\partial y} \end{aligned} \tag{2.12}$$

And Faraday's law becomes:

$$\begin{bmatrix} \frac{\partial E_z}{\partial y} - \frac{\partial E_y}{\partial z} \\ \frac{\partial E_x}{\partial z} - \frac{\partial E_z}{\partial x} \\ \frac{\partial E_y}{\partial x} - \frac{\partial E_x}{\partial y} \end{bmatrix} \cdot \mathbf{n} + \begin{bmatrix} \frac{\partial B_x}{\partial t} \\ \frac{\partial B_y}{\partial t} \\ \frac{\partial B_z}{\partial t} \end{bmatrix} \cdot \mathbf{n} = 0 \tag{2.13}$$

We assume that the unknown electric vector potential has only one non-zero component, namely the one orthogonal to the surface of the spiral, i.e., the radial component.
The curvilinear $\{\hat{r}, \hat{\theta}, \hat{z}\}$ and Cartesian $\{\hat{x}, \hat{y}, \hat{z}\}$ coordinate systems can be related through a transformation:

$$\begin{bmatrix} \hat{r} \\ \hat{\theta} \\ \hat{z} \end{bmatrix} = \begin{bmatrix} T_{11}(x,y) & T_{12}(x,y) & 0 \\ T_{21}(x,y) & T_{22}(x,y) & 0 \\ 0 & 0 & 1 \end{bmatrix} \begin{bmatrix} \hat{x} \\ \hat{y} \\ \hat{z} \end{bmatrix}$$

or, inversely,

$$\begin{bmatrix} \hat{x} \\ \hat{y} \\ \hat{z} \end{bmatrix} = \begin{bmatrix} T'_{11}(r,\theta) & T'_{12}(r,\theta) & 0 \\ T'_{21}(r,\theta) & T'_{22}(r,\theta) & 0 \\ 0 & 0 & 1 \end{bmatrix} \begin{bmatrix} \hat{r} \\ \hat{\theta} \\ \hat{z} \end{bmatrix}.$$

Assume now that eq. (2.13) is expressed in this curvilinear reference system:

$$\begin{bmatrix} (\frac{\partial E_z}{\partial \theta} - \frac{\partial E_\theta}{\partial z}) \\ \frac{\partial E_r}{\partial z} - \frac{\partial E_z}{\partial r} \\ (\frac{\partial E_\theta}{\partial r} - \frac{\partial E_r}{\partial \theta}) \end{bmatrix} \cdot \mathbf{n} + \begin{bmatrix} \frac{\partial B_r}{\partial t} \\ \frac{\partial B_\theta}{\partial t} \\ \frac{\partial B_z}{\partial t} \end{bmatrix} \cdot \mathbf{n} = 0 \tag{2.14}$$

Given the geometry, we can reasonably assume that the electric field components are constant along the thickness of the tape, i.e., along the radial direction. This assumption follows from taking T as constant in $\hat{\mathbf{r}}$, which implies (from $\mathbf{J} = \nabla \times \mathbf{T}$):

$$J_r = 0, \quad J_\theta = \frac{\partial T}{\partial z}, \quad J_z = -\frac{\partial T}{\partial \theta}.$$

If J_θ and J_z are constant through the thickness δ, then, due to the constitutive relation $\mathbf{E} = \rho\,\mathbf{J}$, the electric field $\mathbf{E}$ also exhibits the same behavior. Therefore, only the first component of eq. (2.14) remains relevant:

$$\frac{\partial E_z}{\partial \theta} - \frac{\partial E_\theta}{\partial z} + \frac{\partial B_r}{\partial t} = 0 \tag{2.15}$$

Substituting the electric field with the current density through the resistivity ρ, we obtain:

$$\frac{1}{\rho}\left(\frac{\partial J_z}{\partial \theta} - \frac{\partial J_\theta}{\partial z}\right) + \left(\frac{\partial B_r}{\partial t}\right) = 0 \tag{2.16}$$

We now need to express this equation in the Cartesian coordinate system using the transformation relations.
First, we expand the derivative:

$$\frac{\partial J_z}{\partial \theta} = \frac{\partial J_z}{\partial x}\frac{\partial x}{\partial \theta} + \frac{\partial J_z}{\partial y}\frac{\partial y}{\partial \theta} + \frac{\partial J_z}{\partial z}\frac{\partial z}{\partial \theta} = \frac{\partial J_z}{\partial x}\,T'_{12} + \frac{\partial J_z}{\partial y}\,T'_{22}$$

The magnetic field component B_r is expressed as:

$$B_r = B_x\,T_{11} + B_y\,T_{12} + B_z\,T_{13} = B_x\,T_{11} + B_y\,T_{12}$$

Moreover, we rewrite J_z in terms of T:

$$J_z = -\frac{\partial T}{\partial \theta} = -\left(\frac{\partial T}{\partial x}\frac{\partial x}{\partial \theta} + \frac{\partial T}{\partial y}\frac{\partial y}{\partial \theta} + \frac{\partial T}{\partial z}\frac{\partial z}{\partial \theta}\right) = -\left(\frac{\partial T}{\partial x}\,T'_{12} + \frac{\partial T}{\partial y}\,T'_{22}\right)$$

We thus arrive at the final expression of the equation that was implemented in COMSOL:

$$\boxed{\frac{1}{\rho}\left(\frac{\partial J_z}{\partial x}\,T'_{12} + \frac{\partial J_z}{\partial y}\,T'_{22} - \frac{\partial J_\theta}{\partial z}\right) = -\frac{\partial}{\partial t}\left(T_{11}\,B_x + T_{12}\,B_y\right)} \tag{2.17}$$

2.5.5. T Integral Equation and Circuital Interpretation

The way to have a formulation that overcomes some of the limitations is to combine the T-A formulation equations to obtain a single integral equation, leading to a different numerical setting than the traditional Finite Element approaches.
Starting from Faraday's law in Ω_c:

$$\nabla \times \mathbf{E} = -\frac{\partial(\nabla \times \mathbf{A})}{\partial t}. \tag{2.18}$$

Rewriting now as $\nabla \times (\mathbf{E} + \partial \mathbf{A}/\partial t) = \mathbf{0}$, which implies, as already shown before:

$$\mathbf{E} + \frac{\partial \mathbf{A}}{\partial t} = -\nabla V, \tag{2.19}$$

If the expressions $\mathbf{E} = (\nabla \times \mathbf{T})/\sigma$ and the integral form of $\mathbf{A}$ (2.7) are substituted into eq. (2.19), the final expression almost appears:

$$\frac{\nabla \times \mathbf{T}}{\sigma} + \frac{\partial}{\partial t}\left[\frac{\mu_0}{4\pi}\int_{\Omega_c} \frac{\nabla \times \mathbf{T}(\mathbf{r}')}{|\mathbf{r}-\mathbf{r}'|}\, d\Omega' + \mathbf{A}_0(\mathbf{r})\right] = -\nabla V, \tag{2.20}$$

as it only needs to be rearranged by moving all the forcing terms to the right hand side:

$$\boxed{\frac{\nabla \times \mathbf{T}}{\sigma} + \frac{\mu_0}{4\pi}\frac{\partial}{\partial t}\int_{\Omega_c} \frac{\nabla \times \mathbf{T}(\mathbf{r}')}{|\mathbf{r}-\mathbf{r}'|}\, d\Omega' = -\frac{\partial \mathbf{A}_0}{\partial t} - \nabla V} \tag{2.21}$$

Equation (2.21) has a clear physical interpretation. The first term represents the resistive contribution to the voltage gradient due to current flow, while the second term represents the contribution due to self and mutual inductive effects. Finally, the right-hand side represents external driving terms from applied magnetic fields and electric potential gradients.
This structure directly resembles Kirchhoff's voltage law in circuit analysis, making such integral formulation particularly suitable for a reinterpretation with a partial equivalent circuit [53] representation.
Consider, as an example, a double non-insulated REBCO pancake coil. If such conductor is divided both azimuthally and radially into partial elements, its equivalent circuit can be constructed as in fig. 2.4. In this thesis, the capacitive effects are neglected, and the only electrical elements needed are resistances and inductances.
In this particular case, the resistive and superconducting effects of the tape itself are represented by two resistances in parallel, and only the resistive effect is taken into account for the radial current flow.

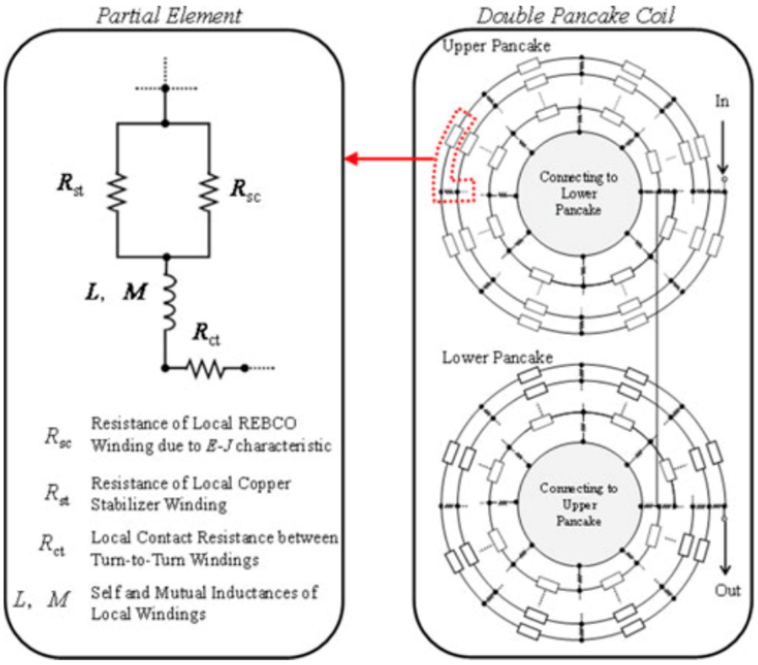


Figure 2.4: Partial element equivalent circuit of a double pancake [42].

2.5.6. Advantages and Limitations of FEM T-A and PEEC

Both the FEM T-A formulation and the PEEC method offer a computational advantage over fully 3D formulations through a dimensionally mixed approach. FEM T-A utilizes a 1D electric and 3D magnetic approach to reduce the number of degrees of freedom, while PEEC solves only a 1D electrical equation and discretizes just the conducting regions, significantly reducing the problem size. Additionally, this separation of electric and magnetic computations allows for a more robust and easier implementation of the non-linear E-J power law.

However, PEEC has specific limitations: it generates a dense inductance matrix L that represents the mutual inductive effects across the entire domain, requiring $\mathcal{O}(N^2)$ memory and assembly time, with N total number of degrees of freedom (see section 3.6), and its self-inductance terms involve weakly singular integrals of the type $|x-y|^{-\alpha}$ (where $0 < \alpha < 1$), which necessitate suitable quadrature rules.

2.6. T-A Variational Formulation

The T-A formulation is based on the simultaneous evolution of two electromagnetic fields: the magnetic vector potential $\mathbf{A}$ and the electric vector potential $\mathbf{T}$. To enable the finite element discretization while ensuring mathematical well-posedness, the system of equations is reformulated in the variational framework. As presented in detail in [22], by multiplying the differential form of the T-A equations by test functions $\mathbf{a}' \in \mathbf{V}$ and $\mathbf{t}' \in \mathbf{Q}$, integrating over the domain, and applying integration by parts on the curl-curl term yields the weak formulation:

$$\boxed{\begin{cases} a(\mathbf{A}, \mathbf{a}') - b(\mathbf{a}', \mathbf{T}) = f(\mathbf{a}') \quad \forall \mathbf{a}' \in \mathbf{V}, \\ -\dfrac{\partial b(\mathbf{A}, \mathbf{t}')}{\partial t} + c(\mathbf{T}, \mathbf{t}') = g(\mathbf{t}') \quad \forall \mathbf{t}' \in \mathbf{Q}. \end{cases}} \tag{2.22}$$

The bilinear forms are defined as:

$$a(\cdot,\cdot) : \mathbf{V} \times \mathbf{V} \to \mathbb{R};\ a(\mathbf{A}, \mathbf{a}') = \int_\Omega \frac{1}{\mu} (\nabla \times \mathbf{A}) \cdot (\nabla \times \mathbf{a}')\, d\Omega, \tag{2.23}$$

$$b(\cdot,\cdot) : \mathbf{V} \times \mathbf{Q} \to \mathbb{R};\ b(\mathbf{T}, \mathbf{t}) = \int_{\Omega_c} (\nabla \times \mathbf{T}) \cdot \mathbf{t}\, d\Omega_c, \tag{2.24}$$

$$c(\cdot,\cdot) : \mathbf{Q} \times \mathbf{Q} \to \mathbb{R};\ c(\mathbf{T}, \mathbf{t}') = \int_{\Omega_c} \rho(\mathbf{T})\, (\nabla \times \mathbf{T})\, (\nabla \times \mathbf{t}')\, d\Omega_c. \tag{2.25}$$

The functional $\mathrm{f}(\mathbf{a}') = 0$, while $\mathrm{g}(\mathbf{t}')$, even though momentarily null, is useful for representing, in the discrete framework, the term arising from a time stepping scheme as Backward Euler related to the bilinear form $b(\cdot,\cdot)$.

The variational formulation requires two distinct spaces, each with specific properties reflecting the physics of the problem. In order to properly define the functional spaces required for the problem of our interes, it is necessary to first introduce the space of square-integrable functions over the domain Ω, denoted as $L^2(\Omega)$.
A scalar function u belongs to $L^2(\Omega)$ if its L^2-norm is finite, defined as:

$$\|\mathbf{v}\|_{L^2} = \left(\int_\Omega |u|^2 d\Omega \right)^{1/2} < \infty. \tag{2.26}$$

For vector fields, this concept is naturally extended to $(L^2(\Omega))^3$.

The vector potential $\mathbf{A}$ has to belong to a curl-conforming space:

$$\mathbf{H}_{\mathrm{curl}}(\Omega) = \left\{ \mathbf{v} \in (L^2(\Omega))^3 : \nabla \times \mathbf{v} \in (L^2(\Omega))^3 \right\}, \tag{2.27}$$

equipped with the norm $\|\mathbf{v}\|_{\mathbf{H}_{\text{curl}}} = \left(\|\mathbf{v}\|_{L^2}^2 + \|\nabla \times \mathbf{v}\|_{L^2}^2\right)^{1/2}$.
Given this definition, the test function space, enforcing the insulation condition on the external boundary, is:

$$\mathbf{V} = \mathbf{H}_{\text{curl},0}(\Omega) = \{\mathbf{v} \in \mathbf{H}_{\text{curl}}(\Omega) : \mathbf{v} \times \mathbf{n} = \mathbf{0} \text{ on } \partial\Omega\}, \tag{2.28}$$

where $\mathbf{n}$ is the outward unit normal.

The vector potential $\mathbf{T}$ appears with a dual role through the coupling term b. The regularity required for it must be :

$$\mathbf{Q} = \mathbf{H}_{\text{curl},1}(\Omega) = \{\mathbf{v} \in \mathbf{H}_{\text{curl}}(\Omega) : \mathbf{v} = \mathbf{0} \text{ on } \partial\Omega\}, \tag{2.29}$$

representing the current density in the conducting regions. No interface conditions are needed since $\mathbf{T}$ is not defined outside the conducting domain.

2.7. PEEC Variational Formulation

The variational formulation of the PEEC equation is obtained in a very similar way to the the T-A one; the main difference is constituted by the integration domain. Test the integral equation (2.21) with $\nabla \times \mathbf{t}' \in H_{\text{curl}}(\Omega_c)$, and integrate over Ω_c:

$$\begin{aligned} &\int_{\Omega_c} \frac{(\nabla \times \mathbf{T}) \cdot (\nabla \times \mathbf{t}')}{\sigma}\, d\Omega \\ &\quad + \frac{\mu_0}{4\pi}\frac{\partial}{\partial t}\int_{\Omega_c} (\nabla \times \mathbf{t}') \cdot \left(\int_{\Omega_c} \frac{\nabla \times \mathbf{T}(\mathbf{r}')}{|\mathbf{r} - \mathbf{r}'|}\, d\Omega'\right) d\Omega \\ &= -\int_{\Omega_c} \frac{\partial \mathbf{A}_0}{\partial t} \cdot (\nabla \times \mathbf{t}')\, d\Omega - \int_{\Omega_c} \nabla V \cdot (\nabla \times \mathbf{t}')\, d\Omega \;\; \forall \mathbf{t}' \in Q \end{aligned} \tag{2.30}$$

The scalar potential term can be simplified using the divergence theorem:

$$\int_{\Omega_c} \nabla V \cdot (\nabla \times \mathbf{t}')\, d\Omega = \int_{\Omega_c} \nabla \cdot (V \nabla \times \mathbf{t}')\, d\Omega - \int_{\Omega_c} V \nabla \cdot (\nabla \times \mathbf{t}')\, d\Omega \tag{2.31}$$

First of all it is possible to notice that the term $\nabla \cdot (\nabla \times \mathbf{t}')$ is identically null; in addition, applying the divergence theorem, the first term of (eq. (2.31)) can be rewritten as:

$$\int_{\Omega_c} \nabla V \cdot (\nabla \times \mathbf{t}')\, d\Omega = \int_{\partial\Omega_c} V (\nabla \times \mathbf{t}') \cdot \mathbf{n}\, dS = 0 \tag{2.32}$$

where the boundary integral vanishes because $(\nabla \times \mathbf{t}') \cdot \mathbf{n} = 0$ on any portion of $\partial\Omega_c$ (no current flowing normal to boundary). When all the above considerations are taken into account, the weak formulation of the problem can be stated as:
$\forall t \in I, \;\; ? \, \mathbf{T} \in \mathbf{Q}$:

$$\begin{aligned} &\int_{\Omega_c} \frac{(\nabla \times \mathbf{T}) \cdot (\nabla \times \mathbf{t}')}{\sigma} \, d\Omega_c \\ &\quad + \frac{\mu_0}{4\pi} \frac{\partial}{\partial t} \int_{\Omega_c} (\nabla \times \mathbf{t}') \cdot \int_{\Omega_c} \frac{\nabla \times \mathbf{T}(\mathbf{r}')}{|\mathbf{r} - \mathbf{r}'|} \, d\Omega_c' \, d\Omega_c \\ &= -\frac{\partial}{\partial t} \int_{\Omega_c} \mathbf{A_0} \cdot (\nabla \times \mathbf{t}') \, d\Omega_c \quad \forall \mathbf{t}' \in \mathbf{Q} \end{aligned} \tag{2.33}$$

Additionally, in case of a linear problem, transforming the time-domain integral equation into the corresponding frequency domain one can be computationally advantageous.
To do so, assume that a given pulse ω characterizes the forcing term, and the system response will have the same periodicity in time. In this way, all the quantities can be expressed as complex phasors, separating the spatial and time behavior [57].
For example, a single harmonic periodic time-domain field $\mathbf{F}(\mathbf{r}, t)$ can be decomposed as:

$$\mathbf{F}(\mathbf{r}, t) = F_0(\mathbf{r}) \cos(\omega t + \phi) = F_0(\mathbf{r}) \Re(e^{j\phi} e^{j\omega t}) = \tilde{\mathbf{F}}(\mathbf{r}) \Re(e^{j\omega t}).$$

Let now $\tilde{\mathbf{T}}(\mathbf{r})$ and $\tilde{\mathbf{A}}_0(\mathbf{r})$ denote the phasors associated with the current vector potential and external applied vector potential, respectively. For a time-harmonic signal with angular frequency $\omega = 2\pi f$, the temporal derivatives convert into an algebraic multiplication by a factor $j\omega$, where $j = \sqrt{-1}$.
Applying this rule to the original equation, we get the frequency-domain form:

$$\boxed{\frac{\nabla \times \tilde{\mathbf{T}}}{\sigma} + j\omega \frac{\mu_0}{4\pi} \int_{\Omega_c} \frac{\nabla \times \tilde{\mathbf{T}}(\mathbf{r}')}{|\mathbf{r} - \mathbf{r}'|} \, d\Omega_c' = -j\omega \tilde{\mathbf{A}}_0 - \nabla \tilde{V}} \tag{2.34}$$

The phasor representation captures amplitude and phase information of the steady-state oscillations, eliminating the need for time-stepping and allowing the direct computation of frequency-dependent losses. The weak formulation of the frequency domain formulation

can be obtained in the same way of eq. (2.33) as:

$$\begin{aligned}&\int_{\Omega_c} \frac{(\nabla \times \mathbf{T}) \cdot (\nabla \times \mathbf{t}')}{\sigma}\, d\Omega_c \\ &\quad + j\omega \frac{\mu_0}{4\pi} \int_{\Omega_c} (\nabla \times \mathbf{t}') \cdot \int_{\Omega_c} \frac{\nabla \times \mathbf{T}(\mathbf{r}')}{|\mathbf{r} - \mathbf{r}'|}\, d\Omega_c'\, d\Omega_c \\ &= -j\omega \int_{\Omega_c} \mathbf{A_0} \cdot (\nabla \times \mathbf{t}')\, d\Omega_c \quad \forall\, \mathbf{t}' \in H^1(\Omega_c). \end{aligned} \tag{2.35}$$

2.8. Nonlinear E-J Characteristic and Power Law

The macroscopic electrical behavior of HTS tapes can be well approximated by a strongly nonlinear relationship between the electric field $\mathbf{E}$ and the current density $\mathbf{J}$. This relationship can be described by the power law relation introduced by Rhyner [51]:

$$|\mathbf{E}| = E_0 \left(\frac{|\mathbf{J}|}{J_c} \right)^n \tag{2.36}$$

where E_0 is the critical electric field strength (defined as $100\,\mu$V/m for HTS), J_c is the critical current density, and n, typically around 40 for REBCO tapes, is the value characterizing the sharpness of the transition (see fig. 2.5) from superconducting to normal conducting state.

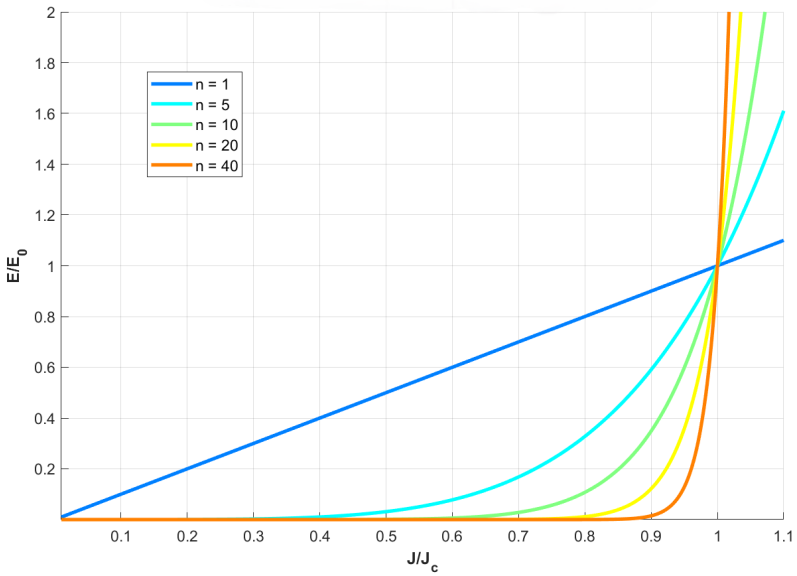


Figure 2.5: Sharpness of the transition depending on n when $\mathbf{J}/J_c \leq 1$.

Consequently, the corresponding electrical resistivity can be expressed as:

$$\rho = \frac{E_0}{J_c}\left(\frac{|\mathbf{J}|}{J_c}\right)^{n-1}. \tag{2.37}$$

When the n-value approaches infinity, this power law approximates Bean's critical state model, where $\rho = 0$ for $J < J_c$ and $\rho \to \infty$ for $J > J_c$ [4] [5]. The value of n introduces a nonlinearity which presents a significant numerical challenge due to the convergence difficulties.

The critical current density J_c represents the maximum current a superconductor can carry without losing its superconducting state. This crucial quantity is strongly dependent on the applied magnetic field, temperature, and the angle θ between the magnetic field and the tape's c-axis, which is perpendicular to the tape surface (see fig. 2.6).
From a microscopic point of view, superconductors maintain their zero-resistance properties through a phenomenon called flux pinning, where magnetic field lines become trapped or "pinned" at defects in the material's structure. These pinning sites prevent the magnetic flux from moving, which would otherwise generate what, at a macroscopic level, is perceived as resistance. The stronger the pinning, the higher the current the superconductor can carry in a magnetic field.
In the case of Fujikura ReBCO tapes [26], one of the options for the fabrication of the 40 T solenoid and its prototypes, the scaling law is derived from the flux pinning force density measurements:

$$\frac{F_p}{F_p^{\max}} = C\left(\frac{B}{B_{\max}}\right)^p\left(a - \frac{B}{B_{\max}}\right)^q \tag{2.38}$$

with p, q, a given fitting parameters. Moreover, the temperature dependence of $B_{\max}$ is approximated as:

$$B_{\max}(T) = A\left(\frac{T}{T_c}\right)^{-\alpha}\left(1 - \frac{T}{T_c}\right)^{\beta} \tag{2.39}$$

where A,α, β are fitting parameters [27].
The crystal structure of ReBCO superconductors consists of layered copper-oxide planes (the ab-plane) stacked along the c-axis. This anisotropic structure implies that the superconducting properties differ depending on field orientation. The critical current density increases significantly when the magnetic field is aligned with the ab-plane (parallel to the tape surface): when $B \parallel$ ab (at $\theta = 90$), J_c is approximately three times higher than when $B \parallel c$ (at $\theta = 0$). In this work, simulations are performed at fixed temperature ($T = 77\,\mathrm{K}$) and with the magnetic field perpendicular to the tape ($\theta = 0$), representing a

conservative approximation since J_c reaches its minimum in this configuration.

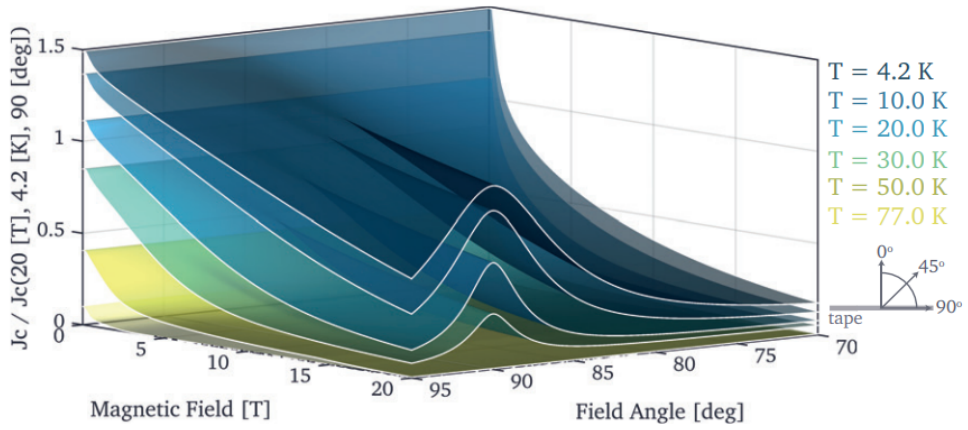


Figure 2.6: J_c surfaces at different temperatures, as function of magnetic field and angle [26].

3 | Discretization, Quadrature and Implementation

This chapter addresses the discretization and implementation aspects of the two formulations previously introduced. The COMSOL Multiphysics implementation is based on the differential form of the governing equations; therefore, the discussion focuses on three-dimensional geometry discretization and basis functions selection, without a specific treatment of the algebraic formulation.
On the other hand, the PEEC implementation in MATLAB demands a deeper analysis of its computational aspects. Consequently, a more detailed analysis of the spatial discretization, algebraic formulation, numerical quadrature rules employed for the assembly of the matrices is provided.
This differentiated approach is due to the different abstraction levels of the two development environments.

3.1. Geometries and Discretization

In this section the chosen geometries and their discretization are briefly discussed. The planar one represents an intermediate validation step of the model before moving to the final spiral configuration.

3.1.1. Target Geometries

Two main geometric configurations are considered in this work, a first test case and a real pancake coil shape:

1. **Plane geometry**: A conducting parallelepiped representing a simple test case for a first validation of the MATLAB code against an Octave PEEC and COMSOL A-V model.

2. **Spiral geometry**: A conducting path representing the realistic pancake coil configuration used in high-field superconducting magnets.

Note that both geometries satisfy the thin-domain assumptions discussed in Chapter 2, where the thickness δ is much smaller than the other characteristic dimensions.

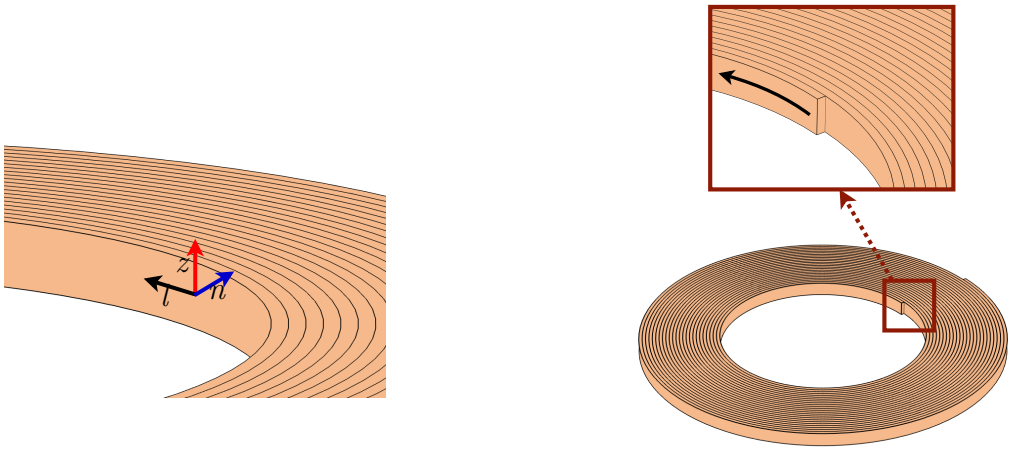


Figure 3.1: Spiral geometry visualized in COMSOL with the local reference system $\{\hat{\mathbf{r}}, \hat{\theta}, \hat{\mathbf{z}}\}$

The two geometries were discretized separating the air domain from the conductor.
The current carrying region was subdivided by means of rectangular elements in MATLAB and hexaedral ones in COMSOL. In particular, n_x elements along the x-direction and n_z elements along the z-direction were used for the square geometry; while the discretization used $n_\theta = 96$ azimuthal elements for every loop and $n_z = 4$ elements across the width of the tape for the spiral geometry.
The air, simulated only in COMSOL, was discretized with piramidal elements while hexahedral elements were used for the infinite elements. The factor 96 in the azimuthal discretization ensures an adequate resolution along the coil, while the factor 4 is the minimum discretization level that enables the simulation of two counter rotating eddy current loops.

3.1.2. Basis Functions

The finite element discretization uses different basis functions for each module:

- Quadratic edge elements (Nédelec) discretize the magnetic module computing $\mathbf{A}$;
- Linear nodal elements (Lagrange) are employed for the electric module and the PEEC implementation computing $\mathbf{T}$.

This choice of element order is necessary to avoid numerical instabilities. In fact, the system (2.22) can be interpreted as a perturbed saddle-point problem, allowing for a

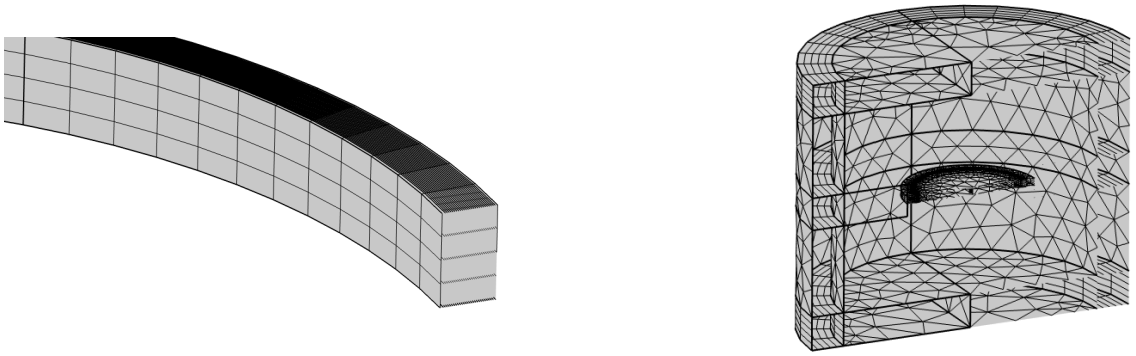


Figure 3.2: Mesh discretization of coil and air domain in COMSOL

rigorous stability analysis via Brezzi theory [12]. A requirement for the well-posedness is the satisfaction the Babuška–Brezzi (inf-sup) condition [3].
However, the coupling form b defined in (2.24) does not always satisfy this condition uniformly over the conductor region. But stability can be achieved by enriching the discrete space $\mathbf{V}_h$ with bubble functions on the conductor surfaces, which ensures the inf-sup condition is satisfied with a constant $\beta_0 > 0$ independent of both mesh size and material parameters [23].
For the PEEC T-A formulation in MATLAB, no increased element order is needed since the vector potential $\mathbf{T}$ is the only unknown.

3.2. PEEC Discretization of the Electric Vector Potential

The following section presents the finite dimensional spaces and the basis functions that were used to formulate the discrete problem associated with the PEEC integral formulation.

3.2.1. Finite Element Setting

We define the finite element space $\mathbf{V}_h$, with respect to $\{\hat{\mathbf{r}}, \hat{\theta}, \hat{\mathbf{z}}\}$, as the space of vectors having only radial non-null component, described by continuous piecewise bilinear functions over the computational mesh $\mathcal{T}_h$:

$$\mathbf{V}_h = \{\mathbf{v}_h = v_h\hat{\mathbf{r}}, v_h \in C^0(\Omega_c) : v_h|_K \in Q^1(K),\ \forall K \in \mathcal{T}_h\} \subset \mathbf{V} \tag{3.1}$$

where $Q^1(K)$ represents the space of bilinear polynomials on element K:

$$Q^1(K) = \{p(x,y) : \deg_x(p) \leq 1, \quad \deg_y(p) \leq 1\} \tag{3.2}$$

This choice ensures $\mathbf{V}_h \subset \mathbf{V} = H^1(\Omega)$, maintaining conformity with the continuous weak formulation developed in Chapter 2.
In this framework, the variational problem is projected onto the discrete space $\mathbf{V}_h$ and a finite dimensional problem is obtained:

$$\begin{aligned}
&\int_{\Omega_c} \frac{(\nabla \times \mathbf{T_h}) \cdot (\nabla \times \mathbf{t_h}')}{\sigma} \, d\Omega_c \\
&\quad + \frac{\mu_0}{4\pi} \frac{\partial}{\partial t} \int_{\Omega_c} (\nabla \times \mathbf{t_h}') \cdot \int_{\Omega_c} \frac{\nabla \times \mathbf{T_h}(\mathbf{r}')}{|\mathbf{r} - \mathbf{r}'|} \, d\Omega_c' \, d\Omega_c \\
&= -\frac{\partial}{\partial t} \int_{\Omega_c} \mathbf{A_0} \cdot (\nabla \times \mathbf{t_h}') \, d\Omega_c \quad \forall \mathbf{t_h}' \in \mathbf{V}_h.
\end{aligned} \tag{3.3}$$

Let $\{\mathbf{w}_i\}_{i=1}^N = [w_i, 0, 0]$ denote the vector basis functions with respect to $\{\hat{\mathbf{r}}, \hat{\theta}, \hat{\mathbf{z}}\}$, where $\{w_i\}_{i=1}^N$ forms a basis of $\mathbf{V}_h$ with $N = \dim(\mathbf{V}_h)$. The current density is then expanded as:

$$\mathbf{J}|_{\mathbf{V}_h} = \nabla \times \mathbf{T}_h = \sum_{k=1}^{N} T_k \, \nabla \times \mathbf{w}_k \tag{3.4}$$

where T_k are the nodal degrees of freedom representing the current vector potential at mesh nodes.

3.2.2. Reference Element Basis Functions

On the reference square $\hat{K} = [0,1] \times [0,1]$, the four nodal basis functions are defined as:

$$\hat{\phi}_i(\xi, \eta) = \begin{cases} (1-\xi)(1-\eta), & i = 1, \\ \xi(1-\eta), & i = 2, \\ \xi\eta, & i = 3, \\ (1-\xi)\eta, & i = 4. \end{cases} \tag{3.5}$$

These functions satisfy the standard finite element properties:

1. $\hat{\phi}_i(\xi_j, \eta_j) = \delta_{ij}$, with $(\xi_j, \eta_j)_{j=1}^4$ vertexes of $\hat{K}$ (Kronecker delta property);
2. $\sum_{i=1}^4 \hat{\phi}_i(\xi, \eta) = 1$ (partition of unity);

3. $\hat{\phi}_i \geq 0$ on $\hat{K}$ (non-negativity).

3.2.3. Physical Element Basis Functions

For computational efficiency, given the regularity of the spatial discretization, the basis functions can be easily defined directly in the physical domain, eliminating the need for reference element mappings.
On a generic rectangular element $[0, h_0] \times [0, h_1]$, in a local bidemensional reference system, the four nodal basis functions are:

$$\phi_i(u_0, u_1) = \begin{cases} \left(1 - \dfrac{u_0}{h_0}\right)\left(1 - \dfrac{u_1}{h_1}\right), & i = 1, \\ \dfrac{u_0}{h_0}\left(1 - \dfrac{u_1}{h_1}\right), & i = 2, \\ \dfrac{u_0}{h_0}\dfrac{u_1}{h_1}, & i = 3, \\ \left(1 - \dfrac{u_0}{h_0}\right)\dfrac{u_1}{h_1}, & i = 4. \end{cases} \tag{3.6}$$

3.3. Treatment of External Current Sources

In the integral formulation in use, an external current source can be simulated by extending the current density discrete shape by adding an extra degree of freedom.
In this way, the current density expansion can be generalized to include external electric contributions as:

$$\nabla \times \mathbf{T}_h = \sum_{k=1}^{N} T_k \nabla \times \mathbf{w}_{h,k} + T_{N+1} \nabla \times \mathbf{w}_{N+1} \tag{3.7}$$

where $\mathbf{w}_{N+1}$ is an additional basis function designed to satisfy:

$$\nabla \times \mathbf{w}_{N+1}\big|_{\partial\Omega} = \frac{\mathbf{J}_0}{T_{N+1}} \tag{3.8}$$

and representing the known contribution of an imposed transport current. For a transport current $\mathbf{J}_0 = [0, J, 0]^T$ in the local coordinate system $\{\hat{\mathbf{r}}, \hat{\theta}, \hat{\mathbf{z}}\}$, a possible choice for the additional basis function is:

$$\mathbf{w}_{N+1} = \left[\frac{z}{H}, 0, 0\right]^T, \text{ with associated weight } \quad T_{N+1} = J \cdot H \tag{3.9}$$

where H represents the major transversal dimension with respect to the current injection.

3.4. Algebraic formulation

Substituting the expression eq. (3.7) into the variational form eq. (3.3) and choosing as test functions the same basis functions $\mathbf{t}_h$ (applying a Galerkin procedure [64]), N scalar equations in the N unknown coefficients T_i are produced.
The result is an algebraic system $\mathbf{MT} = \mathbf{b}$, where the matrix $\mathbf{M}$ and vector $\mathbf{b}$ are computed from integral expressions of the basis functions. Solving this linear system yields the coefficients, and thus the approximate solution $\mathbf{T}_h$. In the examined case, the algebraic system is:

Find $\mathbf{T}(t) \in \mathbb{R}^N$ such that:

$$\mathbf{R}\mathbf{T}(t) + \mathbf{L}\frac{\partial \mathbf{T}(t)}{\partial t} = -\frac{\partial \mathbf{A}_0}{\partial t} \tag{3.10}$$

Where the system matrices are defined through the following integrals:

Resistance Matrix:

$$\mathbf{R}_{ij} = \int_{\Omega_c} \frac{(\nabla \times \mathbf{w}_i) \cdot (\nabla \times \mathbf{w}_j)}{\sigma} \, d\Omega_c \tag{3.11}$$

Inductance Matrix:

$$\mathbf{L}_{ij} = \frac{\mu_0 t}{4\pi} \int_{\Omega_c} \left(\nabla \times \mathbf{w}_i(\mathbf{r}) \cdot \int_{\Omega_c'} \frac{\nabla \times \mathbf{w}_j(\mathbf{r}')}{|\mathbf{r} - \mathbf{r}'|} \, d\Omega_c' \right) d\Omega_c \tag{3.12}$$

External Field Vector:

$$\mathbf{A}_{0,i} = \int_{\Omega_c} (\nabla \times \mathbf{w}_i) \cdot \mathbf{A}_0 \, d\Omega_c \tag{3.13}$$

The resulting system matrices exhibit some relevant properties. The resistance matrix $\mathbf{R}$ is symmetric, positive definite and sparse. The inductance matrix $\mathbf{L}$ is also symmetric and positive definite but full, as it contains the global mutual inductive interactions. Additionally, it involves a weakly singular integral when computing the self-inductance ($\Omega = \Omega'$), requiring special numerical integration techniques. In the frequency-domain algebraic formulation, obtained from eq. (2.35), in the same way of eq. (3.10), the unknown is a vector $\mathbf{T}$:

$$(\mathbf{R} + j\omega\mathbf{L})\mathbf{T} = -j\omega\mathbf{A}_0. \tag{3.14}$$

3.4.1. Extended Formulation with Imposed Current

When external current densities are included via equation (3.7), assuming no external magnetic fields are applied ($\mathbf{A}_0 = \mathbf{0}$), two additional forcing terms appear in the algebraic formulation.
The discrete system becomes:

$$\sum_{j=1}^{N} \left(\mathbf{R}_{ij} T_j + \mathbf{L}_{ij} \frac{\partial T_j}{\partial t} \right) = \\ - T_{N+1} \mathbf{S}_{r,i} - \frac{\partial T_{N+1}}{\partial t} \mathbf{S}_{l,i}, \quad \forall i = 1, \ldots, N \tag{3.15}$$

where:

$$\mathbf{S}_{r,i} = \int_{\Omega} \frac{(\nabla \times \mathbf{w}_{N+1}) \cdot (\nabla \times \mathbf{w}_i)}{\sigma} \, d\Omega \tag{3.16}$$

$$\mathbf{S}_{l,i} = \frac{\mu_0 t}{4\pi} \int_{\Omega} \nabla \times \mathbf{w}_i \cdot \left(\int_{\Omega'} \frac{\nabla \times \mathbf{w}_{N+1}}{r} \, d\Omega' \right) d\Omega. \tag{3.17}$$

3.5. Weakly Singular Integral Quadrature

This section analyzes the two different cases that were encountered while assembling the matrices and vectors of the algebraic formulation.
Two distinct quadrature rules were employed in the assembly phase, as the singular case $\Omega = \Omega'$ in the assembly of L has to be treated separately.
The Gauss-Legendre rule was used to assemble R, the mutual inductance contribution of L ($\Omega \neq \Omega'$) and the right hand side. The Duffy quadrature rule was employed for the self-inductance contributions.

3.5.1. Duffy Transformation for Singular Integrals

The Duffy transformation provides an effective technique for handling weakly singular integrals of the form $1/r^{\alpha}$ on triangular domains [44]. This transformation to eliminate power singularities can be split in the following steps [44]:

1. **Domain subdivision**: Divide the domain into triangular sub-elements with the singularity lying at a vertex of the subdivisions;
2. **Affine mapping**: Transform each triangle to the unit reference square;

3. **Nonlinear transformation**: Apply the change of variables:

$$u = x^{\beta}, \quad v = x^{\beta} y \tag{3.18}$$

where β is chosen to optimize convergence;

4. **Quadrature application**: Apply Gaussian quadrature to the transformed integral and map points and weights back to the original element.

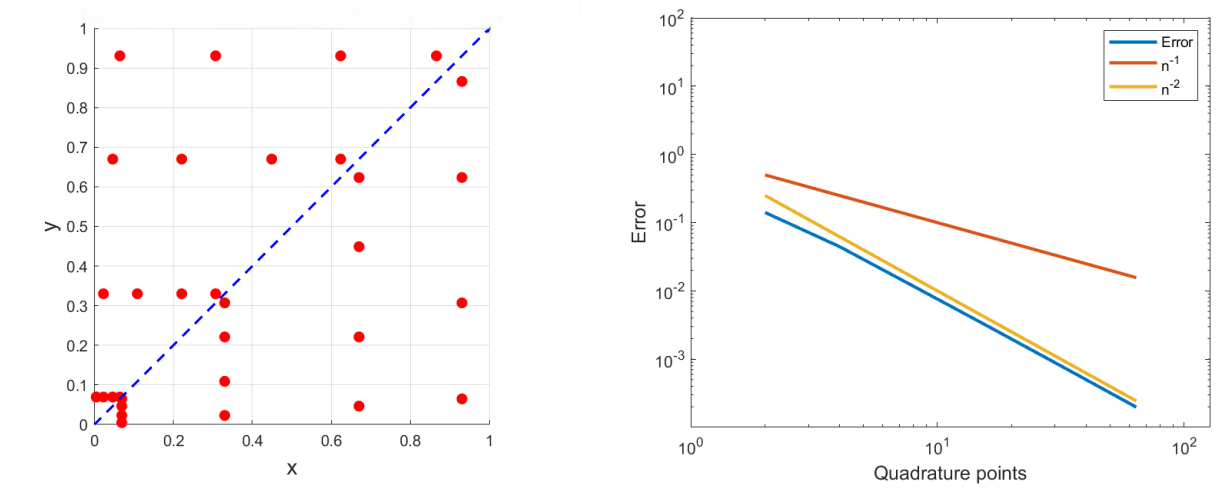
Moreover, for singularities of the type $\frac{1}{r^{\alpha}}$, the best transformation parameter can be proved to be:

$$\beta = \begin{cases} 1, & \text{if } \alpha = 1 \text{ (standard Duffy)} \\ 2, & \text{if } \alpha = 1/2 \\ 3, & \text{if } \alpha = 1/3, 2/3, 4/3 \end{cases} \tag{3.19}$$

This choice ensures that the transformed integrand has integer or simple fractional powers, leading to optimal convergence rates. As first test, the Duffy transformation was tested using the following weakly singular integral, whose exact value is known:

$$I = \int_0^1 \int_0^1 \frac{y}{\sqrt{x^2 + y^2}} \, dx \, dy = \frac{1}{2} \left(\sqrt{2} + \operatorname{arctanh}\left(\frac{1}{\sqrt{2}} \right) - 1 \right) \tag{3.20}$$

The numerical results demonstrate quadratic convergence with respect to the number of integration points n_{sp}, as reported in fig. 3.3.



(a) (b)

Figure 3.3: Duffy nodes for a singularity in the origin (a); Quadrature error (b)

3.5.2. Self inductance computation:

In order to compute the self inductance integral, it is first necessary to understand where the singularity is located.
If an element $\Omega = \tilde{\Omega}$ is fixed, as the outer integral of L is computed with a Gauss-Legendre (GL) quadrature rule, at every iteration the singularity is located at the quadrature nodes $\mathbf{x}_p$:

$$\mathbf{L}_{ij} = \frac{\mu_0 t}{4\pi} \sum_p \nabla \times \mathbf{w}_i(\mathbf{x}_p) \left(\int_{\tilde{\Omega}} \frac{\nabla \times \mathbf{w}_j(\mathbf{r}')}{|\mathbf{x}_p - \mathbf{r}'|} d\tilde{\Omega} \right) w_p \tag{3.21}$$

where w_p are the GL quadrature weights.
Set now $\mathbf{x}_p$ to a fixed GL node and consider a single iteration of the sum over p. The quantity that has to be computed is:

$$\mathbf{L}_{ij}^p = \frac{\mu_0 t}{4\pi} \nabla \times \mathbf{w}_i(\mathbf{x}_p) \left(\int_{\tilde{\Omega}} \frac{\nabla \times \mathbf{w}_j(\mathbf{r}')}{|\mathbf{x}_p - \mathbf{r}'|} d\tilde{\Omega} \right) w_p \tag{3.22}$$

$$= \frac{\mu_0 t}{4\pi} \nabla \times \mathbf{w}_i(\mathbf{x}_p) \left(\sum_q \frac{\nabla \times \mathbf{w}_j(\mathbf{x}_q)}{|\mathbf{x}_p - \mathbf{x}_q|} w_q \right) w_p \tag{3.23}$$

The second set of quadrature nodes $\mathbf{x}_q$ will be computed as Duffy nodes distributed around the singularity. However, being $\mathbf{x}_p$ a GL point, it is internal to the element $\tilde{\Omega}$, so in this case a subdivision in four triangles (instead of just two) is required.

3.6. Numerical Implementation of PEEC Method for Spiral HTS Coils and Rectangular Conductors

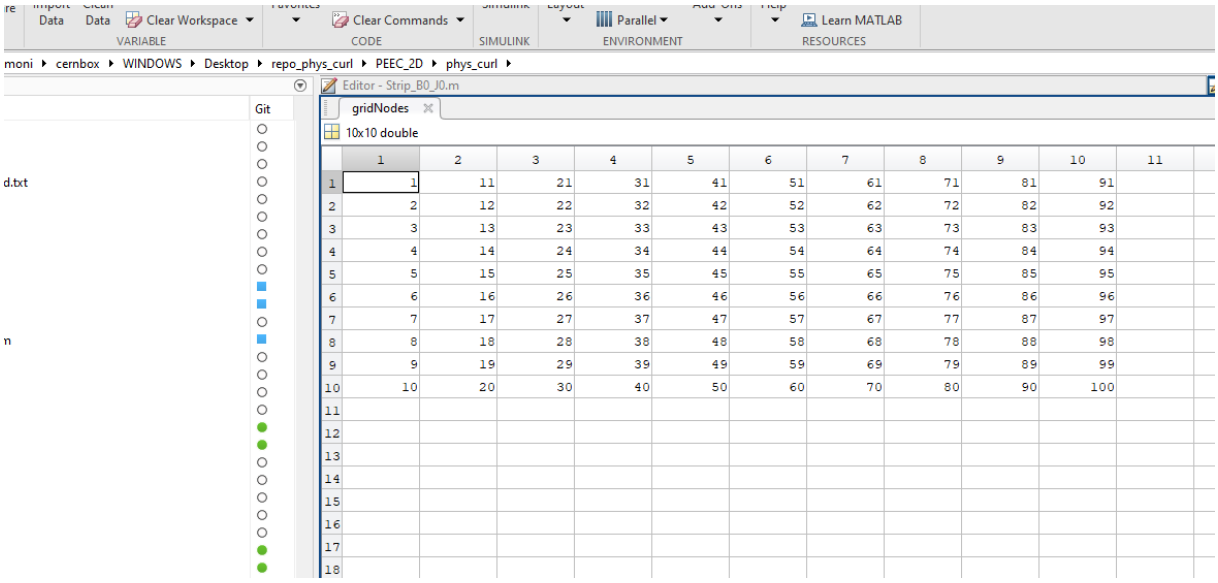
The electromagnetic problem is solved using a MATLAB implementation of the two-dimensional PEEC method, which can be applied to both spiral and rectangular geometries. The code computes the frequency and time domain distribution of the electric vector potential, by assembling resistance and inductance matrices, and then solving the resulting linear system. Two problems are supported: a rectangular conductor subject to external magnetic field or imposed current density, and multi-turn spiral coils focused on the current injecting scenario.

3.6.1. Geometry Construction

In this section the generation of the two geometries is illustrated together with the parameters that can be set.

For rectangular conductors, the geometry is generated via `generate_3D_Rectangular_mesh`, which discretizes a rectangular domain of dimensions L_x m (longitudinal), L_z m (transversal), and thk m (thickness). The mesh is uniform with size $h_x = L_x/(n_x - 1)$ and $h_z = L_z/(n_z - 1)$, where n_x and n_z are the node counts per direction.
The mesh generator creates a structured quadrilateral grid stored as two sets of arrays nodes, elements; each node stores (x, y, z) coordinates in Cartesian form while elements is the connectivity matrix in which each element is associated with the respective nodes constituting its vertexes.
The code also supports the creation of two rectangular conductors separated by distance d m via separate calls to `generate_3D_Rectangular_mesh`; nodes and elements data structures are concatenated with an appropriate index remapping to form a coupled multi-conductor system.
Finally, a double possible scenario is supported by setting $pb = 1$ for applying an external magnetic field or $pb = 2$ to impose an external current. The `gridNodes` matrix of size $(n_z) \times (n_x)$ is useful to visualize the nodes by spatial position, enabling an immediate identification of the boundary nodes along left, right, top, and bottom edges.

The spiral coil geometry is generated via `generate_3D_spiral_mesh`, which creates a three-dimensional mesh representing $\mathrm{n_{loops}}$ turns wound with constant pitch. The mesh is parametrized along two dimensions: the azimuthal direction with n_θ subdivisions per turn, the axial direction ($\mathrm{n}_z = 4$ nodes along the coil height), the radial direction is not discretized due to the thin sheet approximation.



	1	2	3	4	5	6	7	8	9	10	11
1	1	11	21	31	41	51	61	71	81	91	
2	2	12	22	32	42	52	62	72	82	92	
3	3	13	23	33	43	53	63	73	83	93	
4	4	14	24	34	44	54	64	74	84	94	
5	5	15	25	35	45	55	65	75	85	95	
6	6	16	26	36	46	56	66	76	86	96	
7	7	17	27	37	47	57	67	77	87	97	
8	8	18	28	38	48	58	68	78	88	98	
9	9	19	29	39	49	59	69	79	89	99	
10	10	20	30	40	50	60	70	80	90	100	
11											
12											
13											
14											
15											
16											
17											
18											

Figure 3.4: Example of gridNodes with 10 nodes in both directions

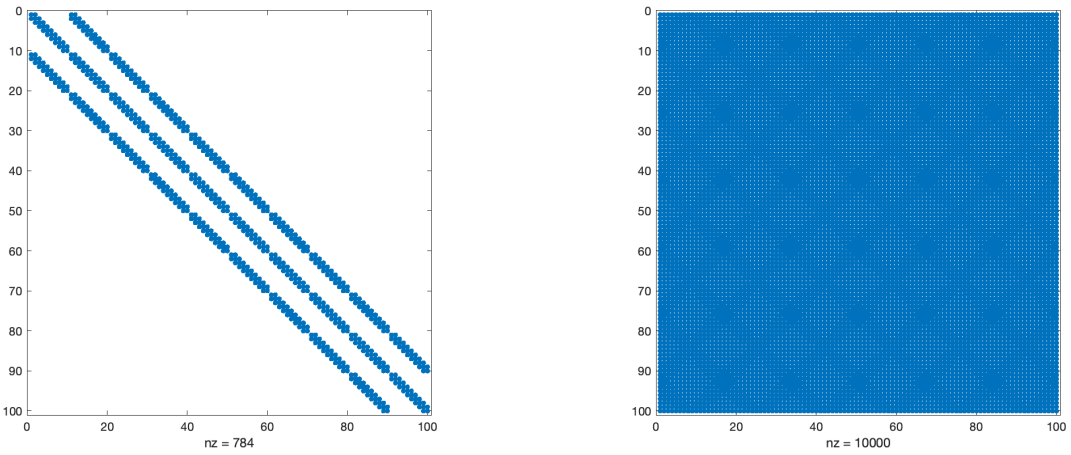
The coil has outer starting radius $r_0 = 3 \times 10^{-2}$ m and $t = 8 \times 10^{-5}$ m is the thickness of the tape and radial contraction per turn. The coil height is fixed at $H = 4 \times 10^{-3}$ m.
As before, `gridNodes` is a matrix of size $(n_z + 1) \times (n_\theta \times n_{\text{loops}} + 1)$ provides directly the spatial indexing for identifying the position of each degree of freedom.

3.6.2. Matrix Assembly

The assembly of the resistance and inductance matrix is now illustrated, for the latter the different assembly methods will be shown, along with a comparison of the computational time required.

Resistance

The resistance matrix $\mathbf{R}$ is assembled by integrating the curl-curl bilinear form over all elements.
In the beginning, for each element e, the Jacobian matrix $\mathbf{J}_e$ was computed from the mapping between reference coordinates $(\xi, \eta) \in [0, 1]^2$ and physical coordinates (x, y, z). The curl operator was then transformed from the reference element to the physical domain via the Jacobian inverse map $\mathbf{J}_e^{-T}$.
Later on, given the regular space orientation of the mesh elements, with the normal always pointing in the radial direction, the basis functions were rewritten in the physical domain, eliminating the need for a reference mapping. Gauss-Legendre or trapezoidal quadrature with $nsp = 2$ points per direction (4 total per element) were employed to evaluate the



(a) (b)

Figure 3.5: Sparsity pattern of the resistance (a) and inductance (b) matrices

element matrix, ensuring the exact computation of the integral as:

$$\mathbf{R}_{ij}^{e} = \frac{1}{\sigma} \sum_{q=1}^{4} (\nabla \times \phi_i^e(\mathbf{x}_q)) \cdot (\nabla \times \phi_j^e(\mathbf{x}_q))\, w_q \,, \tag{3.24}$$

where w_q and $\nabla \times \phi_i^e(\mathbf{x_q})$ are the curl basis functions evaluated at the quadrature point $\mathbf{x}_q$.

Rather than allocating a dense $N \times N$ matrix, the code uses sparse triplet format: three one-dimensional arrays store row indices $\mathbf{I}$, column indices $\mathbf{J}$, and values $\mathbf{V}$ for all non-zero entries. After element-wise assembly, the global sparse matrix is constructed via `sparse(I, J, V, n_dof, n_dof)`, with n_{dof} number of degrees of freedom.

This reduces memory from $\mathcal{O}(N^2)$ to $\mathcal{O}(N)$ and avoids expensive operations on zero entries during all the following operations. In the linear case, the resistance matrix is computed once per simulation since it is independent of frequency.

Self-Inductance

Self-inductance is computed via `L_self_assembly_sparse`, which evaluates the weakly singular integral over coincident elements using the Duffy transformation. For a single element e, the contribution is:

$$\mathbf{L}_{ij}^{e,\text{self}} = \frac{\mu_0 t}{4\pi} \sum_p \nabla \times \phi_i^e(\mathbf{x}_p) \cdot \sum_q \left(\frac{\nabla \times \phi_j^e(\mathbf{x}_q)}{|\mathbf{r} - \mathbf{r}'|}\, w_q \right) w_p \,, \tag{3.25}$$

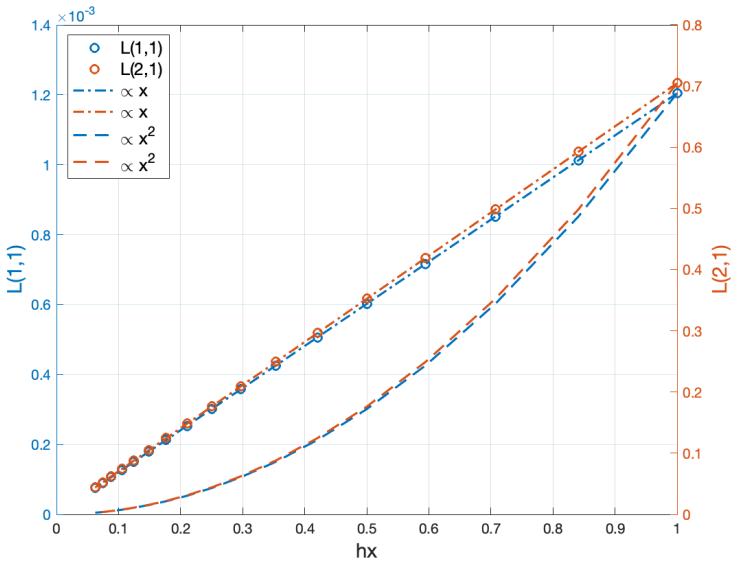
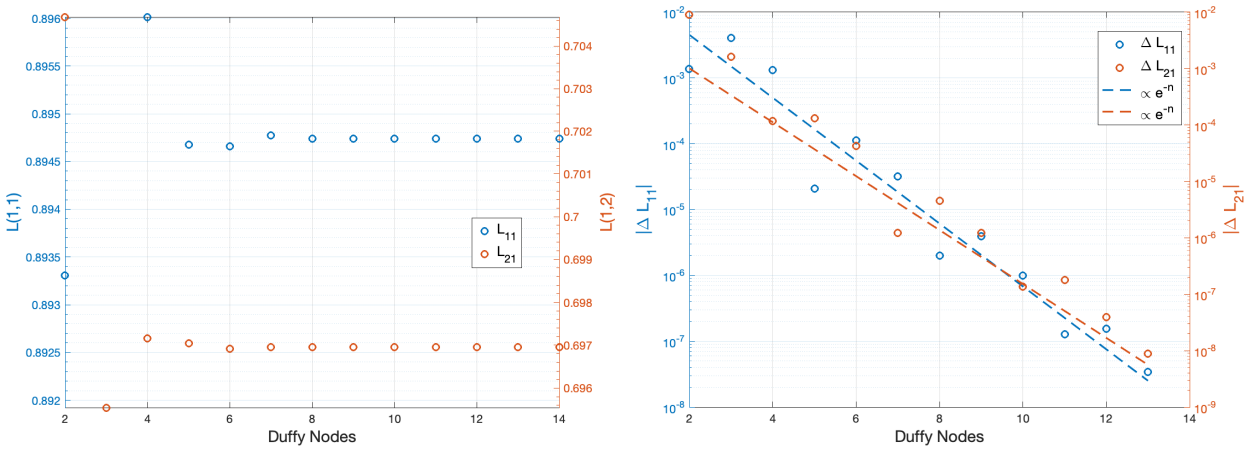


Figure 3.6: L^{self} entries behavior with respect to the mesh element's size

where the $1/|\mathbf{r}-\mathbf{r}'|$ kernel is singular when $\mathbf{r}=\mathbf{r}'$.
The Duffy transformation splits the integration domain into four triangular subregions by drawing diagonals from the singular point; for each triangle, a nonlinear coordinate transformation converts the integrand into a non singular form.
Precomputed Duffy nodes and weights (`TriangleSplittingDuffyNodes`) provide quadrature variables with $nsp2 = 10$ points per direction, yielding $4\times10^2 = 400$ total integration points per element. The self-inductance matrix is sparse because any e'$\neq$ e do not provide a contribution. It is worth conducting two different analysis on the self inductance:

1. analyzing the convergence with respect to the number of Duffy nodes;
2. understanding if a relationship between the matrix L^{self} and the rectangular mesh elements can be found, to then predict it (instead of compute it).

For the first case the square domain [0,1]x[0,1] was considered, and then its dimensions were progressively reduced up to 1/16th of the original size. In this case, L^{self} is a simple 4 by 4 matrix, as the domain is considered a unique mesh element; its the first diagonal and extra-diagonal entries show the behavior illustrated in 3.6. The self inductance shows a linear dependency from the mesh size, when both dimensions are reduced concurrently. This clear trend could be studied further, but it's a good sign towards the prediction of the self-inductance matrix. For the second analysis, the domain was fixed to the unit square, and the number of Duffy nodes was increased to study the convergence of the same two entries of 3.6.



(a) (b)

Figure 3.7: Convergence of the self inductance with respect to the number of Duffy nodes, in absolute terms (a) and its increment (b)

The self-inductance integrals converge exponentially with the number of Duffy quadrature nodes, as evidenced by the linear decay in the semi-logarithmic convergence plot fig. 3.7. This exponential rate is achieved because the Duffy transformation regularizes the singularity, allowing the GL quadrature to exploit such smoothness.

Mutual Inductance

Mutual inductance couples all element pairs (e_1, e_2) with $e_1 \neq e_2$:

$$\mathbf{L}_{ij}^{e_1,e_2,\text{mutual}} = \frac{\mu_0 t}{4\pi} \sum_p \nabla \times \phi_i^{e_1}(\mathbf{x}_p) \cdot \left(\sum_q \frac{\nabla \times \phi_j^{e_2}(\mathbf{x}_q)}{|\mathbf{x}_p - \mathbf{x}_q|} w_q \right) w_p \,, \tag{3.26}$$

with a non-singular kernel for distinct elements. The mutual inductance assembly dominates the computational cost due to $\mathcal{O}(N_{\text{el}}^2)$ element pairs. To accelerate the process, after vectorizing the operations in the first version of this function, the MATLAB parallelization was employed, providing a first speedup, before arriving at function `L_mutual_assembly_phys6_coder`, which is compiled to native machine code via MATLAB Coder, providing an additional relevant speedup shown in fig. 3.8.
The MATLAB Coder generates optimized C code that distributes the outer for loop across available processor cores; each core computes independent element-pair contributions and writes to local buffers, which are then merged after completion.
The compiled function is invoked as a MEX (MATLAB Executable) file: MATLAB passes all the needed arguments to the native binary, which operates on them in memory and re-

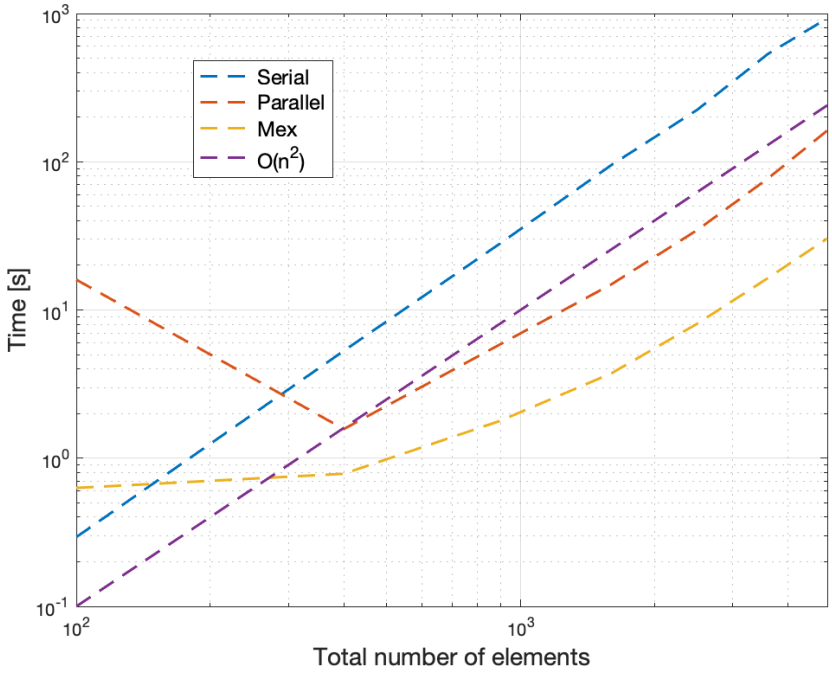


Figure 3.8: Assembly time of the mutual inductance matrix

turns sparse triplet arrays (I, J, V). The returned triplet is finally assembled into a sparse matrix via `sparse(I, J, V, n_dof, n_dof)`, and symmetrized by adding the transpose: $\mathbf{L}_{\mathrm{m}} = \mathbf{L}_{\mathrm{m1}} + \mathbf{L}_{\mathrm{m1}}^T$. The final inductance matrix is obtained by summing up the self and mutual inductance matrices.

3.6.3. Right-Hand Side Assembly

When an external uniform magnetic field $\mathbf{B}_0 = [B_{0x}, B_{0y}, B_{0z}]^T$ is applied, the corresponding vector potential is:

$$\mathbf{A}_0(\mathbf{r}) = \frac{1}{2} \begin{bmatrix} B_{0y}z - B_{0z}y \\ B_{0z}x - B_{0x}z \\ B_{0x}y - B_{0y}x \end{bmatrix} \tag{3.27}$$

This choice ensures $\nabla \times \mathbf{A}_0 = \mathbf{B}_0$ and satisfies the Coulomb gauge $\nabla \cdot \mathbf{A}_0 = 0$.

For time-varying external fields $\mathbf{B}_0(t)$, the source term in the T-A equation becomes:

$$-\frac{\partial \mathbf{A}_0}{\partial t} = -\frac{1}{2}\begin{bmatrix} \dfrac{dB_{0y}}{dt}z - \dfrac{dB_{0z}}{dt}y \\ \dfrac{dB_{0z}}{dt}x - \dfrac{dB_{0x}}{dt}z \\ \dfrac{dB_{0x}}{dt}y - \dfrac{dB_{0y}}{dt}x \end{bmatrix} \tag{3.28}$$

The first case that was simulated and validated has an external magnetic field $\mathbf{B}_0 = (B_{0x}, B_{0y}, B_{0z})$ as forcing term; the associated right-hand side is assembled from the vector potential $\mathbf{A}_0$ and computed via `assemble_A0`.
In the frequency-domain the right-hand side is

$$\mathbf{f} = -j\omega \mathbf{A}_0, \tag{3.29}$$

where the imposed vector potential forces the system at an angular frequency $\omega = 2\pi f_0$. No lifting function is required since the boundary condition is homogeneous ($T = 0$ on all boundaries, no current flow through the boundary $\partial\Omega$).

The second possible scenario is the injection (and extraction) of a current density in the geometry. In order to achieve such result (either into rectangular conductors or spiral coils), a lifting function $\mathbf{w}_{N+1}(\xi, \eta) = [w_{N+1}, 0, 0]$, having only normal non-null radial component, enforces the boundary condition.
For rectangular conductors, $w_{N+1}(\xi, \eta) = \eta / L_z$ satisfies $w_{N+1} = 0$ at bottom and $w_{N+1} = 1$ at top; while for spiral coils, $w_{N+1}(\xi, \eta) = \eta / H$ with H the coil height (L_z and H play obviously the same geometric role).
The curl of such function is $\nabla \cdot w_{N+1} = [1/H, 0, 0]$ respectively, and the resistive right-hand side is:

$$\mathbf{R}_{\mathrm{rhs,i}} = \frac{1}{\sigma}\int_{\Omega_\mathrm{c}} (\nabla \times \mathbf{w}_{N+1}) \cdot (\nabla \times \mathbf{w}_i)\, d\Omega_\mathrm{c}, \tag{3.30}$$

computed via `R_rhs_assembly` and stored as a dense vector of length n_{dof}. The inductive right-hand side couples the lifting function to the curl of all basis functions:

$$\mathbf{L}_{\mathrm{rhs,j}} = \frac{\mu_0 t}{4\pi}\int_{\Omega_\mathrm{c}}\int_{\Omega_\mathrm{c}} \frac{(\nabla \times \mathbf{w}_{N+1}) \cdot (\nabla \times \mathbf{w}_j)}{|\mathbf{r} - \mathbf{r}'|}\, d\Omega_\mathrm{c}'\, d\Omega_\mathrm{c}, \tag{3.31}$$

evaluated via `L_rhs_assembly_mutual_coder` and `L_rhs_assembly_self_coder` (both compiled via MATLAB Coder for efficiency).

The complete frequency domain right-hand side vector is obtained as:

$$\mathbf{rhs} = -T_{n1}(\mathbf{R}_{\text{rhs}} + j\omega\mathbf{L}_{\text{rhs}}), \tag{3.32}$$

where $T_{n1} = J_0 \cdot H$ scales the unitary additional degree of freedom to its correct amplitude.

3.6.4. Enforcement of the boundary condition

The Dirichlet boundary conditions on $\mathbf{T}$ are enforced by keeping in the linear system only the free degrees of freedom for which are unknown. The boundary DoFs in which the value of the electric vector potential is fixed, are removed from the system producing the reduced matrices $\mathbf{R}_{\text{free}}$, $\mathbf{L}_{\text{free}}$, and the right-hand side $\mathbf{f}_{\text{free}}$.
After solving for the unknowns, the boundary values are appended to recover the full solution vector. For cases with multiple conductors (e.g., two rectangular conductors), boundary nodes are identified for each conductor separately and removed as a unified set.

3.6.5. Problem resolution

The frequency-domain problem for the free degrees of freedom reads:

$$(\mathbf{R}_{\text{free}} + j\omega\mathbf{L}_{\text{free}})\mathbf{T}_{\text{free}} = \mathbf{rhs}_{\text{free}}. \tag{3.33}$$

The system is solved directly via the MATLAB backslash operator $\mathbf{T}_{\text{free}} = \mathbf{M} \backslash \mathbf{rhs}_{\text{free}}$, which automatically selects the most appropriate linear solver based on matrix properties. For the complex symmetric impedance matrix $\mathbf{M} = \mathbf{R}_{\text{free}} + j\omega\mathbf{L}_{\text{free}}$, the backslash operator computes a LU factorization $\mathbf{M} \approx \mathbf{LU}$ using approximate minimum degree reordering to minimize fill-in, then solves via forward and backward substitution: $\mathbf{T}_{\text{free}} = \mathbf{U}^{-1}(\mathbf{L}^{-1}\mathbf{rhs}_{\text{free}})$. For ill-conditioned systems at high frequencies, an iterative refinement is automatically applied: after the factorization-based solution $\mathbf{T}_0$ is computed, the residual $\mathbf{r} = \mathbf{f} - \mathbf{M}\mathbf{T}_0$ is evaluated and the correction $\Delta\mathbf{T} = \mathbf{M}^{-1}\mathbf{r}$ is solved and added iteratively until reaching convergence.

3.6.6. Losses and magnetic field computation

Once $\mathbf{T}$ is obtained, the current density is reconstructed as $\mathbf{J}(\mathbf{r}) = \nabla \times \mathbf{T}(\mathbf{r})$ at each node via basis function derivatives, and losses are computed by numerical integration of

$$P = \frac{t}{2}\int_{\Omega_c} \frac{|\mathbf{J}|^2}{\sigma}\, d\Omega_c = \frac{t}{2}\int_{\Omega_c} \sum_i \frac{|\nabla \times \mathbf{w}_i\, T_i|^2}{\sigma} d\Omega_c = \frac{t}{2}\sum_p \sum_i \frac{|\nabla \times \mathbf{w}_i(\mathbf{x}_p)\, T_i|^2}{\sigma} w_p \tag{3.34}$$

with the integral being evaluated using the Gauss quadrature rule.

Additionally, the magnetic field at an arbitrary observation point $\mathbf{x}_0$ can be computed by means of the numerical integration of the Biot-Savart law using the current density distribution $\mathbf{J}(\mathbf{r})$ obtained from the PEEC solution.
The function `compute_magnetic_field_x0` evaluates:

$$\begin{aligned}\mathbf{B}(\mathbf{x}_0) &= \frac{\mu_0 \cdot \mathrm{t}}{4\pi} \int_{\Omega_\mathrm{c}} \frac{\mathbf{J}(\mathbf{r}) \times (\mathbf{x}_0 - \mathbf{r})}{|\mathbf{x}_0 - \mathbf{r}|^3}\, d\Omega_\mathrm{c} \\ &= \frac{\mu_0 \cdot \mathrm{t}}{4\pi} \int_{\Omega_\mathrm{c}} \sum_i \frac{\nabla \times \mathbf{w}_i \times (\mathbf{x}_0 - \mathbf{r})}{|\mathbf{x}_0 - \mathbf{r}|^3}\, T_i\, d\Omega_\mathrm{c} \\ &= \frac{\mu_0 \cdot \mathrm{t}}{4\pi} \sum_p \sum_i \frac{\nabla \times \mathbf{w}_i(\mathbf{x}_p) \times (\mathbf{x}_0 - \mathbf{x}_p)}{|\mathbf{x}_0 - \mathbf{x}_p|^3}\, T_i\, w_p\, d\Omega \end{aligned} \tag{3.35}$$

For each element, the current density is reconstructed at every quadrature point $\mathbf{x}_p$ as $\mathbf{J}(\mathbf{x}_p) = \sum_i (\nabla \times \phi_i)(\mathbf{x}_p)\, T_i + (\nabla \times w_{N+1})\, T_{N+1}$, combining contributions from the potential $\mathbf{T}$ and the lifting function. The distance vector $\mathbf{r} = \mathbf{x}_0 - \mathbf{r}_p$ and its magnitude are computed for each quadrature point, then the cross product $\mathbf{J}(\mathbf{r}_p) \times \mathbf{r}$ is divided by $\mathbf{r}^3$ and integrated.
This computation enables the post-processing of PEEC solutions to evaluate magnetic field at every desired point, allowing the comparison with experimental Hall probe measurements.

3.6.7. Time-Domain Extension

The code framework supports time-domain transient simulations via `Trying_time_dep.m`. The frequency-domain system is extended to time by replacing $j\omega$ with the time-derivative operator ∂_t, yielding:

$$\mathbf{R}\,\mathbf{T}(\mathbf{x}, t) + \mathbf{L}\,\frac{\partial \mathbf{T}(\mathbf{x}, t)}{\partial t} = \mathbf{rhs}(t), \tag{3.36}$$

where $\mathbf{rhs}(t)$ contains the time-dependent boundary conditions (e.g., ramp or step current). Implicit time-stepping schemes as backward Euler or Crank-Nicolson discretize this as a sequence of linear systems, solved repeatedly at each time step. Once $\mathbf{T}$ is obtained for a specific time step, the associated Joule losses and magnetic field in any desired point are computed in order to be able to track their evolution over time.

3.7. COMSOL Reference Model Configuration

The COMSOL model solves the coupled electromagnetic problem for conductors using a physics module from the AC/DC Module and another one belonging to the Mathematics Module. Magnetic Fields, Currents Only (mfco) computes the quasi-static magnetic field in the conductor domains via the vector potential formulation: $\nabla \times (\nabla \times \mathbf{A}) = \mu_0 \mathbf{J}$, where the magnetic vector potential $\mathbf{A} = (A_x, A_y, A_z)$ is discretized with quadratic edge element shape functions.

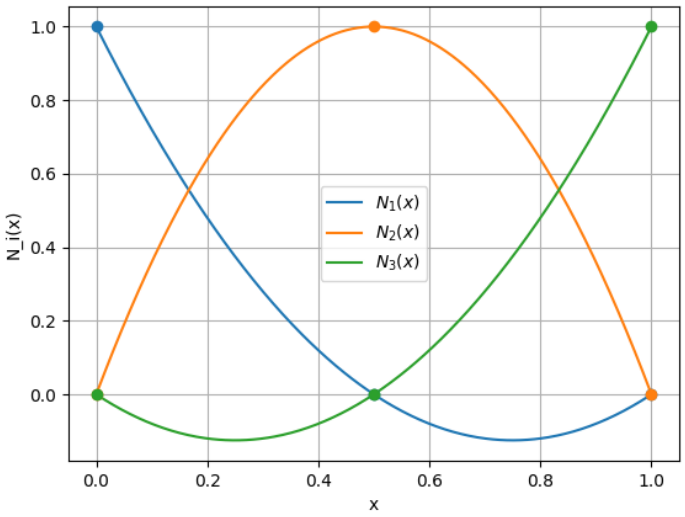


Figure 3.9: Second order Lagrangian basis function on [0,1]

The current density $\mathbf{J}$ is imposed via an external current density boundary condition, parameterized in cylindrical coordinates as $\mathbf{J} = (0, j_\theta, j_z)$, where j_θ and j_z provided the analytical description of the reference system in which they are expressed (no need, in this case, to re-express them through their Cartesian components).
Lastly, Magnetic Fields, Currents Only 2 extends the solution to the surrounding air and infinite elements using an identical discretization of the magnetic vector potential.
The General Form PDE module is used to solve the electric field equation in the conductor domains using linear Lagrange shape functions for the dependent variable T.
The conservative flux is representative of the term $\nabla \times (\rho(\mathbf{J}, \mathbf{B})\,\mathbf{J})$, where the resistivity ρ depends on current density and field magnitude via power-law E-J. On the other hand, the source term contains the time derivative of magnetic flux: $f = -\partial(\mathbf{B} \cdot \mathbf{n})/\partial t$.The initial values are set to zero for all dependent variables.
Dirichlet boundary conditions enforce the current flow by setting $T = I_0(t)/\text{thk}$ on the

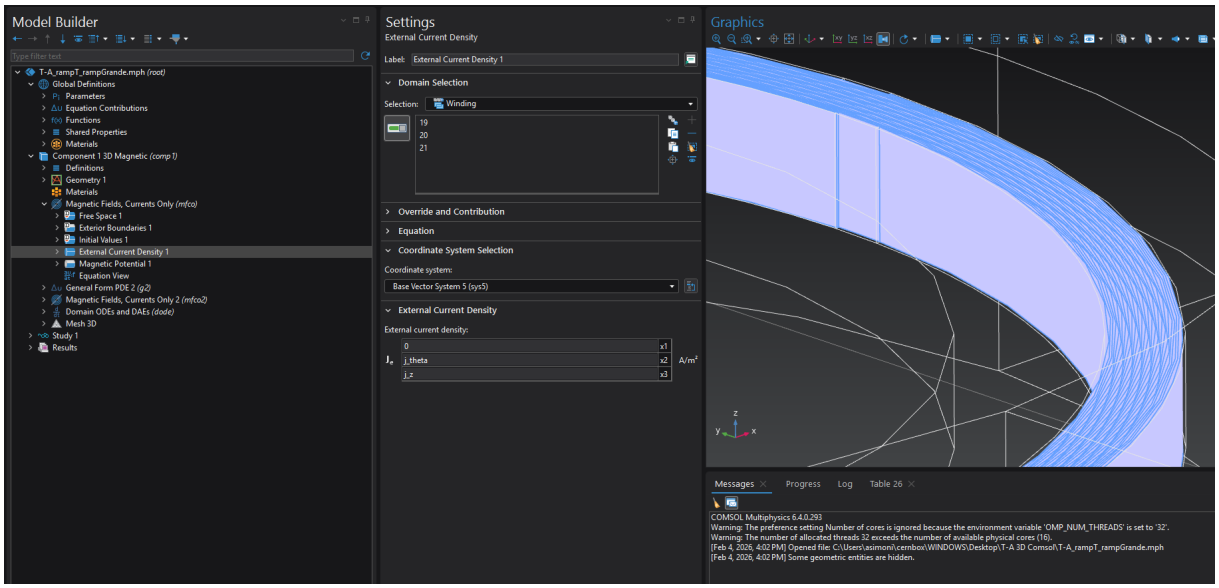


Figure 3.10: Imposition of the external current density as forcing term to solve the magnetic equation

upper surface of the coil (see 3.11) and zero potential $T = 0$ on the bottom one. The time-dependent nonlinear problem is solved with a fully coupled approach [18].
The time derivative is discretized using a fixed BDF scheme of order one [19] [28] , with a strictly controlled automatic time-stepping algorithm and a fixed tolerance, ensuring that rapid transients or sudden changes in the solution are accurately captured. At each time step, the resulting nonlinear algebraic system is assembled and solved monolithically.
The linear subproblems arising inside the nonlinear iterations are handled by a direct solver of the PARDISO type, performing a sparse factorization that is well suited to large finite-element systems. A tolerance factor of 0.1 is used in the linear solver settings, and the system is manually scaled using prescribed factors for the primary variables $\mathbf{A}$ and $\mathbf{T}$, chosen according to the underlying physics so that in the rescaled problem the two variables have a comparable order of magnitude [17]. This scaling improves the conditioning of the system and makes the convergence behavior more robust.
Nonlinearity is treated with a fully coupled Newton method in which all equations and unknowns are solved simultaneously. A constant Newton scheme is employed, using a fixed damping factor to moderate the step size in each iteration, reducing the risk of divergence in strongly nonlinear regimes. The Jacobian is updated minimally; it is not recomputed at every iteration unless necessary, which reduces the computational cost while retaining a sufficient accuracy. The termination criteria of the nonlinear iterations is based on both the solution and the residual, ensuring that the final solution at each time step is accepted only when the increment in the unknowns and the norm of the

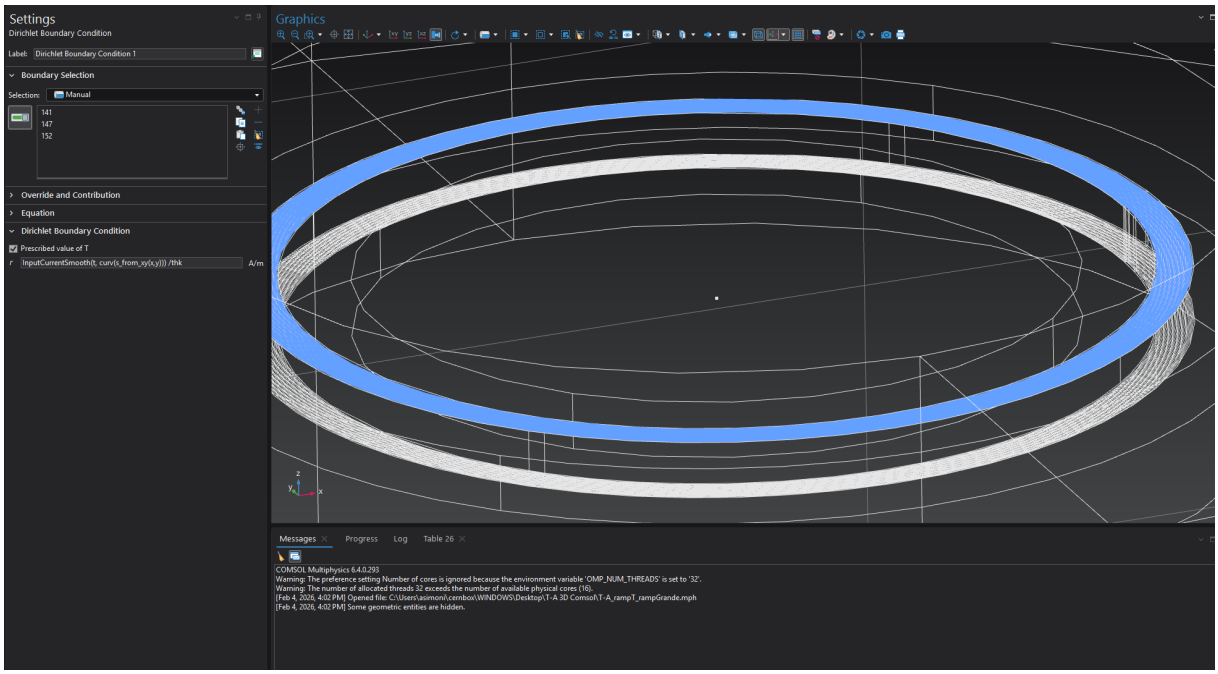


Figure 3.11: Imposition of the Dirichlet condition on T on the upper boundary

residual are simultaneously below the prescribed tolerances.

4 | Experimental Activities and Characterization

4.1. Introduction

This chapter describes the experimental activities conducted at CERN for the fabrication and testing of non-insulated (NI) fully soldered REBCO pancake coils as part of the 40 T Final Cooling Solenoid (FCS) program for the Muon Collider project.
All the presented efforts and results aim at the realization of a 15 T sub-scale prototype, constituted by a stack of 24 coils, to be presented before September 2026. The major experimental objectives presented in this thesis were achieving a consistent high quality and reproducible coil production process, successfully characterization the electromagnetic behavior of single and multiple stacked pancakes and generating benchmarking data for numerical models.

Over seven months, more than twenty pancake coils were fabricated, in order to optimize the production process for high quality coils that can be used for a 15 T solenoid, and tested at 77 K to establish whether the production damaged the superconducting properties of the tape with a first stage of electromagnetic characterization.
This chapter presents the fabrication methodology, testing procedures, measurement instrumentation, and results. The current final state of the PEEC COMSOL model is designed to directly reproduce insulated HTS coils, as in first approximation can be considered to be the polished one presented in **??**.

4.2. Coil Design and Fabrication Process

All the fabricated coils were targeting a geometry being a scaled down version of the final pancakes for the 40 T solenoid. In that case, 12 mm wide REBCO tape is used, and an inner and outer diameter of 60 and 180 mm, respectively, are foreseen. Instead, the current design employs 4 mm wide tape wound to produce coils with 60 mm and 100 mm inner and outer diameters, respectively . This width consequently represents the height of

the coils currently being fabricated, with an inner bore just big enough to fit the cooling channels and the beam pipe. This size reduction choice was made for multiple reasons. The first one is limiting the usage of tape, acquired commercially around 50-60 €/m (before the significant price drop due to the huge demand from the fusion community [67]). The second is the maximum diameter size constraint imposed by the available 4.2 K testing facilities at CERN, being around 110 mm. In this way, the characterization at operational temperature of the coils did not require additional efforts also in this direction. The winding machine currently in use is also presented to show the different stages characterizing the production process.

4.2.1. Baseline Geometry

All coils follow a standardized design with inner diameter 60 mm, outer diameter 100 mm and height of 4 mm with the use of ReBCO tape coming from three different suppliers: Faraday Factory Japan LLC (FFJ), Shanghai Superconductor Technology (SST) (China) and Fujikura Ltd. (Japan).
All tapes use standard REBCO-coated conductor architecture with Hastelloy substrate, buffer layers, REBCO superconductor, silver protective layer, and copper stabilizers (see fig. 1.7 for the structure and 4.1). Target turn count is approximately 300, with actual values ranging from 260 to 365 depending on the thickness of the tape. The coils are single-

Manufacturer	Fujikura	SST	FFJ (low grade)	FFJ (high grade)
Pristine length (m)	765	271	206	404
Width (mm)	3.99 ± 1	4.01 ± 1	4 ± 1	4 ± 1
Thickness (μm)	86.5 ± 0.5	69 ± 0.5	55 ± 0.5	70 ± 0.5
Substrate (μm)	50 ± 1	45 ± 1	40 ± 1	38 ± 1
REBCO (μm)	2.5 ± 0.5	1.5 ± 0.5	2 ± 0.5	–
Ag (μm)	2 ± 0.5	10 ± 2	5 ± 1	10 ± 2
Cu (μm/side)	10 ± 1	242 ± 1	111 ± 1	180 ± 1
av I_c 77 K, s.f. (A)	207 ± 2	242 ± 3	111 ± 2	180 ± 1

Table 4.1: Examples of REBCO tapes used for coil fabrication.

layer pancakes with the HTS layer facing inward. This choice places the superconductor in the condition of being pushed against the substrate (instead of being pulled from it) during operation, improving the resistance to delamination, i.e. the detachment of the superconducting layer from the substrate. The non-insulated soldered architecture allows for radial current redistribution, improving electrical and thermal stability during a quench phenomena, and improves the mechanical robustness.

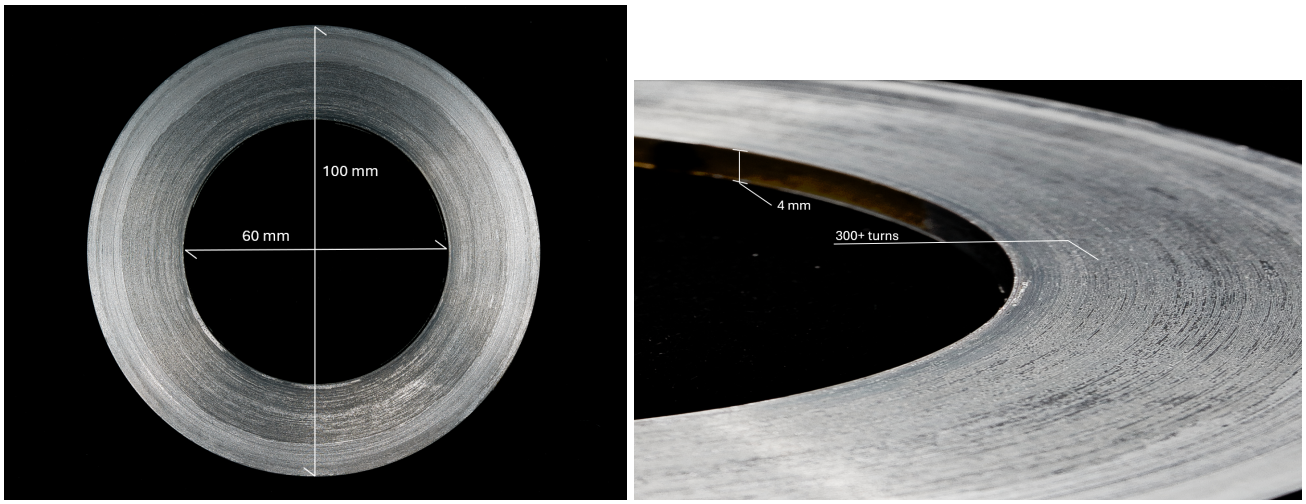


Figure 4.1: Visualization of the coil characteristic dimensions.

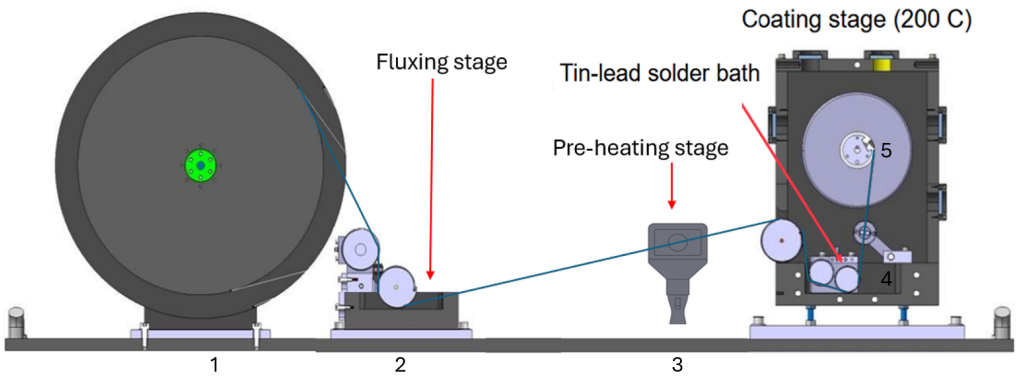


Figure 4.2: Winding setup simplified sketch.

4.2.2. Winding Apparatus

The winding system consists of a sequence of five stages along a 1.5m setup:

1. a big wheel on which the tape is respooled from the producer's batch;
2. the fluxing system at room temperature using diluted rosin flux or WF305F;
3. a pre-heating stage in which the flux gets activated;
4. the immersion in a 200°C eutectic molten Sn-Pb solder bath;
5. the winding onto a cylindrical mandrel with restraining wheels maintaining pancake geometry.

One of the biggest challenges is the reproducibility of the process, as the parameter space of this fabrication process includes flux used, winding speed, winding tension etc.. (see

?? as an example with four coils).

Coils	HW018	HW024	MHW050	MHW061
Tape	SST	FF Low Grade	FF High Grade	FF High Grade
Total length on coil (m)	79	89	72.7	72.58
Thickness nominal (μm)	69± 0.5	55.369± 0.5	6769± 0.5	6869± 0.5
N.o. turns	303	355	287	288
Outer diameter (mm)	98.77± 0.01	101.50± 0.01	101.41± 0.01	100.61± 0.01
Inner diameter (mm)	60.48± 0.01	60.18± 0.01	60.22± 0.01	60.24± 0.01
Thickness on coil (μm)	66± 1	56± 1	72± 1	70± 1
Motor winding	no	no	yes	yes
Motor speed (rpm)	-	-	10	10
Argon (l/m)	n.a.	n.a.	8	8
Tension (kg)	2 ± 0.1	2 ± 0.1	1.5± 0.1	1.2± 0.1
Solder temperature (°C)	200	200	200	200
Flux type	Rosin	Rosin	WF305F	WF305F

Table 4.2: Main winding parameters for 4 fabricated example coils.

The process must achieve thin, ideally void and contamination free, a uniform solder layers between turns, providing low electrical resistance while maintaining a good mechanical integrity. The winding tension was kept constant at 2 kg for all coils, affecting the turn-to-turn solder thickness as higher tensions reduce it, limiting the solder consumption but causing buckling phenomena on the lateral surface of the coil. One of the biggest challenges is the achievement of the desired outer diameter, as it depends on the contributions of both the tape and the solder. In fact, the specifications provided by the manufacturer are often imprecise by 2-5 μm, and this, together with the dependency of the solder layer thickness from the winding tension makes it challenging to obtain a result very close to the 100 mm outer diameter goal.

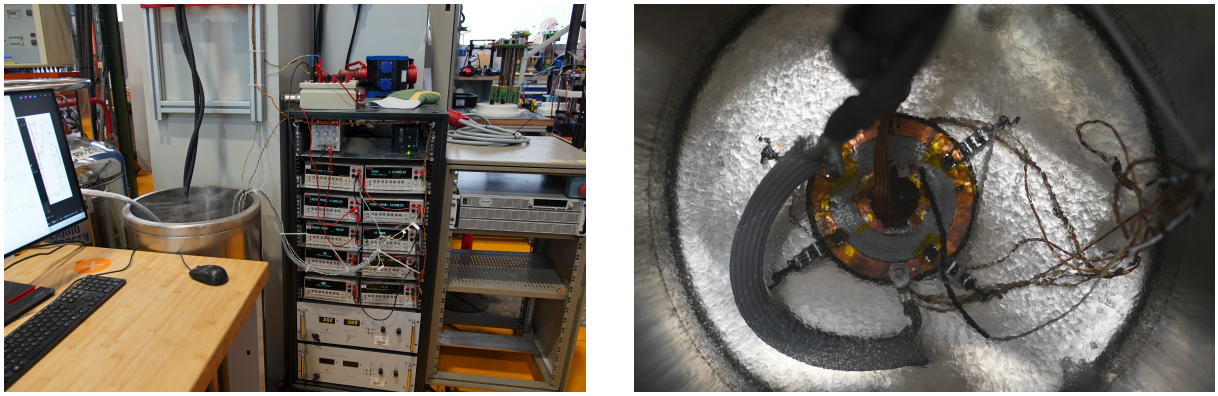
4.3. Experimental Test Setup

Together with a well-designed, reproducible, and efficient fabrication stage, the biggest priority is the thorough cryogenic characterization of the pancake coils.
Measurements were done in liquid Nitrogen, thanks to a setup that was assembled, programmed, and put into operation in just four weeks of teamwork.

4.3.1. Cryogenic Facility

Coils are tested immersed in boiling liquid nitrogen (LN_2) at atmospheric pressure. This approach was selected for practical reasons for the first testing phase: in fact, LN_2 is readily available and not expensive; the setup needed for this scope is relatively simple and REBCO still maintains a substantial critical current density at 77 K for a first meaningful characterization. In addition, the mechanical stresses due to thermal contraction are already comparable to those at 4.2K.

The facility consists of a cylindrical dewar with sufficient volume to fully submerge the sample; copper current leads and contacts, to inject and extract the current in the coil; and a rack with two Delta Elektronika SM 30-200 DC power supplies and ten Keithley 2001 Digital Multi Meters having a resolution of $O(10^{-6})$ V.



(a) (b)

Figure 4.3: Complete setup with multimeters, LN_2 dewar and cryostat (a) and the instrumented coil submerged in LN_2 (b).

Current injection into the sample must be uniform and low-resistance to obtain valid measurements; full-face copper contacts were used and pressed on the inside and outside of the coil, utilizing a 75 μm Indium sheet as a soft, low resistive interlayer. A poor contact might cause inhomogeneous current injection and localized heating that might result in premature quenching phenomena.
Voltage taps and Hall probes are the two essential measurement instruments for characterizing high-temperature superconducting (HTS) magnets. Voltage taps are used to measure a potential difference and provide stable readings across wide temperature and field ranges.
Hall probes measure local magnetic field strength by exploiting the Hall effect. When a planar current-carrying conductor is immersed in a magnetic field, the electrons experi-

ence a Lorentz force due to the component of the field normal to the surface, that deflects them to one side of the conductor. This generates an electric field and an associated voltage, called the Hall voltage. If the conductor is placed perpendicularly to the magnetic field, the Hall voltage is directly proportional to the applied field.
The so called 'active area' of Hall probes is made of a thin semiconductor experiencing an externally supplied current flow. By measuring the Hall voltage, one can infer the local magnetic field with a spatial resolution on the millimeter scale. However, Hall probes exhibit several measurement challenges that necessitate careful treatment. For instance, the temperature dependence arises as the charge carrier concentration changes with temperature. Due to this and other potential issues, Hall probes must be calibrated against known reference magnetic fields before any experimental campaign.

In the particular case of the coil testing campaign, the instrumentation was integrated into a plate positioned under the coil in fig. 4.4. It was constituted by seven radially aligned voltage taps with 3 mm spacing, allowing the measurement of the different behaviour of each circular sector; and two Hall probes at various bore and surface locations.



Figure 4.4: Real instrumented coil.

4.4. Experiments and Measurements

From a macroscopic point of view, the non-insulated superconducting coil can be very well approximated by the simple circuit of fig. 4.5 having a resistance R in parallel with an inductance L, which represents the radial and azimuthal electrical effects, respectively.

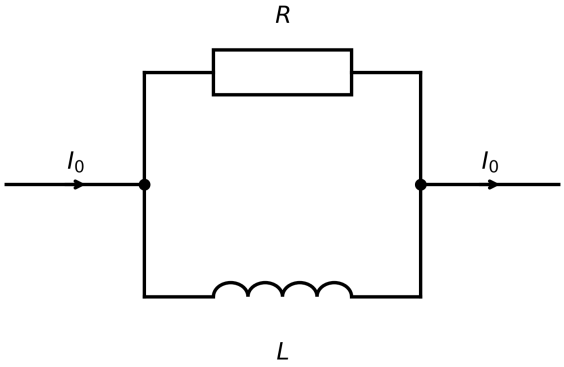


Figure 4.5: Simplified equivalent circuit of an NI superconducting coil.

The experimental campaign aims to determine these two main parameters, together with the charging time constant $\tau = L/R$.
To do so, two different sets of experiments were performed: current ramps at fixed rates (0.5 A/min) and current steps (5–20 A) in the range (0–150 A). The circuit can be fully described by the two Kirchhoff equations:

$$\begin{cases} I_0(t) = I_L(t) + I_R(t), \\ L\,\dfrac{dI_L(t)}{dt} - R\,I_R(t) = 0. \end{cases} \tag{4.1}$$

with $I_L(t) + I_R(t)$ being the currents flowing through the inductor and the resistance, respectively.
In the case of a current step, at t=0 s, from 0 to I_0 A, the associated solution is:

$$I_L(t) = I_0(1 - e^{-\frac{t}{\tau}}). \tag{4.2}$$

Two deductions can be drawn from it. First of all, at time t=0 s the current is entirely flowing through the resistive element as $I_L = 0$. Second of all, the overall voltage between injection and extraction behaves as:

$$V(t) = L\,\frac{dI_L(t)}{dt} = L\,\frac{I_0}{\tau}e^{-\frac{t}{\tau}} = R\,I_0 e^{-\frac{t}{\tau}}. \tag{4.3}$$

This implies that from the voltage measured as the current step is applied, R can be deduced as $\mathrm{R} = \dfrac{V|_{t=0}}{I_0}$.
On the other hand, in the case of a linear current ramp $I_0(t) = I\,\dfrac{t}{T}$, where I and T are

the maximum current reached by the ramp and the total ramp-up time, respectively, the current flowing through the inductance is:

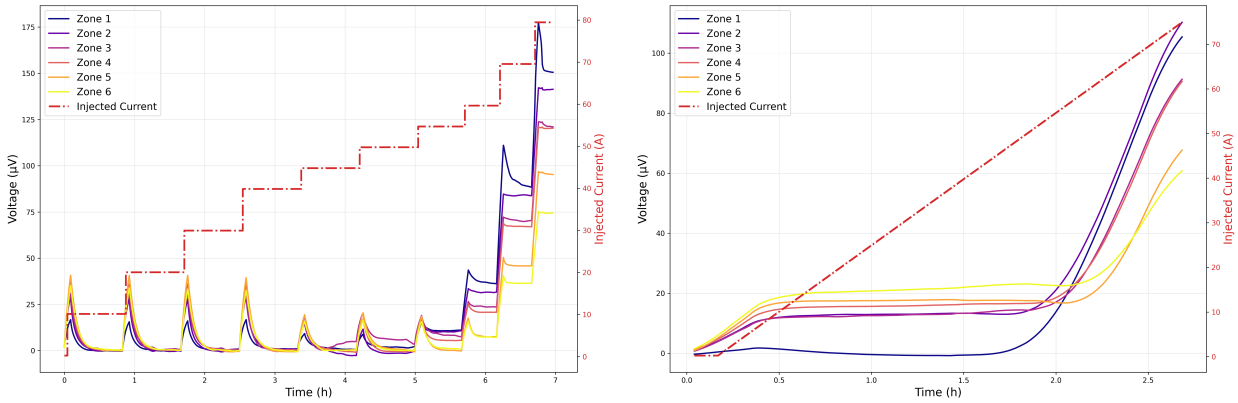
$$I_L(t) = \frac{I}{T}\left[t - \tau\left(1 - e^{-t/\tau}\right)\right], \tag{4.4}$$

following the source I_0 with a time delay τ.
This time, the voltage drop is:

$$V(t) = L\frac{I}{T}\left(1 - e^{-t/\tau}\right). \tag{4.5}$$

In this second case, it is possible to observe that when $t \gg \tau$ the voltage saturates to the value $V_{\text{sat}} = L\dfrac{I}{T}$, and the inductance value could be obtained as all the other quantities are known. In reality, the measured voltage contains an additional resistive contribution due to transfer length effects and imperfect insulation from the copper contacts, grouped in the term V_{res}.
In fig. 4.7, the full cycle ramp up and ramp down can be seen, and the saturation just described can be observed in the plateaus at the beginning and at the end of the experiment.
During the first plateau, the measured voltage is $V_1 = V_{\text{sat}} + V_{\text{res}}$, while during the second, as the current gets ramped down, $V_2 = -V_{\text{sat}} + V_{res}$. Hence, the required voltage for the computation of L can be obtained as $V_{\text{sat}} = \dfrac{V_1 + V_2}{2}$. At this point, since both L and R are known, the time constant τ can be computed.The measured data provided a value of radial resistance R in the range 20-35 $\mu\Omega$, an inductance L $\simeq$ 8 mH, and a time constant of 250–350 s. The realization of multiple measurements at different currents was also useful to assess whether the time constant varies with current and the distance from I_c. In the present experiments, it was reasonably independent of it.
It is particularly interesting to observe the behaviour of different sectors of the coil. This can be done thanks to the seven voltage taps positioned radially, splitting the coil into 6 concentric circular sectors, and analyzing each one of them individually, as in fig. 4.6, where an example of such an analysis is reported for both kind of experiments.

The presented equivalent circuit and voltage evolution over time, however, is physically meaningful only if $I_0 < I_{\text{c}}$ everywhere in the coil, i.e., locally the current density $\mathbf{J} < J_{\text{c}}$, with J_{c} critical current density. As this condition starts to fail, the coil progressively enters the critical state, i.e., the superconductor is not able to carry a higher current density, and energy dissipation (hence, a resistance and a voltage), starts to appear. Since J_{c} decreases as the magnetic flux density increases, the inner turns are going to experience the transition first, as in those regions the magnetic field is higher. Moreover, the gener-



(a) (b)

Figure 4.6: Measurement of voltage over half of a stepping (a) and ramping (b) experiments in the six different sectors of the coil.

ated Joule losses, locally increase the temperature, further reducing J_c. Consequently, as the current is ramped above I_c, a linear voltage progressively starts to appear from the inner turns outwards, as in fig. 4.7. The critical current of a coil does not have a uniform definition, contrarily to single samples of tape, for which the standard choice is $1\mu V/cm$ [65]. For our experiments, the same definition was used, quantified based on the length of the very first few inner turns, as they experience the critical state first, giving a reference voltage of (100–120 μV).

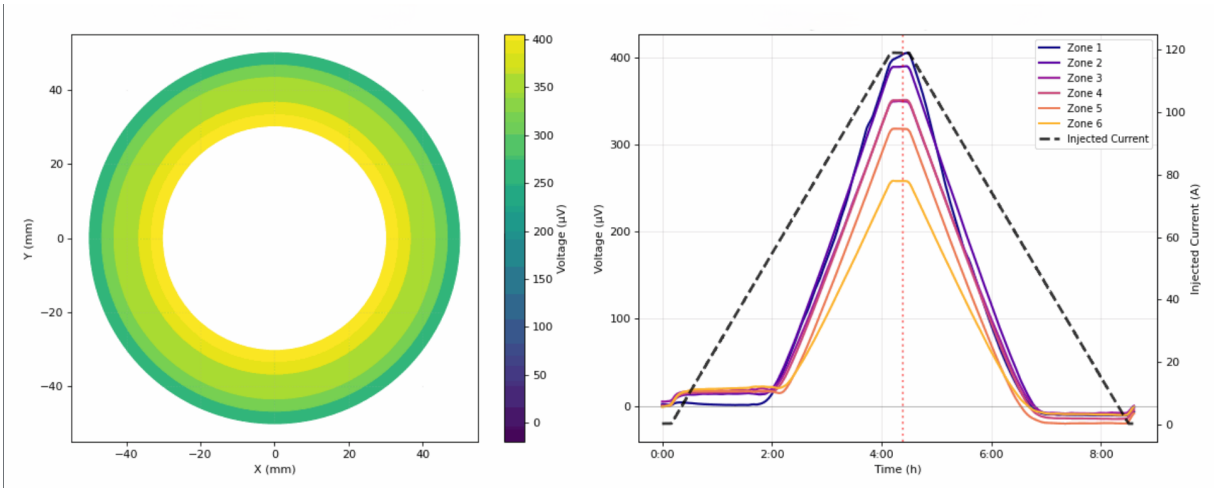


Figure 4.7: Behavior of the voltage across the coil during a current ramp exceeding I_c

Therefore, the critical current can be determined by looking at the complete V-I characteristic curve of the coil, as the current value for which the established voltage threshold is exceeded.

As shown in 4.8 the transition between the two regions can be more or less sharp, providing information about the quality of the fabricated coil. A sharp transition is sign of good quality, while a broader one indicates a critical current variation across turns, potentially caused by tape inhomogeneity, winding damage, or strain gradients.

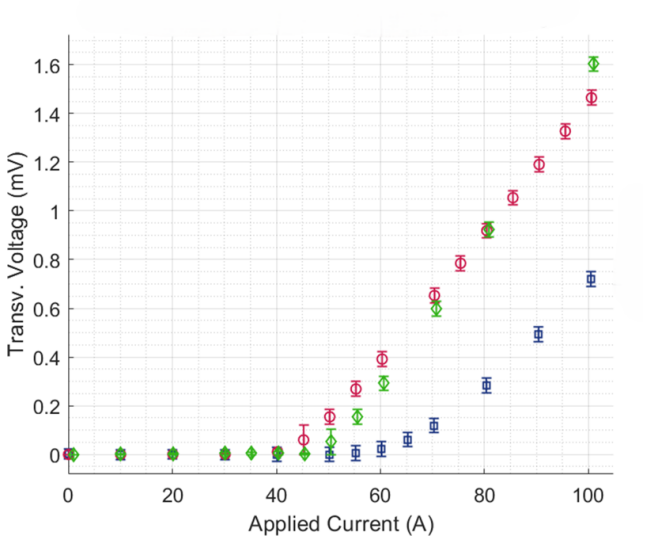


Figure 4.8: V-I curves of three different coils that were measured

The magnetic flux density measurement is represented in a 2D plot with a B-I curve as fig. 4.9. A linear regime can be observed below I_c, with approximately 5 mT generated for every injected Ampère, followed by a saturation for higher values of applied current, before decreasing as resistive dissipation reduces the critical current density.

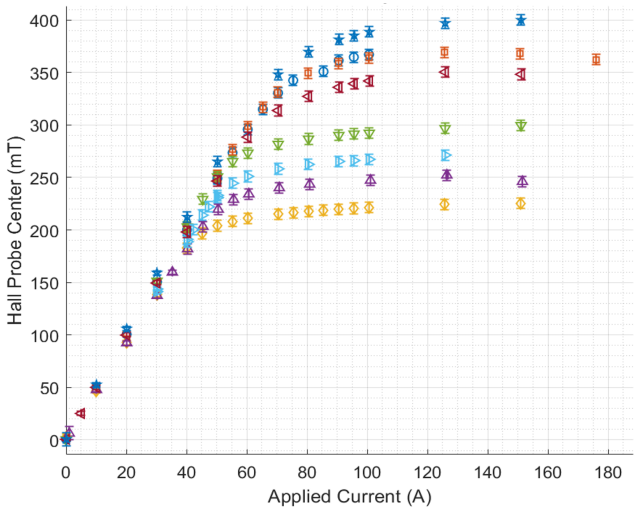
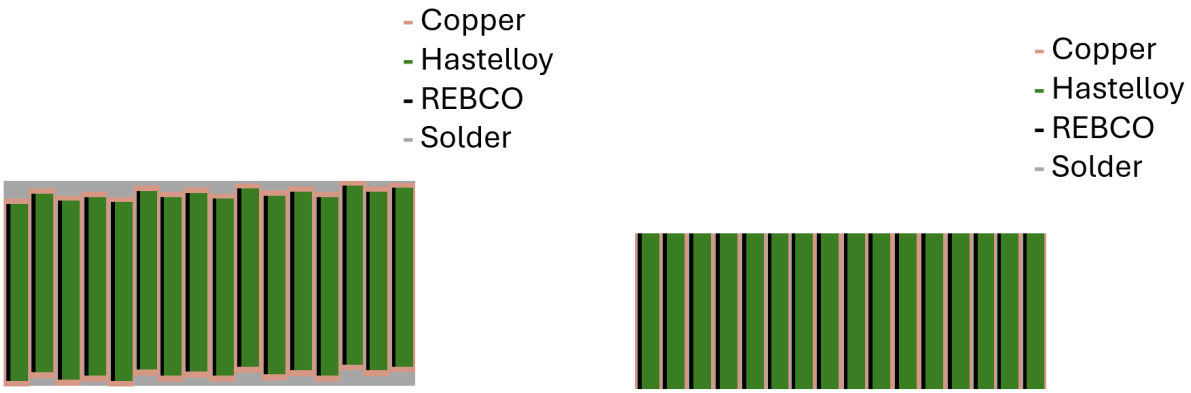


Figure 4.9: B-I curves of eight different coils

In solenoids, the peak field is reached on coil, and the discrepancy between the center field and its peak value decreases as the number of turns grows. For a small coil of 24 turns, the ratio between the two values would be around 5, while for full size coils of 250-300 turns, such a ratio was approximately 2. This ratio has an important implication for the operating margin: if the target center field is 1 T, the conductor must be able to operate in 2 T local field.

Polishing Experiment

Coil HW009 was mechanically polished on both flat faces to remove the solder and copper stabilizer. On a conceptual level, half of a cross section of the coil can be imagined as in fig. 4.10. Before polishing it is a sequence of non perfectly aligned tapes, kept together by the solder, with the current being able to flow from one turn to the adjacent mostly through the solder and copper. This operation was performed to exploit the insulating properties of the buffer layers, that do not allow any flow of current between the superconducting layer and the Hastelloy substrate. Therefore, the polishing operation removes these favorite paths and the current prefers the azimuthal path immediately sinking into the superconductor, and quickly reaching the steady state regime.



(a) (b)

Figure 4.10: Left: Schematic representation of half of the cross section before (a) and after (b) polishing.

Such a coil was then retested to measure how this modification affected its electromagnetic behavior, particularly the charging time. The data showed a dramatic time constant reduction, from about 320 s to just 2 s while the linear B–I dependence below I_c remained unchanged. Therefore, it is reasonable to assume that the damage to the superconducting layer due to the mechanical treatment was negligible. However, the coil now behaves

effectively as insulated, and a quench phenomena was observed after reaching the critical current. This confirms that non-insulated coil self-protection relies on the current bypassing from one turn to the adjacent, allowing for a stable operation even well above I_c.

4.5. Limitations

Two main limitations of the experimental campaign should be acknowledged: **Temperature and field:** All tests were performed at 77 K in self-field, whereas the target application (40 T FCS) will operate at 4.2 K in high field. The overall behaviour differ significantly due to a much higher critical current density and, consequently, very big Lorentz forces acting on the coils.
Testing at 4.2 K in background fields up to 20 T is essential for the validation of this technology; therefore, a test of this kind is foreseen in the next months. **Duration:** The test duration was limited to a few hours per coil, insufficient to assess long-term stability or degradation. In fact, thermal cycling and mechanical fatigue could alter the performance over a long period of time.

5 | Numerical Results

5.1. Introduction

This chapter presents results obtained from the two numerical models that were implemented, based on the mathematical formulations presented in chapter 2. The simulations include both frequency-domain results in MATLAB, benchmarked against Octave or COMSOL Multiphysics solutions, and time-domain results in which the PEEC and T-A models were compared directly. Two geometries were studied: a rectangular conducting square and a spiral shaped conductor. The results are organized by geometry and analysis type, focusing on model cross-verification, observed discrepancies, and computational efficiency.

The main quantities considered for the comparison are the total Joule losses and the magnetic flux density. This choice was made as power losses and magnetic flux density are single quantities representing the global behavior of the system.

In addition to the absolute comparison between computed values, the relative error and relative discrepancy between the models were computed to establish the distance between the two results.

In particular, when a reference solution u_{ref} was available, the relative error with respect to the computed solution u was computed. On the other hand, when the computational effort did not allow an extensive refinement study, the two solutions u_1, u_2, obtained using the same discretization of the conductor, were compared directly.

In full generality, these quantities are defined using the infinity norm $\|\cdot\|_\infty$, where for a vector $v \in \mathbb{R}^n$ one has $\|v\|_\infty = \max_{1\leq i\leq n} |v_i|$, as

$$e_{\text{rel}} = \frac{\|u_{\text{ref}} - u\|_\infty}{\|u_{\text{ref}}\|_\infty}, \; d_{\text{rel}} = \frac{\|u_1 - u_2\|_\infty}{\|u_2\|_\infty}. \tag{5.1}$$

However, all quantities of interest reduce to a single scalar value at each time step, since vector quantities were compared through their norms in a specific point, the infinity norm reduces to the standard absolute value, and relative error discrepancy simplify respectively

to

$$e_{\text{rel}} = \frac{|u_{\text{ref}} - u|}{|u_{\text{ref}}|}. \tag{5.2}$$

In scenarios where no reference solution was available and two solutions u_1, u_2 obtained with the same conductor discretization were compared directly through

$$d_{\text{rel}} = \frac{|u_1 - u_2|}{|u_2|}, \tag{5.3}$$

where one of the two solutions is arbitrarily taken as reference.

5.1.1. Test Geometries and Parameters

For each of the two conducting domains that were considered, a set of geometric and physical parameters was fixed. A squared shape was chosen for a first test. The main reasons for this were two: its simplicity, and the pre-existence of a PEEC Octave model, developed in the Mathematics department of Politecnico di Milano [30], in which the electromagnetic problem is solved on this same domain.
The main parameters for this first case are listed in table 5.1

Quantity	**Parameter**	**Value**
Length x	L_x	$0.1\,\text{m}$
Length y	L_y	$0.1\,\text{m}$
Thickness	δ	$3 \times 10^{-3}\,\text{m}$
Electrical conductivity	σ	$4.6729 \times 10^{6}\,\text{S/m}$ or $1 \times 10^{10}\,\text{S/m}$
Magnetic permeability	μ	$\mu_0 = 4\pi \times 10^{-7}\,\text{H/m}$

Table 5.1: Simulation parameters for square geometry, see fig. 5.1.

This intermediate step allows for a first validation of the PEEC method, before moving on to the final goal geometry. It provides a test case for assessing mesh convergence properties and frequency dependence behavior in the excitation scenarios of an applied external magnetic field and a total current being imposed. For the latter case, a corresponding COMSOL A-V 3D model was implemented.
The discretization of the conductor is carried out using a uniform mesh having the same number of elements along the two directions.

The spiral domain is the representation of the real shape of a pancake coil. It is described

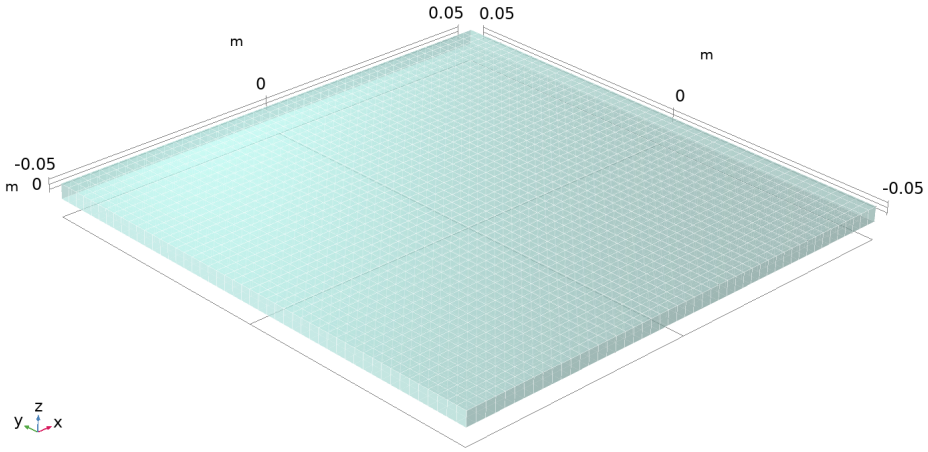


Figure 5.1: Meshed square geometry in COMSOL.

by the equation:

$$\begin{cases} x(u) = \left(r_0 - \dfrac{\text{thk}}{2\pi}\, u\right) \cos u, \\ y(u) = \left(r_0 - \dfrac{\text{thk}}{2\pi}\, u\right) \sin u, \end{cases} \qquad u \in [0, 2\pi N]. \tag{5.4}$$

with N number of turns. The set of parameters associated with this second geometry is reported in table 5.2.

Parameter	**Symbol**	**Value**
Outer radius	r_0	$3 \times 10^{-2}\,\text{m}$
Height	H	$4 \times 10^{-3}\,\text{m}$
Conductor thickness	δ	$8 \times 10^{-5}\,\text{m}$
Number of turns	N	$9, 24$
Electrical conductivity	σ	$1 \times 10^{10}\,\text{S/m}$
Magnetic permeability	μ_0	$4\pi \times 10^{-7}\,\text{H/m}$

Table 5.2: Set of parameters for the spiral geometry.

5.2. Frequency-Domain Results

This first series of results, obtained with the PEEC MATLAB model exploiting the frequency domain formulation 3.14, aimed first at validating the implementation of the original formulation, on the square geometry, in which an external magnetic field can be applied through the term $\mathbf{A}_0$, and then testing the new external current imposition technique.

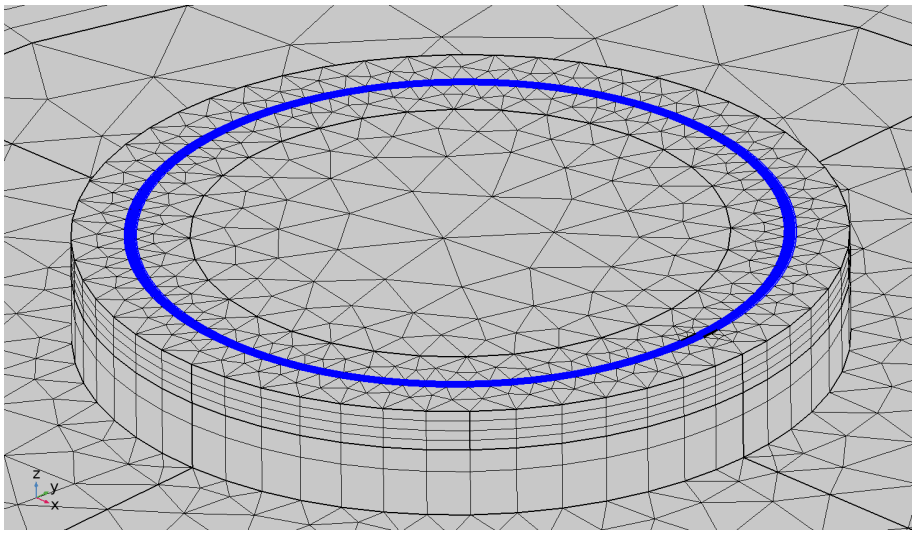


Figure 5.2: Mesh of a 9-turn spiral and the surrounding air in COMSOL.

5.2.1. Uniform External Magnetic Field

In the first test, a uniform external magnetic field was applied:

$$\mathbf{B}_0 = [0,\, 0,\, B_0], \quad \text{with } B_0 = 10^{-3}\ \mathbf{T}. \tag{5.5}$$

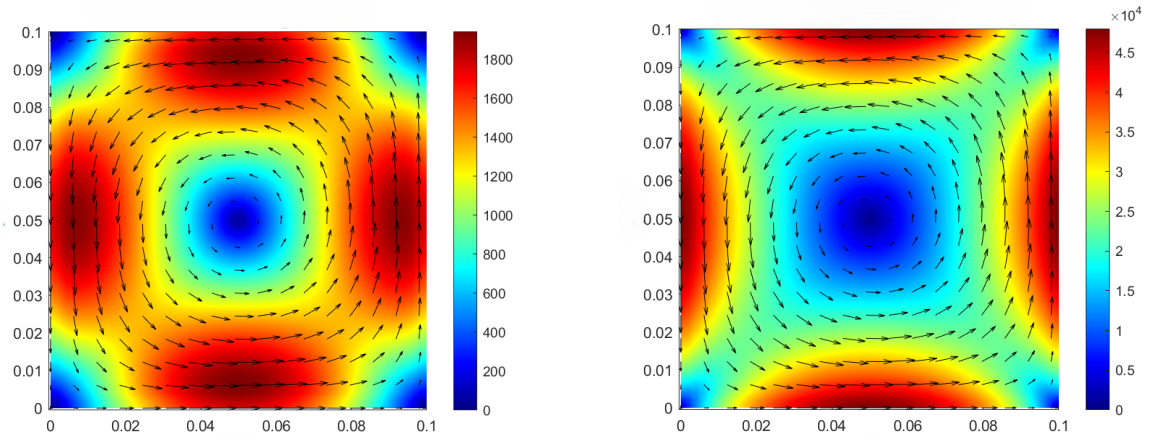
Such a magnetic flux density is associated with magnetic vector potential

$$\mathbf{A}_0 = \frac{B_0}{2}[-y,\, x,\, 0].$$

Note that the choice of $\mathbf{A}_0$ is again not unique (see section 2.3.1), in this case it was chosen such that $\nabla \cdot \mathbf{A}_0 = 0$.
The resulting current density obtained with the PEEC MATLAB model is complex-valued due to the excitation in the frequency domain; the spatial distribution of both real and imaginary components are displayed in fig. 5.3. Joule losses were computed, from the current vector potential distribution, as:

$$P_{\text{Joule}} = \frac{1}{2}\int_{\Omega} \frac{|\mathbf{J}|^2}{\sigma}\,\mathrm{d}\Omega = \frac{1}{2}\int_{\Omega} \frac{|\nabla \times \mathbf{T}|^2}{\sigma}\,\mathrm{d}\Omega. \tag{5.6}$$

The comparison was performed fixing the frequency at f = 50 Hz and refining the mesh. The frequency was fixed at f=50 Hz, the conductivity at $\sigma = 4.6729 \times 10^6\,\mathrm{S/m}$, and $\mathbf{B}_0$ is applied as in eq. (5.5).
An extensive overview of this test is given by table 5.3, and visually represented by fig. 5.4. For every fixed mesh refinement level, the agreement between the two PEEC implemen-



(a) (b)

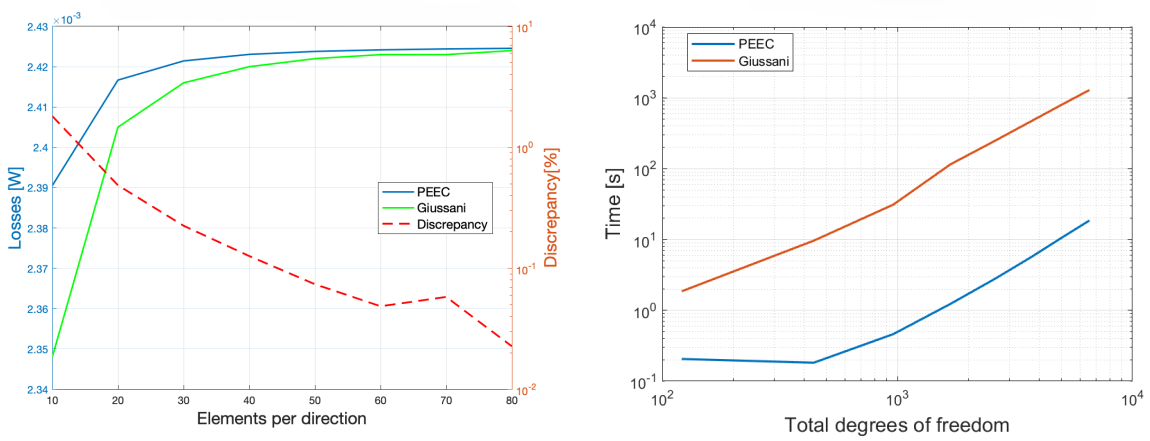
Figure 5.3: Real (a) and imaginary (b) part of the current density distribution.

tations is very good. The discrepancy between the two models has its maximum for the coarser mesh size, at less than 2%, and progressively decreases towards a null value. On the other hand, the distance from the MATLAB solution and the reference solution is also small, again above 1% only for the coarser mesh.

In terms of computation time and the speedup with respect to the pre-existing model, it has to be taken into account that the computation for this thesis were performed using a Processor Intel(R) Core(TM) i9-14900KS, 3200 Mhz, 24 Core(s), 32 Logical Processor(s) with 64 GB of RAM. Moreover, the Octave code exploit a parallelized approach, while in MATLAB the MEX compilation was used. However, the significant improvement did not involve the complexity of the algorithm, still quadratic with respect to the total number of degrees of freedom.

#dof	h	losses [W]	e_{rel}	time [s]	speedup
121	1/100	0.0023905	0.014311	0.851	**2.18x**
441	1/200	0.0024166	0.003356	0.211	**45.6x**
961	1/300	0.0024214	0.001367	0.418	**74.36x**
1681	1/400	0.0024231	0.000665	0.932	**123.45x**
2601	1/500	0.0024238	0.000376	2.122	**116.77x**
3721	1/600	0.0024242	0.000211	4.074	**115.63x**
5041	1/700	0.0024244	0.000128	7.484	**108.53x**
6561	1/800	0.0024245	0.000087	13.235	**97.66x**

Table 5.3: Mesh refinement study PEEC MATLAB vs reference PEEC Octave.



(a) (b)

Figure 5.4: Comparison of Joule losses and discrepancy between the two models(a) and computation time (b).

5.2.2. Imposed Current Density

In the second case, the conductivity was increased to $\sigma = 10^{10}\,\mathrm{S/m}$, and, in order to test the external current imposition method, a uniform current density corresponding to a current $I_0 = 30\,A$ was injected from the left and extracted from the right edges of the domain.

A showcase frequency $f = 5\,\mathrm{kHz}$ was chosen to demonstrate an example of current density distribution. The skin effect occurring along the height of the domain is clearly visible, with the current being concentrated near the upper and lower boundaries.

The skin effect arises because time-varying currents generate magnetic fields that induce opposing electric fields inside the conductor, inhibiting the field penetration into the bulk; consequently, the current density decays approximately exponentially away from the external surfaces rather than remaining uniformly distributed.

This decay is quantified by the skin depth δ_s, defined as the distance from the surface at which the current density magnitude drops to $1/e$ of its surface value. For a homogeneous conductor under a sinusoidal excitation, the skin depth is defined as:

$$\delta_s = \sqrt{\frac{2\rho}{\omega\mu}},$$

with ρ electrical resistivity, ω angular frequency, and μ magnetic permeability.

This time, the comparison was carried out against a COMSOL 3D A-V finite element model developed in parallel, which was also able to capture the non-uniform current

distribution along the thinner dimension.

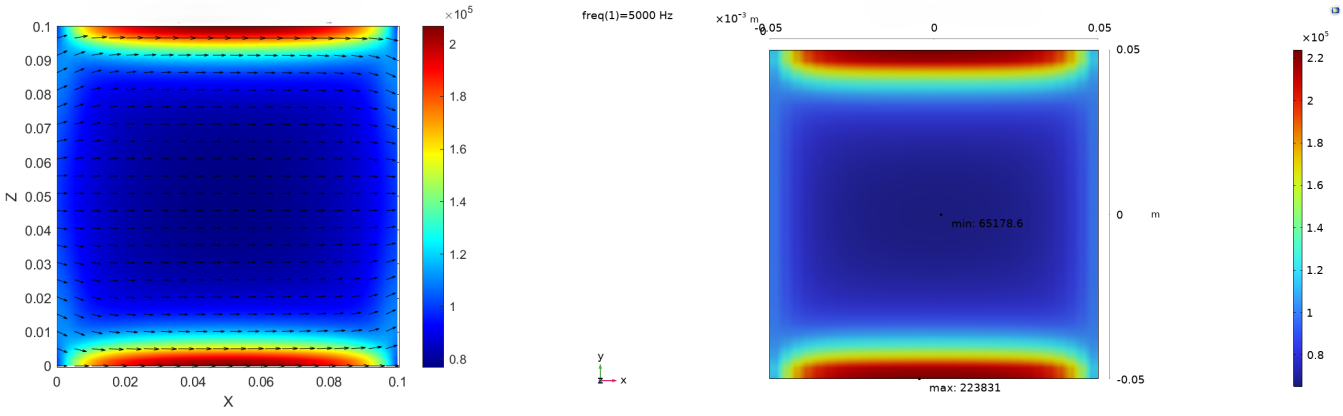
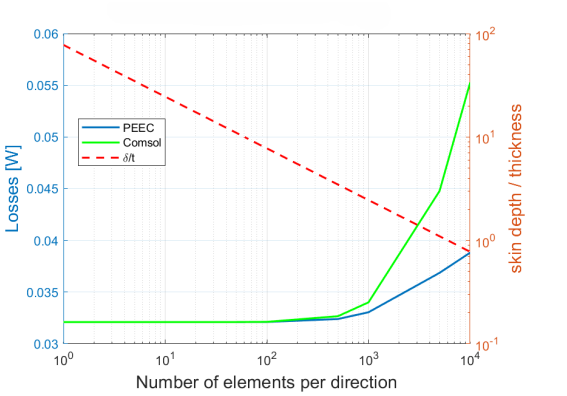
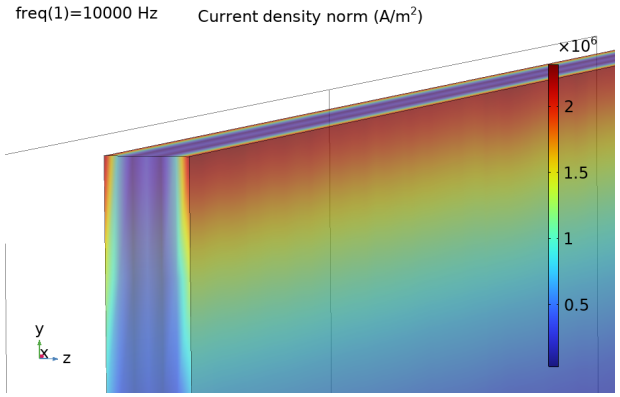


Figure 5.5: Comparison of the real part of the current density distribution at f=5 kHz.

Considering a fixed mesh resolution with the same number of elements along both directions $n_x = n_z = 50$, the Joule losses were computed over a frequency range from 1 Hz to 10 kHz. The PEEC-COMSOL discrepancy grew with frequency, reaching 50% at the f = 10 kHz.

This trend can be correlated with the skin depth ratio. In fact, when $\delta_s \approx \delta$, the current density is not distributed uniformly along the thickness of the geometry, hence, MATLAB and COMSOL results start to diverge.





(a)

Figure 5.6: Joule losses comparison from 1 to 10^4 Hz (a) and showcase of skin effect along δ at f=10^4Hz.

The computation time between PEEC and COMSOL was compared as a function of mesh

refinement. It is worth noticing that even though the PEEC method is coded in a high level programming language and has not been not fully optimized yet, the time required by the two methods to solve the problem for the same number of mesh elements in the conductor, is comparable.

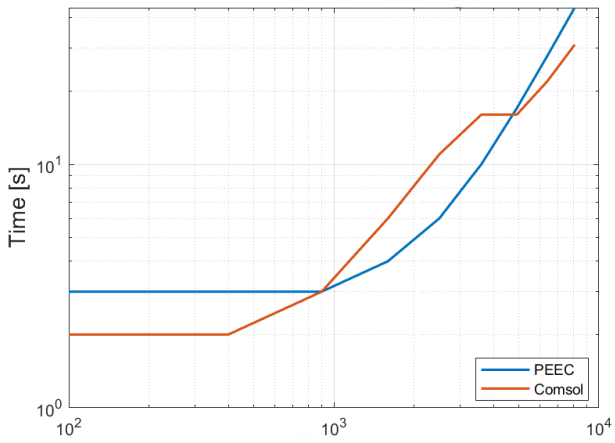


Figure 5.7: Computation time PEEC vs Comsol with respect to the number of mesh elements in the conductor for f = f_0.

5.3. Frequency vs Time-Domain Solution

In order to proceed step by step and validate the time-domain resolution scheme, frequency-domain results were compared with steady-state responses from time-domain simulations with periodic excitation. This constitutes a coherent intermediate step before moving on to the transient study of the new spiral geometry.

5.3.1. Comparison Overview

The frequency-domain problem, as shown in section 3.4.1, is:

$$\mathbf{R} + j\omega\mathbf{L}\mathbf{T}_f = \mathbf{S}_r + j\omega\mathbf{S}_\ell, \tag{5.7}$$

And the associated time-domain steady-state solution is $\mathbf{T}(t) = \Re\left(\mathbf{T}_f\, e^{j\omega t}\right)$. On the other hand, the time-domain evolution is governed by:

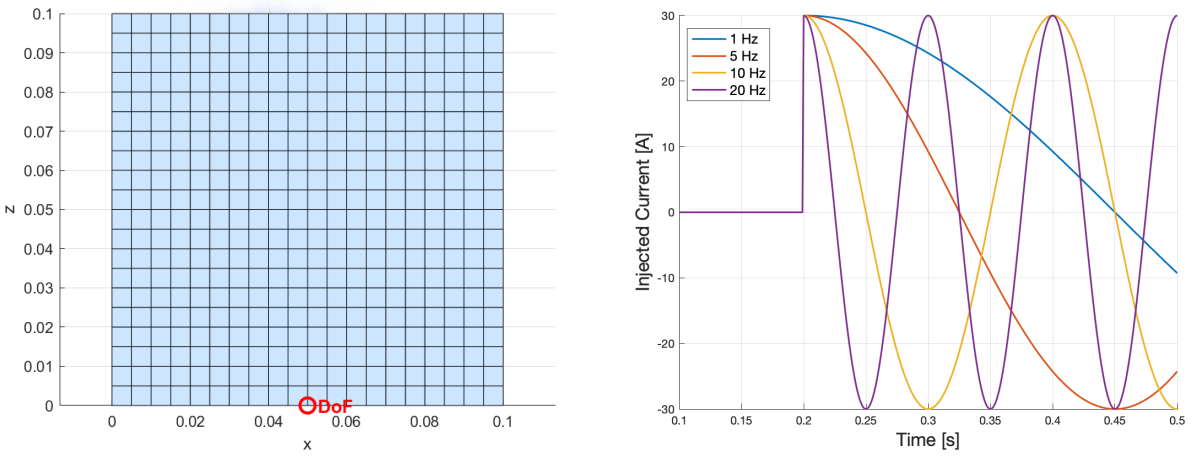
$$\mathbf{L}\frac{\mathrm{d}\mathbf{T}(t)}{\mathrm{d}t} + \mathbf{R}\mathbf{T}(t) = \Re\left[\left(\mathbf{S}_r + j\omega\mathbf{S}_\ell\right) e^{j\omega t}\right], \quad t \in [0, T_f], \tag{5.8}$$

with typical initial condition $\mathbf{T}(0) = \mathbf{0}$. The Backward Euler (BE) time discretization scheme was implemented, chosen for its absolute unconditional stability. Using a time step Δt, the discrete system at step n is:

$$(\Delta t\,\mathbf{R} + \mathbf{L})\,\mathbf{T}^n = \mathbf{L}\mathbf{T}^{n-1} + \Delta t\left(T^n_{N+1}\mathbf{S}_r + \dot{T}^n_{N+1}\mathbf{S}_l\right), \quad n = 1, \ldots, N_t. \tag{5.9}$$

with $T^n_{N+1} = T_{N+1}(t_n)$, $\dot{T}^n_{N+1} = \dfrac{\partial T_{N+1}}{\partial t}(t_n)$ and N_t being the total number of required time steps.

BE discretization scheme was applied to the rectangular strip for many test frequencies from 1 to 100 Hz (see some examples in fig. 5.8). The time-domain solution was integrated until steady state was reached. The periodic oscillations were compared with the frequency-domain solution rescaled in time by the term.

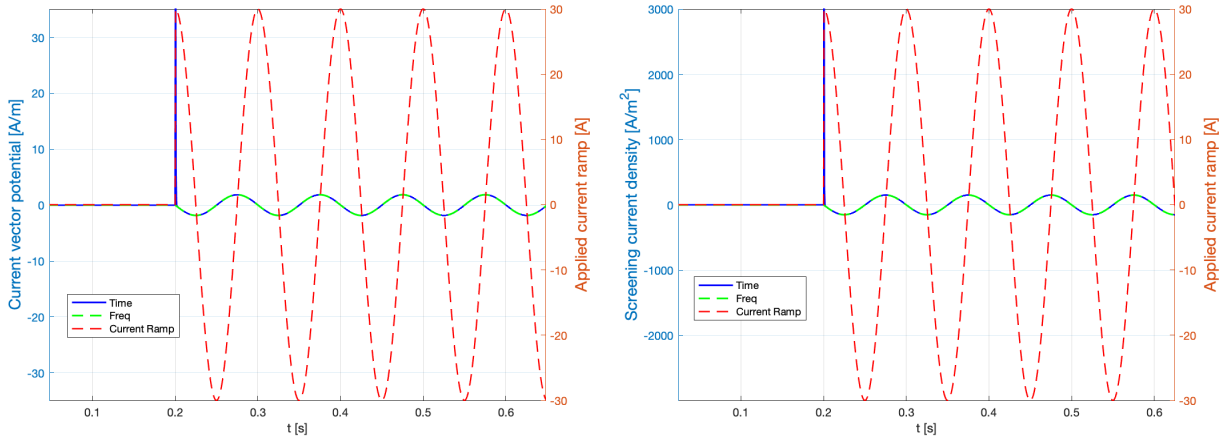


(a) (b)

Figure 5.8: Showcase degree of freedom for comparison (a) and examples of periodic current ramps (b).

A first qualitative comparison was carried out by looking at the local distribution of eddy currents, represented in the test degree of freedom (dof) shown in fig. 5.8, in terms of time evolution and amplitude and phase of its Fourier transform.

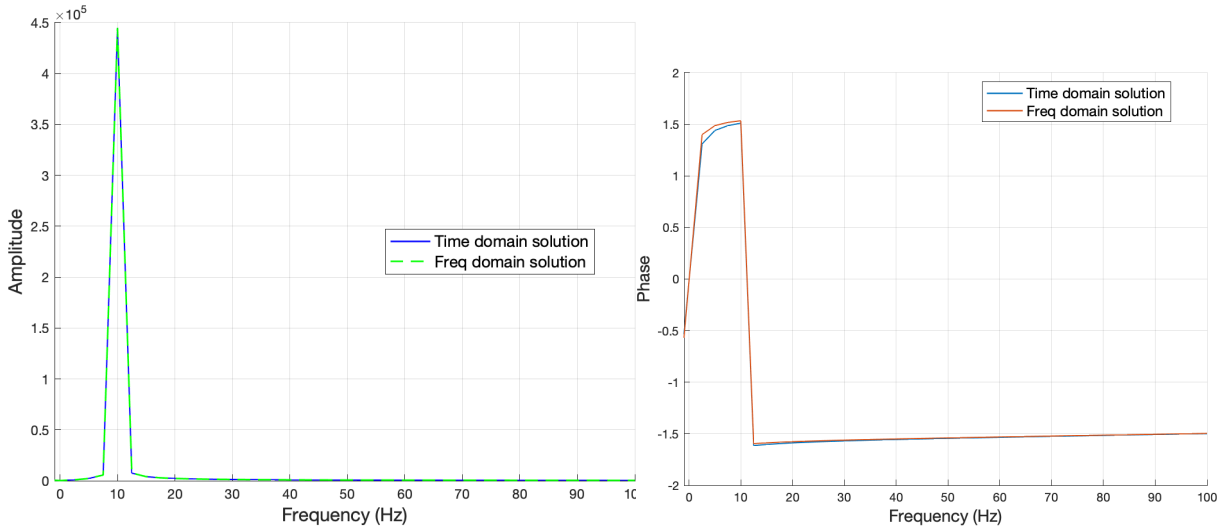
For all the analyzed frequencies between 0 and 10^3 Hz, the agreement is excellent in amplitude and phase for both the electric vector potential and current density values. As an example, the 10 Hz case is showcased in fig. 5.9 and fig. 5.10.



(a) (b)

Figure 5.9: Time evolution of electric vector potential (a) and eddy currents (b).

An initial spike can be observed, caused by the discontinuity in the current ramp applied to the system. However, it only involves a couple of time steps before the time solution reaches the steady state predicted by the frequency one.
After this qualitative comparison, the Fourier transform of both waves was performed, and it can be seen how the spectrum of the two distributions coincides in both amplitude and phase fig. 5.10. In the proposed example, a single amplitude peak at 10 Hz is obtained, precisely the excitation frequency that was applied.



(a) (b)

Figure 5.10: Fourier transform comparison of the electric vector potential in amplitude (a) and phase (b) for f = 10 Hz.

5.4. Time-Domain Results

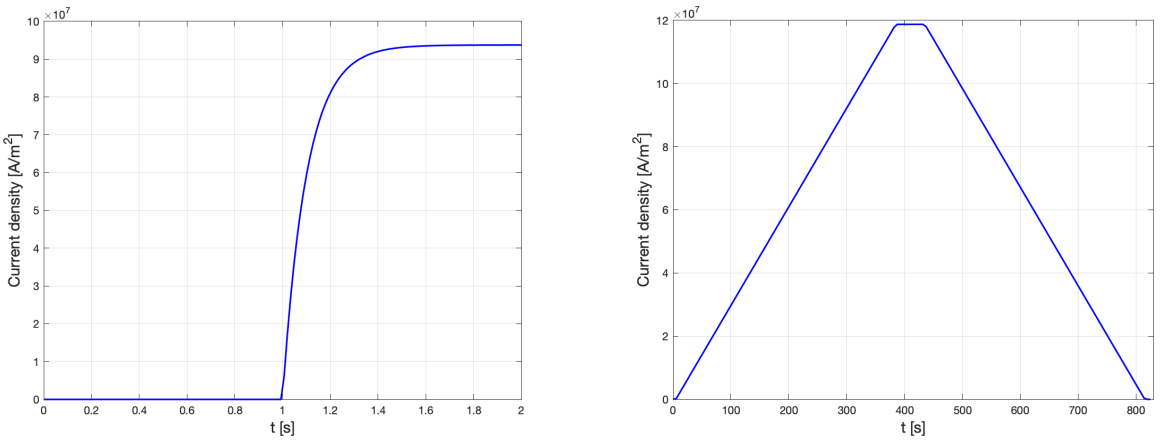
The time dependent results for a coil with linear relationship between electric field and current density are now presented. In particular, a constant conductivity $\sigma = 10^{10}\,\mathrm{S/m}$ has been used, for a spiral geometry with 9 and 24 turns.
Two different current ramps are used: the first exponential one represents a useful setting in which eddy currents can be locally compared between the two models. The smaller geometry with 9 turns was used for this analysis, together with the Joule losses computation.
The associated current density being injected can be described analytically with the following expression:

$$J_0(t) = \frac{I_0}{H\delta}\left(1 - e^{-k(t-t_{\mathrm{start}})}\right) H(t - t_{\mathrm{start}}), \tag{5.10}$$

where $I_0 = 30\,\mathrm{A}$, $t_{\mathrm{start}} = 1\,\mathrm{s}$, and $k = 10\,\mathrm{s}^{-1}$.
Its advantages are the very short computation time required, as its interesting portion only spans one second, together with having a sufficient rate of change to induce meaningful eddy currents that can be compared.
The second case represents a real experimental scenario of a slow linear ramp injected into the coil, as presented in fig. 4.7. This case was used for the 24 turn coil, focusing in particular on the values of Joule losses and magnetic flux density in the center and on coil.
The second excitation profile uses a trapezoidal current waveform to simulate a 77 K test of an insulated coil, having electromagnetic behavior similar to a mechanically polished NI HTS one (see section 4.4):

$$J_0(t) = \frac{1}{H\delta}\begin{cases} r\,(t - t_1) & \text{if } t_1 \le t < t_2 \\ I_0 & \text{if } t_2 \le t < t_3 \\ I_0 - r\,(t - t_3) & \text{if } t_3 \le t < t_4 \\ 0 & \text{otherwise} \end{cases}, \tag{5.11}$$

where t_1, t_2, t_3, and t_4 define the ramp-up start, plateau start, ramp-down start, and ramp-down end times, respectively, r is the employed current ramp rate in [A/s], and I_0 is the maximum current reached, and held during the plateau phase. This trapezoidal profile is suitable for a coil having a time constant of the order of few seconds, while it would definitely be too quick to observe the saturation voltage described in section 4.4.



(a) (b)

Figure 5.11: Injected current density, forcing terms described in eq. (5.10) (a) and eq. (5.11) (b).

5.4.1. 9-turn spiral

The first comparison is done between the computed values of current density, Joule losses and magnetic field for a 9 turn-coil, to which eq. (5.10) is applied.
First of all, a visual global comparison was done between the two current density distributions right after the ramp started and at the very end, when the maximum and minimum eddy currents are expected.

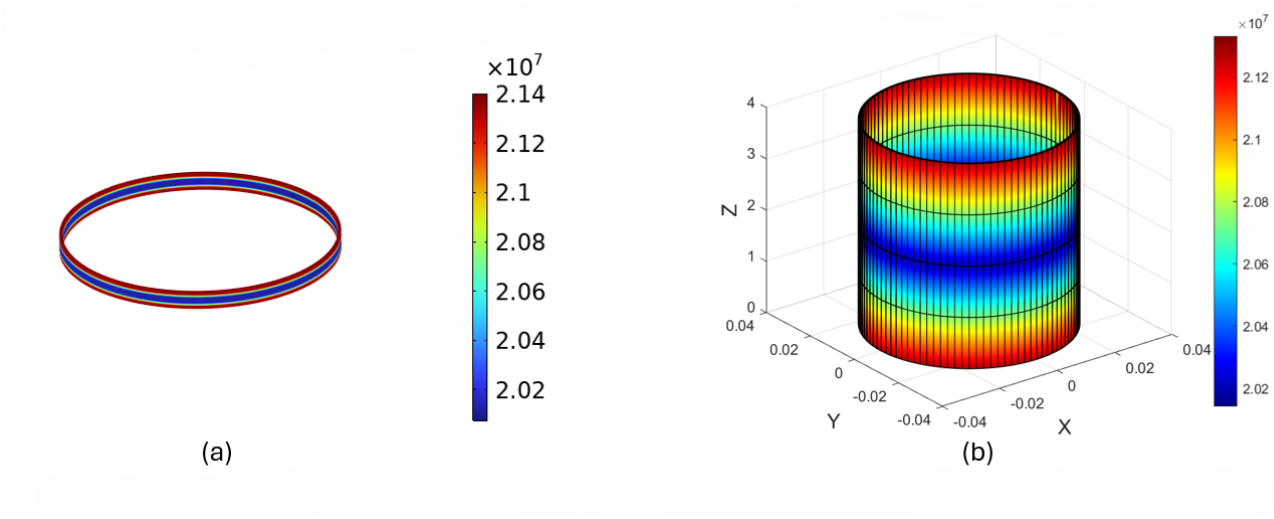


Figure 5.12: Current density distribution at t=1.025 s in COMSOL(a) and MATLAB(b).

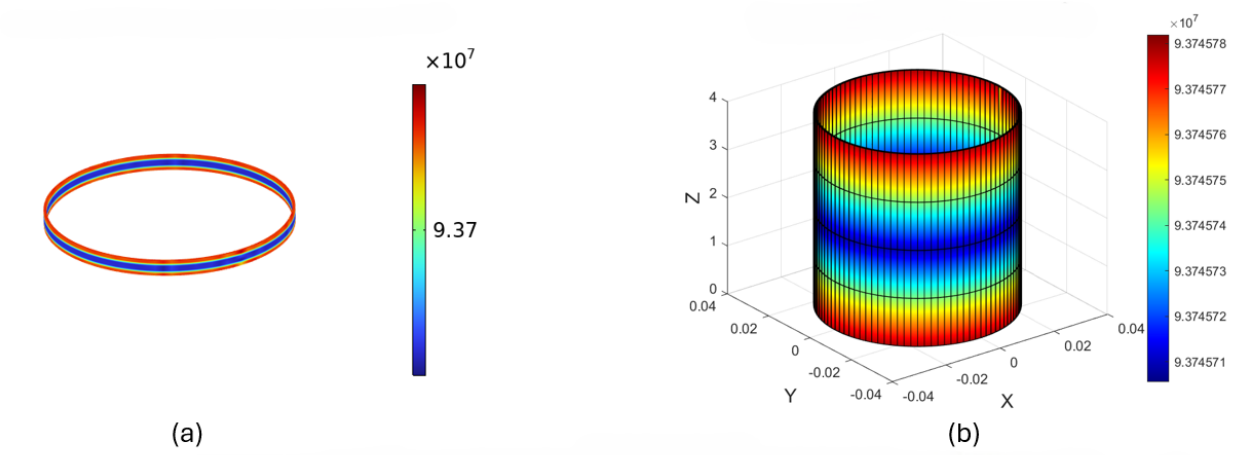
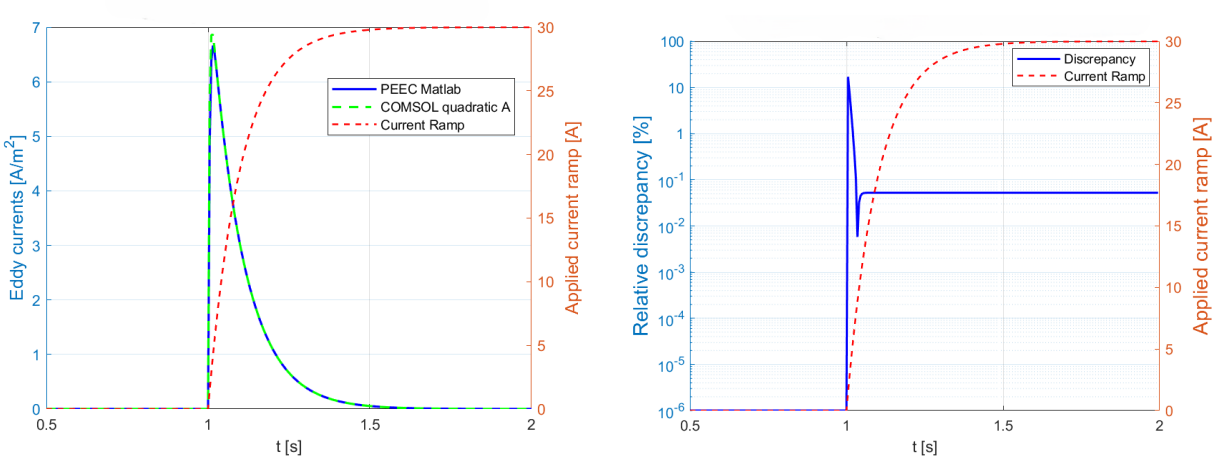


Figure 5.13: Current density distribution at t=2 s in COMSOL(a) and MATLAB(b).

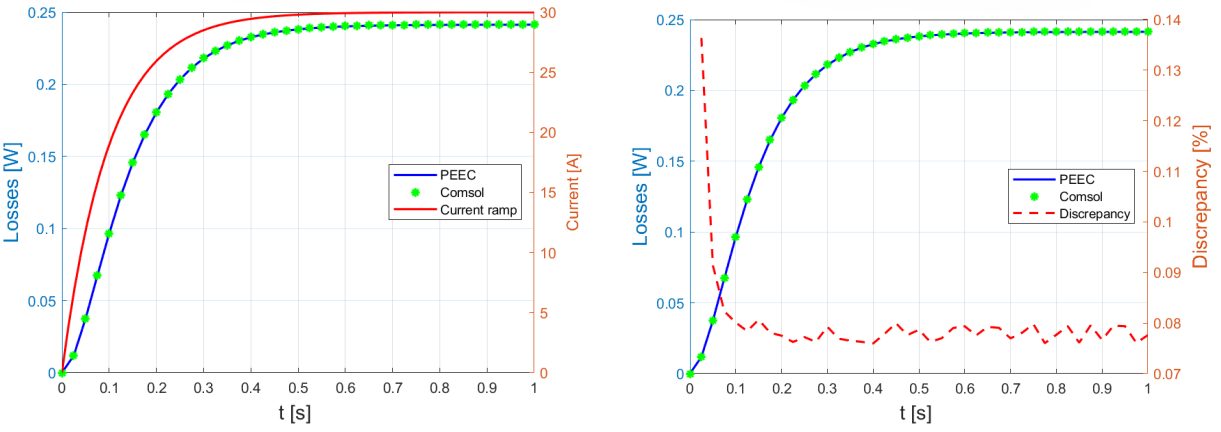
A local analysis of the evolution of eddy currents in the central turn was conducted, using BE with a constant time step $\Delta t = 0.025$s.
Before the ramp ($t < 1$), eddy currents are obviously null, as is the injected current. During the ramp ($1 < t < 2$), the current initially increases rapidly, resulting in the maximum eddy currents being obtained (see fig. 5.12); then it reaches a steady value once the ramp saturates and the current distribution becomes homogeneous, as shown in fig. 5.13.
The PEEC and T-A values were compared at a point localized at coordinate z=0 of the central turn, to reduce boundary effects. The agreement is very good in both transient and steady-state regimes. In fact, the relative discrepancy is significant only at the very start of the ramp, as COMSOL also captures a non-null current-value at t= 1s, but then drops to less than 0.1% during the ramp and the steady-state phase. Such a distance might be due to some additional factors, as briefly discussed in section 5.5, or simply to the accuracy of the derivative computation strategy to obtain the current density as $\mathbf{J} = \nabla \times \mathbf{T}$.

The Joule power losses are then considered. They were computed during the whole current ramp to observe their evolution, and, as their definition suggests, they increase following a quadratic dependence on the current density (and consequently, on the current):



(a) (b)

Figure 5.14: Eddy current density norm in one point of the central turn: (a) direct comparison, (b) relative discrepancy between the two models.



(a) (b)

Figure 5.15: Joule losses: (a) direct comparison and current ramp, (b) discrepancy between the two models.

Once again, as fig. 5.15 shows, the agreement with COMSOL is excellent, with the discrepancy being closer to 0.15% at the very beginning and dropping to 0.08% for the rest of the ramp. This relative difference is due to the different eddy current values of the two models, but it confirms the validity of the time-domain models.

In addition, with respect to the square geometry analysis, a third quantity is now of crucial interest, as it represents the final goal of the FCS project and the experimental activities. A peak magnetic flux density of 15 T is, in fact, the first target of all current

efforts, as intermediate step towards 40 T. Moreover, it is important to know its spatial distribution as the electrical conductivity of superconducting materials depends on it through the critical current density.
As a first example, the magnetic flux density was computed in the center of the 9-turn coil and its evolution was compared over time.

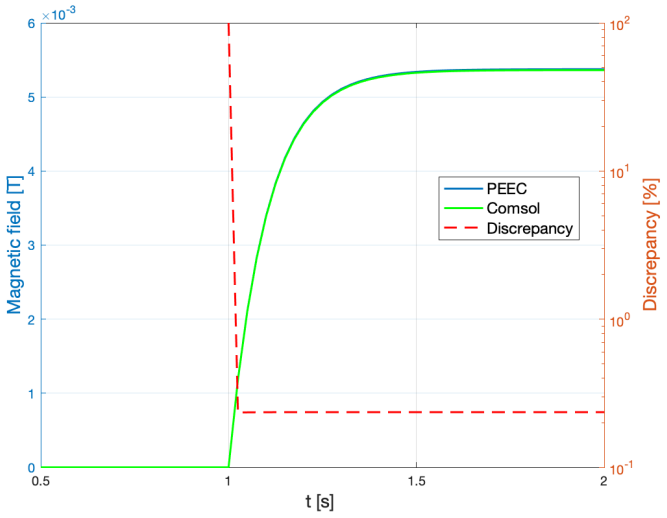
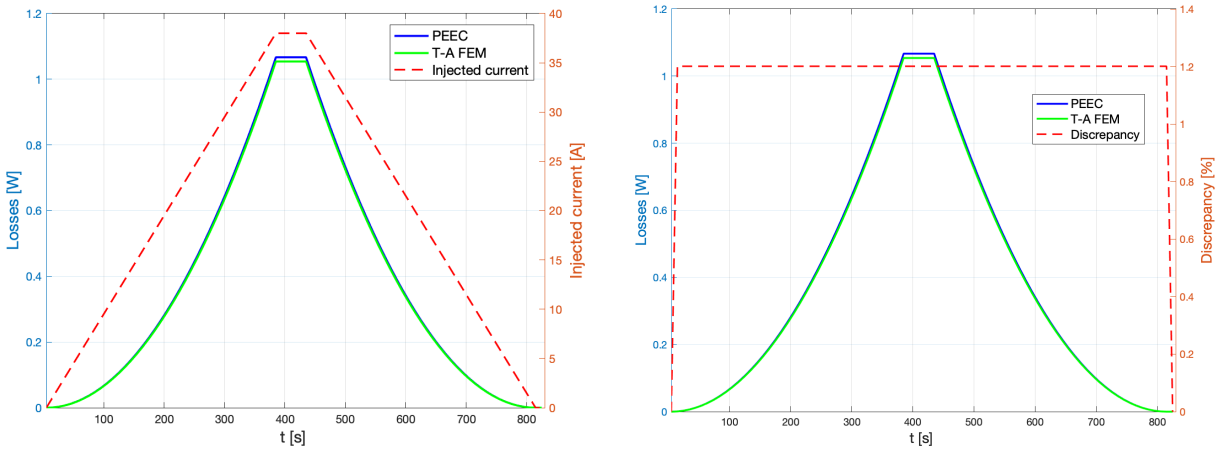


Figure 5.16: Magnetic flux density comparison in the center of a 9-turn coil.

Also in this case, the relative discrepancy is significant in percentage but not in magnitude in the very first time step, but immediately drops in the range $(0.2 - 0.5)\%$ for the rest of the ramp, confirming the correct implementation of this computation.

5.4.2. 24-turn spiral

A similar comparison was carried out for a 24 turns coil, to ensure no additional variation is introduced by scaling up the geometry. In this case, the real experimental ramp of eq. (5.11) was used, and the comparison focused on Joule losses and magnetic field. As before, the power losses follow the current profile with a quadratic behavior, as we are in the linear case, and the discrepancy can be observed to be constantly around 1.2% along the whole ramp.



(a) (b)

Figure 5.17: Joule losses in the two models with applied current(a) and discrepancy (b).

With the size of the geometry starting to be more significant, the magnetic comparison was extended, and the magnetic field was computed in three different points, instead of just one. The first one is the center (c), as for the 9 turn-coil.
The second one is at the bottom of the innermost turn (on coil in), where the winding starts. It has the goal of computing the maximum magnetic flux density being generated, in this case, around 4 times higher than the value in the center. The whole innermost region is of high interest as this peak value causes the critical current density to achieve its minimum here, representing the region that transitions first from the superconducting to the normal conducting regime and is subject to the highest mechanical stresses.
The third point is located at the bottom of the outermost turn (on coil out), where the winding ends. This point is useful to check whether the magnetic behavior of the coil is close to an ideal one. In fact, in such a point, the magnetic field lines should pass tangentially to the coil, as in fig. 5.18. If, instead, they curve inside the coil and a premature "closure" is observed, it is interpreted as a sign of non optimal behavior of the coil.

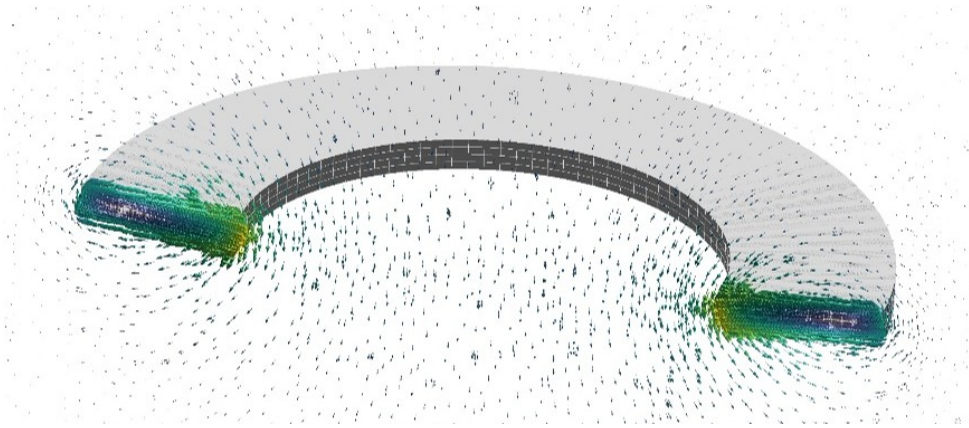
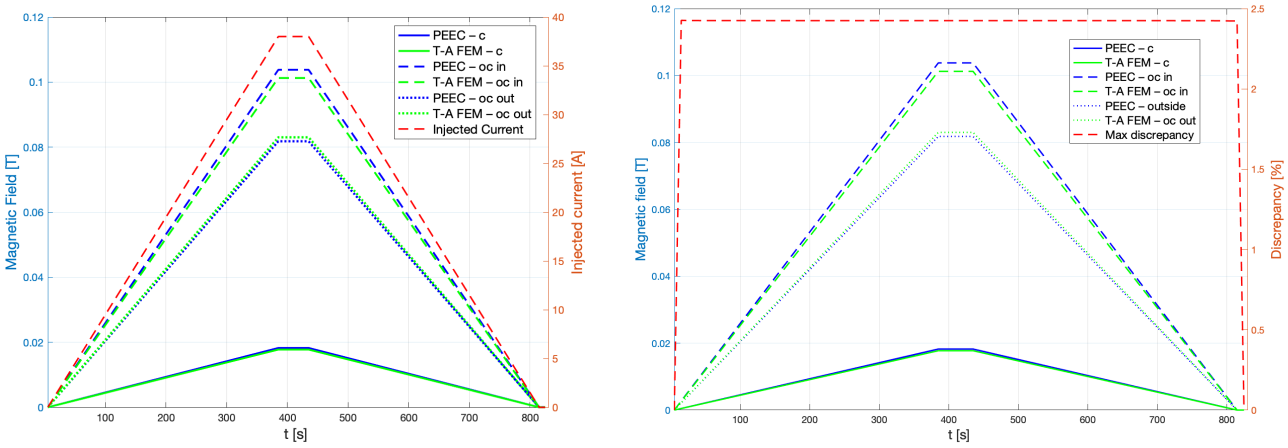


Figure 5.18: Single pancake coil simulation, magnetic flux density distribution [61].



(a) (b)

Figure 5.19: Magnetic flux density comparison with applied current(a) and maximum discrepancy (b).

In all three points, the agreement during the time evolution is very good; the maximum discrepancy between the magnetic flux densities was around 2.5% and plotted in 5.19, is observed on the inside of the coil, where the maximum value is achieved. In the other two points the difference was below 1.5%.

5.5. Remarks on the discrepancies between the two models

The small, and in some cases constant, discrepancy between the PEEC and T-A FEM results is nevertheless worth a comment. Such a distance might come from a couple of

differences that were not discussed up to here.
First of all, the normal vector along whose direction the electric vector potential **T** lies, in MATLAB, is defined with respect to the discretized geometry, while in COMSOL, with respect to the analytical description of the spiral. Hence, in every mesh element, **T** has a constant direction in the former case, while has a smoothly changing direction in the latter. In addition, the hexahedral elements used in COMSOL, being 3D, use trilinear nodal basis functions that also allow a variation of the unknown **T** along the radial direction, while this is impossible by construction in the PEEC case (being 2D). The impact of these two effects was not studied, but the first could be addressed by further reducing the thickness of each layer, while the second could be addressed by increasing the number of azimuthal mesh elements and studying whether the discrepancy between the two models is reduced.

5.6. Numerical Model - Experimental Data Comparison

The main obstacle between the current model and the complete simulation of the powering of an insulated REBCO coil is purely computational. In fact, the MATLAB model struggles as the number of degrees of freedom reaches the order of $O(10^5)$, especially with the storage of the inductance matrix, which, for a 250 turns and a double precision data type, would require around 115 GB of RAM. Therefore, this would require a necessary improvement to be made, for instance, with the use of hierarchical matrix techniques [40]. On the COMSOL side, an effort would be required to optimize the order of the basis functions used, together with the implementation of suitable stabilization techniques, in order to use linear elements for both variables **T** and **A** and significantly reduce the number of degrees of freedom employed.
Keeping this in mind, it is nevertheless possible to clearly observe a trend in the numerical results as the number of turns grows, correctly reproducing the measured center field profile, and getting progressively closer to the experimental results.

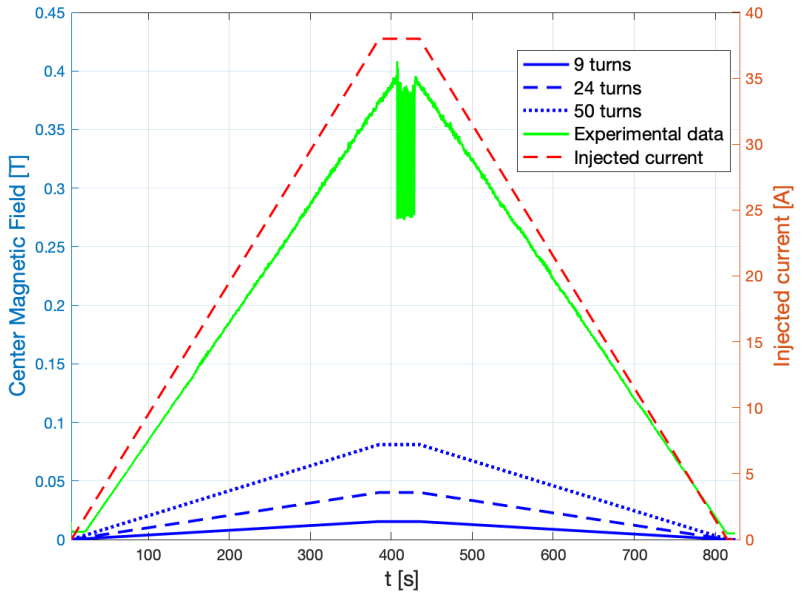


Figure 5.20: Indirect comparison between numerical (in blue) and experimental (in green) results for an insulated coil.

The comparison shown in fig. 5.20 analyzes the magnetic flux density computed in the center of the coil as the number of turns increases, from 9 to 24 to 50, and the experimental measurement of the polished (practically insulated) coil, when a current ramp from 0 to 38 A is applied.
The big oscillations in the data during the plateau represent a quench that happened in the coil, with the sudden heating causing a bigger quantity of LN_2 to boil and the coil and contacts to move, interfering with the voltage measurement in progress.

6 | Conclusions

This thesis has developed, analyzed, and validated numerical and experimental tools to support the design of ultra–high-field HTS magnets, with particular focus on the 40 T Final Cooling Solenoid for the Muon Collider. The work combined a MATLAB implementation of a PEEC integral formulation, a 3D COMSOL T–A Finite Element Method (FEM) model, and an extensive experimental campaign on REBCO non-insulated pancake coils.

From the theoretical point of view, the introduction of the current vector potential $\mathbf{T}$ automatically enabled a divergence-free representation of the current density and a natural coupling with the magnetic vector potential $\mathbf{A}$, while the thin-domain approximation reduced the problem dimension for conductors having the geometry of a tape.

In the PEEC T integral model, only the conductor domain was discretized, using first order nodal basis functions for the electric vector potential on rectangular mesh elements. The main difference with a FEM model, in the resulting algebraic system, is the dense inductance matrix, that contains self and mutual contributions. In order to deal with its weakly singular part, the Duffy quadrature rule was implemented.

The PEEC implementation was first validated on a squared domain, subject to either a uniform external magnetic field or an imposed transport current. In the frequency domain, current density distributions and Joule losses showed very good agreement with an independent Octave implementation and with a COMSOL A–V reference model, with discrepancies of only a few percent over the frequency range 1-10^3 Hz.

As an intermediate step, time-domain simulations based on an implicit Backward Euler scheme and a harmonic forcing term were compared with the steady-state frequency-domain response, both in amplitude and phase, confirming the correctness of the temporal discretization.

The same methodology of the square domain was then applied to a spiral geometry. For both a 9-turn and a 24-turn spiral domains, excited by an exponential and linear current ramps, respectively, the PEEC and COMSOL models showed excellent agreement in the time evolution of local eddy currents, global Joule losses, and magnetic flux density at the center, on the inside, and on the outside of the coil. Relative discrepancies remained

at the level of a few percent during the ramp and in steady state, indicating that the thin-domain PEEC approximation still captures the electrodynamic behavior of the coil very well, with a significantly reduced number of unknowns.

In parallel with the numerical work, more than twenty fully soldered non-insulated RE-BCO pancake coils were fabricated and characterized at 77 K, immersed in a boiling liquid nitrogen bath. The winding setup, based on wet winding through a molten Sn–Pb solder bath, was progressively optimized to achieve uniform 3–4 μm solder layers, good mechanical integrity, and good reproducibility of the process.
Cryogenic tests with current ramps and steps yielded a systematic characterization of the electrical behavior of each coil, and the quantification of the electrical elements constituting its equivalent circuit. Non-insulated coils exhibited characteristic time constants in the range of 220–350 s, consistent with an effective turn-to-turn surface resistivity of order 10^{-6} $\mu\Omega \cdot \mathrm{m}^2$, an inductance of 8 mH, and showed stable operation above the critical current thanks to the radial current redistribution.
Finally, the COMSOL 3D T–A model was used to reproduce the data an insulated version of the tested superconducting pancake coils. The model was validated against the measurement of the center magnetic flux density, and the current results showed a very promising consistency with the experimental data, the reproduction of which is currently limited only by computational obstacles.

6.1. Future developments

The prosecution of this project is quite straightforward.
The very first step would be to benchmark the power law implementation between the two models. After carefully implementing a current density and magnetic field dependent resistivity in the PEEC model (where only the dependence on $\mathbf{B}$ is currently missing), the main critical step would be to implement or select a robust non-linear solver capable of handling the high non-linearities arising when the current density approaches or exceeds the critical one J_c.
The second step would then be to extend the model to include the possibility for the current to flow radially, realizing a complete simulation tool for NI HTS pancake coils and their cryogenic behavior. The approach to be followed for the FEM COMSOL model could be similar to the one of [29] and [16], i.e. properly modulating the Dirichlet boundary condition on $\mathbf{T}$ to include the transverse flow of the current. On the other hand, thanks to the possibility of a circuital reinterpretation of the PEEC model, it would be possible to

imagine that additional circuital branches could be added in the radial direction between one turn and another. By writing the Kirchhoff equations, having the total current flowing in each of them as unknown, the algebraic problem could be extended to include the computation of the radial currents.

Bibliography

[1] Guilherme Henriques Farromba Teixeira Alves. Recycling of ybco high-temperature superconductors bulks. June 2023.

[2] Paolo Andreetto, Nazar Bartosik, Laura Buonincontri, Daniele Calzolari, Vieri Candelise, Massimo Casarsa, Luca Castelli, Mauro Chiesa, Anna Colaleo, Giacomo Da Molin, Matthew Forslund, Luca Giambastiani, Alessio Gianelle, Karol Krizka, Sergo Jindariani, Anton Lechner, Donatella Lucchesi, Leo Mareso, Paola Mastrapasqua, Patrick Meade, Alessandro Montella, Simone Pagan Griso, Nadia Pastrone, Lorenzo Sestini, Rosamaria Venditti, Angela Zaza, and Davide Zuliani. Higgs physics at a $\sqrt{s} = 3$ tev muon collider with detailed detector simulation, 2024.

[3] Ivo Babuška. The finite element method with lagrangian multipliers. *Numerische Mathematik*, 20(3):179–192, June 1973.

[4] C. P. Bean. Magnetization of hard superconductors. *Physical Review Letters*, 8(6):250–253, March 1962.

[5] CHARLES P. BEAN. Magnetization of high-field superconductors. *Reviews of Modern Physics*, 36(1):31–39, January 1964.

[6] M. Bogomilov, R. Tsenov, and Vankova-Kirilova et al. Transverse emittance reduction in muon beams by ionization cooling. *Nature Physics*, 20(10):1558â€“1563, July 2024.

[7] B. Bordini, C. Accettura, A. Bertarelli, L. Bottura, A. Dudarev, A. Kolehmainen, T. Mulder, A. Verweij, and M. Wozniak. Conceptual design of a rebco non/metal-insulated ultra-high field solenoid for the muon collider. *IEEE Transactions on Applied Superconductivity*, 34(3):1–10, May 2024.

[8] Bernardo Bordini, Luca Bottura, Arnaud Devred, Lucio Fiscarelli, Mikko Karppinen, Gijs de Rijk, Lucio Rossi, Frédéric Savary, and Gerard Willering. *Nb3Sn 11 T Dipole for the High Luminosity LHC (CERN)*, pages 223–258. Springer International Publishing, 2019.

[9] Lorenzo Bortot. Simulation of transient effects in high-temperature superconducting magnets. 2022.

[10] L Bottura. Magnet quench 101, 2014.

[11] T. Boutboul, L. Oberli, A. den Ouden, D. Pedrini, B. Seeber, and G. Volpini. Heat treatment optimization studies on pit nb_3sn strand for the ned project. *IEEE Transactions on Applied Superconductivity*, 19(3):2564–2567, June 2009.

[12] Franco Brezzi and Michel Fortin. *Mixed and Hybrid Finite Element Methods*, volume 15 of *Springer Series in Computational Mathematics*. Springer-Verlag, 1991.

[13] Oliver Brüning and Markus Zerlauth. Lhc operation and the high-luminosity lhc upgrade project, 2025.

[14] CERN. The standard model.

[15] Jay Chan. Investigation of higgs boson decaying to di-muon, dark matter produced in association with a higgs boson decaying to b-quarks and unbinned profiled unfolding, 2023.

[16] Yong Chen, Qiuliang Wang, Benzhe Zhou, Shixian Liu, Fangliang Dong, Kangshuai Wang, Hongzhuo Zeng, Xiaoyu Ji, Lei Wang, and Jianhua Liu. Electromagnetic modeling of no-insulation rebco coils based on t – a formulation: from 2d to 3d. *Superconductor Science and Technology*, 39(2):025005, February 2026.

[17] COMSOL. Manually setting the scaling of variables.

[18] COMSOL. Understanding the fully coupled vs. segregated approach and direct vs. iterative linear solvers.

[19] COMSOL. Understanding the fully coupled vs. segregated approach and direct vs. iterative linear solvers.

[20] P.C. de Vries and Y. Gribov. Iter breakdown and plasma initiation revisited. *Nuclear Fusion*, 59(9):096043, August 2019.

[21] D. Dew-Hughes. Flux pinning mechanisms in type ii superconductors. *The Philosophical Magazine: A Journal of Theoretical Experimental and Applied Physics*, 30(2):293–305, August 1974.

[22] Julien Dular. *Standard and Mixed Finite Element Formulations for Systems with Type-II Superconductors*. PhD thesis, ULiège - Université de Liège [Sciences Appliquées], Liège, Belgium, 17 March 2023.

[23] Julien Dular, Christophe Geuzaine, and Benoit Vanderheyden. Finite-element formulations for systems with high-temperature superconductors. *IEEE Transactions on Applied Superconductivity*, 30(3):1–13, April 2020.

[24] Julien Dular, Alexander Glock, Arjan Verweij, and Mariusz Wozniak. Distributed inter-strand coupling current model for finite element simulations of rutherford cables, 2025.

[25] Wolfgang Engelhardt. Gauge invariance in classical electrodynamics, 2005.

[26] Fujikura. Y-based high temperature superconductor. company leaflet at icec (2014).

[27] Shinji Fujita, Shogo Muto, Wataru Hirata, Tomo Yoshida, Kazuomi Kakimoto, Yasuhiro Iijima, Masanori Daibo, Takanobu Kiss, Tatsunori Okada, and Satoshi Awaji. Flux-pinning properties of bahfo3-doped eubco-coated conductors fabricated by hot-wall pld. *IEEE Transactions on Applied Superconductivity*, 29(5):1–5, August 2019.

[28] Bill Gear. Backward differentiation formulas. *Scholarpedia*, 2(8):3162, 2007.

[29] Hengrui Geng, Sijian Wang, Shouhong Shan, Huadong Yong, and Youhe Zhou. Fast electromagnetic modeling of high-temperature superconductors: a reduced-order scheme for the t–a formulation. *Superconductor Science and Technology*, 39(2):025002, February 2026.

[30] Luca Giussani, Luca Di Rienzo, Massimo Bechis, and Carlo de Falco. Computation of armor losses in ac submarine cables. *IEEE Transactions on Power Delivery*, 36(5):3014–3021, October 2021.

[31] Alexander Glock. Homogenization methods for transient simulations of superconductors. 2025.

[32] Zachary S. Hartwig and Vieira et al. The sparc toroidal field model coil program. *IEEE Transactions on Applied Superconductivity*, 34(2):1–16, March 2024.

[33] Chinese high field magnet laboratory. Chinese high field magnet laboratory, 2011.

[34] National high field magnet laboratory. National high field magnet laboratory, 2011.

[35] Stephen Holmes, Ronald S Moore, and Vladimir Shiltsev. Overview of the tevatron collider complex: goals, operations and performance. *Journal of Instrumentation*, 6(08):T08001–T08001, August 2011.

[36] B.J. Holzer. Introduction to particle accelerators and their limitations. *CERN Yellow Reports*, pages Vol 1 (2016): Proceedings of the 2014 CAS–CERN Accelerator School: Plasma Wake Acceleration, 2016.

[37] Felix Huber, Wenjuan Song, Min Zhang, and Francesco Grilli. The t-a formulation: an efficient approach to model the macroscopic electromagnetic behaviour of hts coated conductor applications. *Superconductor Science and Technology*, 35(4):043003, March 2022.

[38] Rasmus Ischebeck. I.10 — synchrotron radiation. *CERN Yellow Reports: School Proceedings*, 3:433, 2024.

[39] Christian Lacroix, Jaël Giguère, Simon-Mathieu Bergeron Hartman, Haïfa Ben Saad, Anthony Martin, Thomas Leduc, Maxime Gendron-Paul, Zakaria Bellil, Jean-Hughes Fournier-Lupien, Lucile Moret, Pedro Barusco, Xavier Granados, Xavier Obradors, Marcela Pekarčiková, Fedor Gömöry, Veit Grosse, Markus Bauer, and Frédéric Sirois. Normal zone propagation in various rebco tape architectures. *Superconductor Science and Technology*, 35(5):055009, March 2022.

[40] Francesco Lucchini and Riccardo Torchio. Comparative analysis of hierarchical matrix formats for electromagnetic device modeling: A preliminary study. In *2025 International Symposium on Electromagnetic Compatibility – EMC Europe*, pages 1294–1297. IEEE, September 2025.

[41] Enze Ma, Yulong Li, and Yuan Gao. Performance analysis of superconducting motors for electrical aircraft propulsion using electromagnetic–thermal coupling method. *Journal of Applied Physics*, 137(3), January 2025.

[42] Ryosuke Miyao, Hajime Igarashi, Atsushi Ishiyama, and So Noguchi. Thermal and electromagnetic simulation of multistacked no-insulation rebco pancake coils on normal-state transition by peec method. *IEEE Transactions on Applied Superconductivity*, 28(3):1–5, April 2018.

[43] Hiroshi Miyazaki, Sadanori Iwai, Tatsuro Uto, Yasumi Otani, Masahiko Takahashi, Taizo Tosaka, Kenji Tasaki, Shunji Nomura, Tsutomu Kurusu, Hiroshi Ueda, So Noguchi, Atsushi Ishiyama, Shin-ichi Urayama, and Hidenao Fukuyama. Progress in the development of conduction-cooled rebco magnets for ultrahigh-field mri systems. *IEEE Transactions on Applied Superconductivity*, 27(4):1–5, June 2017.

[44] S. E. Mousavi and N. Sukumar. Generalized duffy transformation for integrating vertex singularities. *Computational Mechanics*, 45(2–3):127–140, October 2009.

[45] Tim Mulder, Alexey Dudarev, Matthias Mentink, Danko van der Laan, Marc Dhalle, and Herman ten Kate. Performance test of an 8 ka @ 10-t 4.2-k rebco-corc cable. *IEEE Transactions on Applied Superconductivity*, 26(4):1–5, June 2016.

[46] COMSOL Multyphisics. The magnetic and electric fields interface.

[47] Solovyov Mykola and Gömöry Fedor. A–v formulation for numerical modelling of superconductor magnetization in true 3d geometry. *Superconductor Science and Technology*, 32(11):115001, September 2019.

[48] Meenakshi Narain, Laura Reina, and Alessandro Tricoli. The future of us particle physics – the snowmass 2021 energy frontier report, 2022.

[49] Mahesh Paidpilli, Chirag Goel, Bhabesh Sarangi, Siwei Chen, Eduard Galstyan, Jan Jaroszynski, Griffin Bradford, Dmytro Abraimov, and Venkat Selvamanickam. 40-meter-long rebco tapes with critical current over 4,000 a/12 mm at 4.2 k and 13 t by advanced mocvd. *Superconductivity*, 9:100081, March 2024.

[50] Michael Parizh. Viewpoint on the manuscript by zachary s hartwig et al 'viper: an industrially scalable high-current high-temperature superconductor cable' 2020 supercond. sci. technol. 33 11lt01. *Superconductor Science and Technology*, 35(1):010501, December 2021.

[51] Jakob Rhyner. Magnetic properties and ac-losses of superconductors with power law current—voltage characteristics. *Physica C: Superconductivity*, 212(3):292–300, 1993.

[52] L. Rossi and E. Todesco. Conceptual design of 20 t dipoles for high-energy lhc, 2011.

[53] A.E. Ruehli. Equivalent circuit models for three-dimensional multiconductor systems. *IEEE Transactions on Microwave Theory and Techniques*, 22(3):216–221, March 1974.

[54] Meenaloshini Satgunam. An engineering perspective on the progress and implementation of superconducting materials: Insights from low- and high-temperature superconductors and application. *Jurnal Kejuruteraan*, 37(7):3445–3469, October 2025.

[55] Evan Sheehan, John Pfotenhauer, Franklin Miller, and Owen Christianson. Quench detection and protection of an hts coil. *IOP Conference Series: Materials Science and Engineering*, 278:012182, December 2017.

[56] Jonathan Siau. *Unstructured PEEC formulationsconsidering resistive, inductiveand capacitive effects forpower electronics*. Theses, Université Grenoble Alpes, December 2016.

[57] C. P. Steinmetz. *Complex quantities and their use in electrical engineering*. Chicago, IL, USA, 1893.

[58] Bharath Kumar T, Krupanidhi Y G, and Ramya Y A. Superconductivity: Basic principles and type i vs type ii superconductors. *World Journal of Advanced Research and Reviews*, 13(1):895–900, January 2022.

[59] Herman ten Kate, Anna Kario, and Simon Otten. Rebco superconductor mechanical properties. https://indico.cern.ch/event/1220254/contributions/5270725/, 2023.

[60] Taizo Tosaka, Hiroshi Miyazaki, Sadanori Iwai, Yasumi Otani, Masahiko Takahashi, Kenji Tasaki, Shunji Nomura, Tsutomu Kurusu, Hiroshi Ueda, So Noguchi, Atsushi Ishiyama, Shinichi Urayama, and Hidenao Fukuyama. R&d project on hts magnets for ultrahigh-field mri systems. *IEEE Transactions on Applied Superconductivity*, 26(4):1–5, June 2016.

[61] Andrea Vitrano, Mariusz Wozniak, Erik Schnaubelt, Tim Mulder, Emmanuele Ravaioli, and Arjan Verweij. An open-source finite element quench simulation tool for superconducting magnets. *IEEE Transactions on Applied Superconductivity*, 33(5):1–6, August 2023.

[62] Kai Wang, Hao Dong, Daxing Huang, Hongjing Shang, Bowei Xie, Qi Zou, Lin Zhang, Changping Feng, Hongwei Gu, and Fazhu Ding. Advances in second-generation high-temperature superconducting tapes and their applications in high-field magnets. *Soft Science*, 2(3):12, 2022.

[63] Frederick S. Wells, Alexey V. Pan, X. Renshaw Wang, Sergey A. Fedoseev, and Hans Hilgenkamp. Analysis of low-field isotropic vortex glass containing vortex groups in yba2cu3o7x thin films visualized by scanning squid microscopy. *Scientific Reports*, 5(1):8677, 2015.

[64] Wikipedia. Galerkin method.

[65] Victor M. R. Zermeño, Frederic Sirois, Makoto Takayasu, Michal Vojenčiak, Anna Kario, and Francesco Grilli. A self-consistent model for estimating the critical current of superconducting devices. *Superconductor Science and Technology*, 28(8):085004, June 2014.

[66] Huiming Zhang, Min Zhang, and Weijia Yuan. An efficient 3d finite element method model based on the t–a formulation for superconducting coated conductors. *Superconductor Science and Technology*, 30(2):024005, December 2016.

[67] Yue Zhao, Yue Wu, Amit Goyal, Hannu Huhtinen, Petriina Paturi, and Yuji Tsuchiya. Commercial compact fusion triggered rebco tape industry: Pulsed laser deposition

technology opportunities and challenges. *Superconductivity*, 15:100188, September 2025.

List of Figures

1.1 Overview of the size and particle collision points of the LHC [15]. 2
1.2 Layout of the Muon Collider as presented by the US MAP ([41]), with the 5 main stages highlighted. 3
1.3 Layout and magnetic field distribution for the 40 T solenoid. Left: magnetic field distribution. Right: a quarter cross-section enabling the view of the full structure. 4
1.4 Left: plot of electrical resistivity illustrating the its temperature dependence. Right: [1] schematic of the Meissner effect showing the expulsion of magnetic field lines. 5
1.5 Left: [1] schematic of the Meissner effect for type II superconductors; Right: [63] plot of quantum vortices of magnetic field for $\mathbf{B}_{C1} < \mathbf{B} < \mathbf{B}_{C2}$. 6
1.6 Left: [11] cross section of a Nb_3Sn wire; Right: [62] Critical current density versus magnetic field and temperature for YBCO, Bi-2223, NbTi, and MgB_2. 7
1.7 Layers composing a REBCO tape [59]. 7
1.8 Left: R&D outline for the development of fusion devices [50] at CFS; Right: Cryogenic system of UHF-MRI HTS magnet for brain imaging and whole-body imaging [60]. 8

2.1 Visualisation of the different computational domains of the two equations [66] 18
2.2 Example of domain satisfying the mentioned condition 19
2.3 Generic cross section of the tape Σ on which T2 and T1 are fixed. 20
2.4 Partial element equivalent circuit of a double pancake [42]. 24
2.5 Sharpness of the transition depending on n when $\mathbf{J}/J_c \leq 1$. 28
2.6 J_c surfaces at different temperatures, as function of magnetic field and angle [26]. 30

3.1 Spiral geometry visualized in COMSOL with the local reference system $\{\hat{\mathbf{r}}, \hat{\theta}, \hat{\mathbf{z}}\}$ 32
3.2 Mesh discretization of coil and air domain in COMSOL 33

3.3 Duffy nodes for a singularity in the origin (a); Quadrature error (b) 38
3.4 Example of gridNodes with 10 nodes in both directions 41
3.5 Sparsity pattern of the resistance (a) and inductance (b) matrices 42
3.6 L^{self} entries behavior with respect to the mesh element's size 43
3.7 Convergence of the self inductance with respect to the number of Duffy nodes, in absolute terms (a) and its increment (b) 44
3.8 Assembly time of the mutual inductance matrix 45
3.9 Second order Lagrangian basis function on [0,1] 49
3.10 Imposition of the external current density as forcing term to solve the magnetic equation 50
3.11 Imposition of the Dirichlet condition on T on the upper boundary 51

4.1 Visualization of the coil characteristic dimensions. 55
4.2 Winding setup simplified sketch. 55
4.3 Complete setup with multimeters, LN_2 dewar and cryostat (a) and the instrumented coil submerged in LN_2 (b). 57
4.4 Real instrumented coil. 58
4.5 Simplified equivalent circuit of an NI superconducting coil. 59
4.6 Measurement of voltage over half of a stepping (a) and ramping (b) experiments in the six different sectors of the coil. 61
4.7 Behavior of the voltage across the coil during a current ramp exceeding I_c . 61
4.8 V-I curves of three different coils that were measured 62
4.9 B-I curves of eight different coils 62
4.10 Left: Schematic representation of half of the cross section before (a) and after (b) polishing. 63

5.1 Meshed square geometry in COMSOL. 67
5.2 Mesh of a 9-turn spiral and the surrounding air in COMSOL. 68
5.3 Real (a) and imaginary (b) part of the current density distribution. 69
5.4 Comparison of Joule losses and discrepancy between the two models(a) and computation time (b). 70
5.5 Comparison of the real part of the current density distribution at f=5 kHz. 71
5.6 Joule losses comparison from 1 to 10^4 Hz (a) and showcase of skin effect along δ at f=10^4Hz. 71
5.7 Computation time PEEC vs Comsol with respect to the number of mesh elements in the conductor for f = f_0. 72
5.8 Showcase degree of freedom for comparison (a) and examples of periodic current ramps (b). 73

5.9 Time evolution of electric vector potential (a) and eddy currents (b). . . . 74
5.10 Fourier transform comparison of the electric vector potential in amplitude (a) and phase (b) for f = 10 Hz. 74
5.11 Injected current density, forcing terms described in eq. (5.10) (a) and eq. (5.11) (b). 76
5.12 Current density distribution at t=1.025 s in COMSOL(a) and MATLAB(b). 76
5.13 Current density distribution at t=2 s in COMSOL(a) and MATLAB(b). . 77
5.14 Eddy current density norm in one point of the central turn: (a) direct comparison, (b) relative discrepancy between the two models. 78
5.15 Joule losses: (a) direct comparison and current ramp, (b) discrepancy between the two models. 78
5.16 Magnetic flux density comparison in the center of a 9-turn coil. 79
5.17 Joule losses in the two models with applied current(a) and discrepancy (b). 80
5.18 Single pancake coil simulation, magnetic flux density distribution [61]. . . . 81
5.19 Magnetic flux density comparison with applied current(a) and maximum discrepancy (b). 81
5.20 Indirect comparison between numerical (in blue) and experimental (in green) results for an insulated coil. 83

List of Tables

4.1 Examples of REBCO tapes used for coil fabrication. 54
4.2 Main winding parameters for 4 fabricated example coils. 56

5.1 Simulation parameters for square geometry, see fig. 5.1. 66
5.2 Set of parameters for the spiral geometry. 67
5.3 Mesh refinement study PEEC MATLAB vs reference PEEC Octave. 69